

# Large-Eddy Simulations of Marine Cumulus and Stratocumulus and Study of Humidity Halos and Aerosol Indirect Radiative Effects

Thesis by

Miao-Ling Lu

In Partial Fulfillment of the Requirements

for the Degree of

Doctor of Philosophy



California Institute of Technology

Pasadena, California

2005

(Defended October 19, 2004)

© 2005

Miao-Ling Lu

All Rights Reserved

To my family

# Acknowledgments

First, I would like to express my gratitude toward my advisor, John Seinfeld, for offering me the opportunity to study in Caltech. During these years, John was always there to provide me guidance and valuable suggestions whenever I needed his help. He broadens my scientific perspective and also inspires me from his assiduous dedication in science. I appreciate for what I have learned from him. In addition, I wish to thank Richard Flagan for sharing the experience of aircraft mission data and his scientific enthusiasm when working on the HALO project .

I wish to thank Bob McClatchey for his suggestive comments and advices during our collaboration in the HALO project. Hafliði Jonsson in CIRPAS is thankful for very fast response for my data processing questions. I also thank other collaborators, Andy Freedman and Jian Wang, for their support in this project.

I appreciate Graham Feingold in NOAA ETL for his expertise in the bin-microphysics. I am benefited from his reviews and insightful comments in my aerosol indirect effect paper.

I would also like to thank the colleagues in Seinfeld and Rick's group. My longtime classmate and groupmate, Serena Chung, is thankful for her friendship and many interesting discussions during these years. Bill Conant is thankful for being a nice officemate and sharing many inspiring scientific discussions during our collaboration in CRYSTAL-FACE and CSTRIFE. I would also thank Roya Bahreini for her friendship and sending me a lot

of activity news. Thank Tracey Rissman and Tim VanReken for offering me several rides. Thank Tomtor Varutbangkul for organizing numerous musical tours so that I am fortunate to enjoy these great performances. Past members in the modeling group, Peter Adams and Thanos Nenes are thankful for their help when I just came to the group's computer lab. I appreciate all the past and present group members for creating a great research environment here. I would like to thank secretaries, Ann Hilgenfeldt and Linda Scott for their professional assistances.

Chris Golaz, Craig Tremback, Sue van den Heever, and Bob Walko are appreciated for their help in my RAMS model modifications.

Finally, I would especially express my gratitude to my family - Kai-En, Vivian, Fong, and my parents for their continuous love and unconditional supports. I am much indebted to my husband, Kai-En, for his companionship and encouragement throughout my PhD life.

# Abstract

This thesis is motivated by using a state-of-the-art 3D (three-dimensional) LES (Large-Eddy Simulation) numerical model to simulate cumulus and stratocumulus clouds and to understand how these warm clouds perturb the Earth’s radiation budget. The first part of the thesis focuses on understanding the characteristics of the cloud humidity halos, the significant enhancements in humidity around cumulus clouds, and their radiative impacts. The simulated cloud and halo properties were compared with the measurement data from the aircraft campaign — “Cloud Halo” conducted in Hawaii, 2001. The cloud halo spatial distribution, the relationship with the vertical wind shear, and the temporal variation with cloud lifetime are explored by the 3D numerical simulations. Results suggest that halos are formed as a result of evaporation of cloudy air or detrainment of high humidity by the turbulent mixing in the cloud lateral boundary regions, or simply due to cloud dissipation. Humidity halos absorb the incoming sunlight, warm the atmosphere, and cool the surface. The 3D radiative transfer model results show that the SW column absorption (surface – 3.4 km) enhanced by the halo is  $1.32 \text{ W m}^{-2}$  averaged over the cloud mature and dissipating stages, a 1.3% change in the absence of the halo, for the cloud of the Cloud Halo experiment. Halo is the possible loci for new particle formation, and several incidences have been seen in the Cloud Halo experiment.

The second part of the thesis is to understand the first and second aerosol indirect

effects by conducting 98 3D LES simulations of the marine stratocumulus clouds — under various conditions of nighttime and daytime, SST (sea surface temperature), aerosol number concentration, and large-scale subsidence rate. Based on the statistical analysis, the cloud optical depth is found to be positively correlated with the cloud LWP (liquid water path), which is mainly regulated by large-scale subsidence and SST. The regression analysis shows that the second aerosol indirect effect is more pronounced in clean than polluted clouds and that it increases (reduces) the cloud optical depth for the same relative change in aerosol number concentration than considering the Twomey (first indirect) effect alone. Introducing a small amount of giant sea salt aerosols into the simulation lowers the number of cloud droplets activated and initiates precipitation for non-drizzling clouds. It also results in a reduction of cloud optical depth by 3% – 77% (for aerosol number concentration  $\geq 1000$   $\text{cm}^{-3}$ ) for heavily drizzling cases. Simulation results suggest that concurrent observation of cloud LWP and aerosol number concentration is needed for assessing the aerosol indirect effect.

# Contents

<b>Acknowledgments</b>	<b>iv</b>
<b>Abstract</b>	<b>vi</b>
<b>1 Preface</b>	<b>1</b>
1.1 Introduction . . . . .	1
1.2 Organization of the thesis . . . . .	3
<b>2 Cloud halos: numerical simulation of dynamical structure and radiative impact</b>	<b>4</b>
2.1 Abstract . . . . .	4
2.2 Introduction . . . . .	5
2.3 Dynamic cloud model . . . . .	8
2.4 Simulations of the cloud and associated halo . . . . .	12
2.5 Radiative effects of cloud halos . . . . .	20
2.6 Summary . . . . .	26
2.7 Acknowledgment . . . . .	28
<b>3 Analysis of humidity halos around trade wind cumulus clouds</b>	<b>46</b>
3.1 Abstract . . . . .	46

3.2	Introduction . . . . .	47
3.3	Cloud Halo field experiment and instrumentation . . . . .	49
3.4	Halo observations . . . . .	54
3.5	Numerical simulation . . . . .	60
3.6	Simulated radiative effect of cloud and halo . . . . .	64
3.7	Conclusions . . . . .	68
3.8	Acknowledgments . . . . .	70
<b>4</b>	<b>Study of the aerosol indirect effect by large-eddy simulation of marine stratocumulus</b>	<b>90</b>
4.1	Abstract . . . . .	90
4.2	Introduction . . . . .	91
4.3	Model setup . . . . .	94
4.4	LES simulation . . . . .	98
4.5	Results . . . . .	102
4.6	Effect of giant sea salt on stratocumulus dynamics . . . . .	108
4.7	Daytime conditions . . . . .	116
4.8	Implications for the aerosol indirect effect . . . . .	117
4.9	Acknowledgments . . . . .	120
<b>5</b>	<b>Future studies</b>	<b>142</b>

# List of Figures

- 2.1 Schematic of cloud halo (shaded region). This depiction shows a westerly wind increasing with height. Upshear and downshear are defined relative to the vertical wind shear. In the upper right corner, average absolute humidity is sketched as a function of the distance from the cloud edge.  $\bar{\rho}_{vc}(z)$  is the mean absolute humidity of the cloud. When the absolute humidity approaches a constant value, it is defined as  $\bar{\rho}_{ve}(z)$ .  $\bar{\rho}_{ve}(z)$  is the  $e$ -folding absolute humidity calculated by Eq. (2.3). If there is cloud at an arbitrary height  $z$ , the cloud halo is defined by that region of the humidity field where  $\bar{\rho}_{vc}(z) > \rho(z) > \bar{\rho}_{ve}(z)$ . If there is no cloud at that altitude, the halo is defined by Eq. (2.4). . . . . 31
- 2.2 Schematic of radiative transfer in the cloud halo for a cumulus cloud. The cloud halo absorbs incident solar radiation directly, as well as the scattered radiation from nearby cloud droplets. . . . . 32

- 2.3 Skew T-log  $p$  diagram of environmental conditions for a typical shallow cumulus off the northern California coastline. Temperature and dew point temperature profiles are represented by thick lines. The skewed abscissa is temperature ( $^{\circ}\text{C}$ ) and the ordinate is pressure (hPa). Dotted lines labeled in Kelvins represent dry adiabats while curved, dashed lines labeled in  $^{\circ}\text{C}$  are pseudoadiabats. Straight-dashed lines labeled in  $\text{g kg}^{-1}$  are isopleths of the saturation water vapor mixing ratio. This vertical sounding profile was obtained in Oakland, CA ( $37^{\circ}44'\text{N}$ ,  $122^{\circ}13'\text{W}$ ) at 1200 GMT, 26 October 2000. The north-south wind is arbitrarily set to zero. The sounding profile features an increasing easterly wind with height below 925 hPa. . . . . 33
- 2.4 Simulated development of shallow cumulus off the northern California coast near Oakland in the absence of wind, for several selected time stages. The contour represents a cloud liquid water content (LWC) of  $0.01 \text{ g m}^{-3}$ , chosen to define the cloud boundary. The shaded region outside the cloud boundary, defined to be the cloud halo, is where the absolute humidity exceeds the  $e$ -folding water vapor density (see Fig. 2.1). . . . . 34
- 2.5 Same as Fig. 2.4 but in the presence of the wind shear shown in Fig. 2.3. . . . . 35
- 2.6 Skew T-log  $p$  diagram of environmental conditions for a typical cumulus near Hawaii. The description of the lines and ordinates is as in Fig. 2.3. This vertical sounding profile was observed at Lihue on Kauai, Hawaii ( $21^{\circ}59'\text{N}$ ,  $159^{\circ}21'\text{W}$ ) at 0000 GMT, 8 August 2000. The north-south wind is arbitrarily set to zero. The sounding profile features a decreasing easterly wind with height up to 700 hPa, overlain by an increasing westerly wind with height in the cloud layer. . . . . 36

2.7 Same as Fig. 2.4, but for cumulus cloud near Hawaii in the absence of wind. 37

2.8 Same as Fig. 2.7 but in the presence of the wind shear shown in Fig. 2.6. . . . 38

2.9 Skew T-log  $p$  diagram of environmental conditions for a Barbados trade-wind cumulus cloud (data taken from <http://www.knmi.nl/~siebesma/gcss/bomexcomp.append.html>). The description of the lines and ordinates is as in Fig. 2.3. The simulation date is set to 4 August 2000. . . . . 39

2.10 Same as Fig. 2.4. but for Barbados trade wind cumulus. . . . . 40

2.11 Vertical profile of the temporally and spatially averaged net downward SW flux normalized to the incoming SW at the TOA (top of the atmosphere) for the cloud of (a) Oakland case without wind (Fig. 2.4), (b) Oakland case with wind shear (Fig. 2.5), (c) Hawaii case without wind (Fig. 2.7), (d) Hawaii case with wind shear (Fig. 2.8), (e) Barbados case (Fig. 2.10): cloud (closed circle), halo (open circle), and far-ambient (solid line only). The area average is illustrated in Fig. 2.12 . . . . . 41

2.12 Illustration of the increased net downward flux below cloud base (see text for details). The shaded columns are halo columns, and between them is the cloud column. The solid line is the cloud, and the the region between the dotted line and the cloud defines the cloud halo. The two bold horizontal lines represent levels  $z_i$  and  $z_{i+1}$  with  $z_{i+1} > z_i$ . . . . . 42

2.13 SW heating rate ( $\text{K hr}^{-1}$ ) for the small cumulus of Fig. 2.7. In-cloud values are not shown in order to show details in the halo region. Cloud boundaries are defined by the  $0.01 \text{ g m}^{-3}$  contour line for the cloud LWC. . . . . 43

2.14 Vertical profile of the temporally and spatially averaged SW heating rate for the cloud of (a) Oakland case without wind (Fig. 2.4), (b) Oakland case with wind shear (Fig. 2.5), (c) Hawaii case without wind (Fig. 2.7), (d) Hawaii case with wind shear (Fig. 2.8), (e) Barbados case (Fig. 2.10): halo (open circle) and far-ambient (closed circle). . . . . 44

2.15 The radiative effect of the cloud halo, computed by subtracting the domain-averaged heating rate in the presence of the halo from that in the absence of the halo, for (a) Oakland case without wind, (b) Oakland case with wind shear, (c) Hawaii case without wind, (d) Hawaii case with wind shear, (e) Barbados case. These heating rate profiles are temporally averaged over the cloud lifetime and spatially averaged over the horizontal domain. . . . . 45

3.1 Schematic of the Aerodyne Research, Inc. spectroscopic water vapor sensor. Also shown are the relative intensities of the frequency components produced by the Zeeman (magnetic) splitting of the lamp output. The lower frequency component,  $\nu_1$ , is absorbed by the water vapor in the absorption cell, producing a net AC signal at the detector. See text for a full explanation. . . 74

3.2 Flight path for the cumulus cloud at 0047 UTC, on August 8, 2001. A total of 14 traverses (green) are shown. Observation 1 represents traverses 1 through 8; observation 2 represents traverses 9 through 14. Red circles denote the cloud boundary. . . . . 75

- 3.3 Skew  $T$ - $\log p$  diagram of the ambient sounding profile on August 8, 2001 taken for the extensively studied cloud (in Sections 3.3 and 3.4) at 0047 UTC, 21.57°N, 156.82°W. Temperature and dewpoint temperature profiles are represented by thick lines. The skewed abscissa is temperature (°C), and the ordinate is pressure (hPa). Dotted lines (K) represent dry adiabats. Curved, dashed lines (°C) are pseudoadiabats. Straight-dashed lines ( $\text{g kg}^{-1}$ ) are isopleths of the saturation water vapor mixing ratio. The north-south wind is not shown. . . . . 76
- 3.4 Vertical profiles of (a) cloud width and (b) the horizontally averaged and maximum cloud LWC for each traverse for observations 1 (traverses 1–8) and 2 (traverses 9–14). . . . . 77
- 3.5 Specific humidity ( $\text{g kg}^{-1}$ ) distribution on aircraft traverse 12. The dotted line is the actual data, and the solid line through it are the smoothed data (11-point moving average of the dotted line). The shaded area is the cloud liquid water content ( $\text{g m}^{-3}$ ). The cloud boundary is defined by a liquid water content of  $0.01 \text{ g m}^{-3}$ , and is displayed as “c”, and the edge of the halo is denoted by “h” in the humidity distribution. The horizontal line in the cloud area is the in-cloud specific humidity,  $\bar{q}_{vc}(z)$ , while the two lines outside the cloud are the environmental specific humidity  $\bar{q}_{env}(z)$ . The distance from the beginning of this traverse is given on the top axis. . . . . 78
- 3.6 Same as Fig. 3.5 but for traverse 4. The ambient specific humidity is defined as that at the start and end of the traverse. . . . . 79

3.7	Vertical profile of cloud halo width at the west and east sides of the cloud. versus the altitude normalized with the cloud depth for observations 1 and 2. The normalized altitudes of 0 and 1 refer to cloud base and cloud top, respectively. Below the inversion base, the west side relative to the cloud is the downshear direction. . . . .	80
3.8	Vertical profile of the halo width for the sampled clouds shown in Table 3.2 in the (a) downshear and (b) upshear directions of the cloud. The data points are categorized into five altitude bins. The thick solid line is the averaged halo width of each altitude bin. Error bars indicate the standard deviations of the data points in each altitude bin. The square symbols indicate the observational data points. . . . .	81
3.9	(a) Flight track during sampling of a convective cumulus cloud from UTC 00:50 to 02:04 on August 60 2001, with different altitudes labelled A–K; (b) Vertical profile of total particle concentration and particle concentration in the size range, 0.1 to 3.5 $\mu\text{m}$ diameter; (c)–(e) dry aerosol size distributions in free troposphere, transition region, and marine boundary layer; (f)–(g) Particle concentrations measured by three CNCs when newly formed particles were detected. . . . .	82
3.10	Averaged cloud droplet size distribution for traverse 7, together with continuous fitted gamma distribution [Eq. (3.2)] used for simulation. . . . .	83

3.11	Simulated cloud (LWC contour line of $0.01 \text{ g m}^{-3}$ ) and cloud halo (shaded regions) at $t = 16$ min. Below the inversion base, the west side of the cloud is the downshear side. The dotted line is the isopleth of turbulent kinetic energy of $0.1 \text{ m}^2 \text{ s}^{-2}$ . The vertical profile of horizontal wind speed is shown as horizontal arrows. . . . .	84
3.12	Vertical profiles of the maximum (a) LWC and (b) specific humidity from RAMS simulation at $t = 16$ min, observation 1 and observation 2. . . . .	85
3.13	Vertical profile of the simulated cloud halo as shown in Fig. 3.11 at the west side and east side of the cloud at $t = 16$ min. Wind is from the east. Below the inversion base, the west side relative to the cloud is the downshear direction. . . . .	86
3.14	Halo (shaded regions) simulation by imposing a stronger wind shear into the simulation as shown in Fig. 3.11 for (a) mature stage and (b) dissipation stage. The turbulent mixing area is encompassed by the isopleth (dotted) of turbulent kinetic energy of $0.1 \text{ m}^2 \text{ s}^{-2}$ . The vertical profile of horizontal wind speed is shown as horizontal arrows. The LWC contour line (solid) of $0.01 \text{ g m}^{-3}$ represents the cloud. . . . .	87
3.15	Domain-averaged (over the $x$ -axis) SW atmospheric column (surface to 3.4 km) absorption ( $A$ ) as a function of simulation time in the presence and absence of humidity halo. The dotted line is the halo-enhanced atmospheric absorption ( $\Delta A$ ). . . . .	88

- 3.16 Increase of the atmospheric heating rate in the presence of a cloud halo over that in the absence of a halo for the simulation shown in Fig. 3.11. Contour lines (green dashed) are 0.01, 0.03, 0.06, 0.12, 0.15, 0.2, 0.3 K hr<sup>-1</sup>. The LWC contour line (purple solid) of 0.01 g m<sup>-3</sup> is the cloud, and shaded regions (yellow) are the halo. Two shaded contour plots provide an expanded view of the enhanced heating rate near the cloud top. . . . . 89
- 4.1 Initial sounding profile for a lightly drizzling stratocumulus cloud. Solid line is for BASE run (data from Moeng et al. 1996); dotted line is for SST2 run; dashed line is for SST4 run. . . . . 124
- 4.2 Effect of region size on averaged cloud optical depth as a function of aerosol number concentration. BASE run (solid line) performed over a horizontal region of 1.1 km × 1.1 km, while the same configuration but a domain of 3.3 km × 3.3 km (BASELG) is shown as the dotted line. The average is performed over the horizontal domain during the final 3 h of the simulation. Error bars represent the standard deviation of the domain-averaged values. 125
- 4.3 Cloud LWP for seven simulations defined in Table 4.1. Data points are averages over the horizontal domain during the final 3 h of the simulation. . 126
- 4.4 Super-micron sea salt effect (see section 5 for details) for weakly precipitating stratocumulus cloud (a)  $N_c$ , (b)  $r_e$ , (c) accumulated surface precipitation, (d) cloud LWP, (e)  $\tau$ , and (f) cloud albedo for BASE, UGSALT, and BASESW. The accumulated surface precipitation is summed over the six-hour simulations. 127
- 4.5 Vertical profiles of sedimentation flux (solid line, lower axis) and LWC (dotted line, upper axis) for BASE  $N_a=50$  cm<sup>-3</sup>, horizontally averaged over the final 3 h of the simulation. . . . . 128

4.6	Vertical profiles of the temporally (last 3 hours) and horizontally averaged (a) vertical velocity variance, (b) water vapor mixing ratio, (c) potential temperature, and (d) cloud LWC. Solid line represents the non-drizzling cloud (BASE, $N_a = 2000 \text{ cm}^{-3}$ ) and the dotted line represents the drizzling cloud (BASE, $N_a = 50 \text{ cm}^{-3}$ ). . . . .	129
4.7	Temporal evolution of horizontally averaged cloud mixing ratio ( $\text{g kg}^{-1}$ ) for (a) BASE, (b) SST2, and (c) SST4. Aerosol number concentration is $50 \text{ cm}^{-3}$ . Cloud optical depth versus cloud LWP for clean and polluted cases for eight simulations. Data points are averaged over the horizontal domain. . . . .	130
4.8	Cloud optical depth for seven simulations defined in Table 4.1. Data points are averages over the horizontal domain during the final 3 h of the simulation. . . . .	131
4.9	Cloud optical depth versus cloud LWP for clean and polluted (data points below the constant line of $r_e = 12 \mu\text{m}$ ) cases for eight simulations. Data points are averaged over the horizontal domain; except that $r_e$ is averaged over the upper one-third of the cloud layer. $r_e$ is colored by its value given in the colorbar. Overlain dashed lines are the theoretical $r_e$ defined in Stephens (1978). . . . .	132
4.10	Regression of $N_c$ versus $N_a$ at every binned LWP with bin size of $5 \text{ g m}^{-2}$ with 5 min sampling frequency (for $\text{LWP} \geq 25 \text{ g m}^{-2}$ , data points are represented by plus) during the final 3 h (dotted lines). The line solid line is the averaged results of the dotted lines. The short thick line is from DYCOMS-II measurements (Fig. 1 of Twohy et al. 2005). . . . .	133

4.11 (a) Linear regression results of the dry sea salt aerosol radius with the corresponding wet radius at  $RH = 97\%$ ,  $r_{97}$ , at 285K for 200 size bins in the dry size range of  $r_g(\text{giant})/10 \sigma_g(\text{giant}) = 0.05 \mu\text{m} - 10 r_g(\text{ultra-giant})/\sigma_g(\text{ultra-giant}) = 180 \mu\text{m}$ ; (b) Spectrum of fractions of the number of activated giant- and ultra-giant- sea salt aerosols mapped to the 36 cloud droplet size bins in the model. . . . . 134

4.12 Initial sounding profile for a heavily precipitating stratocumulus cloud (data from Stevens et al. 1998). . . . . 135

4.13 Same as Fig. 4.2 but for the BASEH run. . . . . 136

4.14 Temporal evolution of domain averaged cloud droplet number concentration (left) and surface precipitation rate (right) at high aerosol loadings ( $N_a = 1500, 2000, 2500 \text{ cm}^{-3}$ ) for BASEH, GSALTH, and UGSALTH. . . . . 137

4.15 Simulation results of the ASTEX sounding (Fig. 4.12) on different sulfate aerosol concentrations as seen on (a)  $N_c$ , (b)  $r_e$ , (c) accumulated surface precipitation, (d) cloud LWP, (e)  $\tau$ , and (f) cloud albedo. Data are domain-averaged during the final 1 hour of the simulation. The accumulated surface precipitation is summed over the 6 h simulations. . . . . 138

4.16 Layer-averaged drop spectra for  $N_a = 2000 \text{ cm}^{-3}$  at selected heights at  $t = 5 \text{ h}$ . Solid line is BASEH run and dotted line is UGSALTH. . . . . 139

4.17 Similar to Fig. 4.15 except for the inclusion of aerosol washout by drizzle drops (WASHOUTH). . . . . 140

4.18 Simulation results of the ASTEX sounding (Fig. 4.12) on different sulfate aerosol concentrations as seen on (a) $N_c$ , (b) LWP, (c) $\tau$ , and (d) cloud albedo for the BASEHDIU early morning (local standard time 08-10h), noon (11-13h), and afternoon (14-16h). . . . .	141
---	-----

# List of Tables

2.1	Summary of case studies. . . . .	29
2.2	Temporally and spatially averaged halo SW radiative forcing at the surface of the earth. . . . .	30
3.1	Airborne and ground-based measurements of cloud halos . . . . .	71
3.2	Characteristics of nine trade wind cumulus clouds studied . . . . .	72
3.3	Cloud halo statistics for the current study as compared with Perry and Hobbs (1996) . . . . .	73
4.1	Conditions of simulations . . . . .	121
4.2	Relative change in averaged cloud properties due to introduction of large sea salt aerosols into BASEH simulation <sup>a</sup> . . . . .	122
4.2	Continued . . . . .	122
4.3	Evaluation of aerosol indirect effect of Eq. (4.15) and the contribution from the first and second aerosol indirect effect	

$$\left. \frac{\partial \ln \tau}{\partial \ln N_a} \right|_{D, \text{SST}} = \alpha + \beta \left. \frac{\partial \ln \text{LWP}}{\partial \ln N_a} \right|_{D, \text{SST}}$$

# Chapter 1

## Preface

### 1.1 Introduction

Clouds are a truly multiscale atmospheric phenomenon from a boundary layer cloud scale of several hundreds of meters up to an organized precipitating meso- to synoptic-scale system of several tens of kilometers. Clouds play an important role in global scales — the latent heat released by clouds is one of the main engines that drives the global atmospheric circulation, one of the key components in Earth’s hydrology cycle, and the most important of all, they play a major role in determining the earth’s global radiation budget, and thereby they have a profound impact on the earth longtime climate state. Atmospheric aerosols can intimately interact with clouds by acting as cloud condensation nuclei, hence determining the initial cloud droplet number concentration, albedo, precipitation formation and lifetime of warm clouds. Anthropogenic aerosols, for example, the major component — sulfate, have substantially increased from pre-industrial times to the present-day. How this increase of the anthropogenic source will change our climate is of great concern to human beings. The way that aerosols perturb the earth radiation indirectly via the cloud process is generally characterized by two types: The first aerosol indirect effect, the so-called the Twomey effect (Twomey 1977), refers to the increase of cloud shortwave albedo

due to the enhancement in the cloud droplet number concentration for a constant liquid water content. The second aerosol indirect effect refers to the decrease in precipitation efficiency, and thus, the increase in cloud lifetime, due to more but smaller cloud droplets (Albrecht 1989). The aerosol indirect forcing is currently believed to be of a negative sign by the atmospheric sciences community; however, the uncertainty of the second aerosol indirect forcing is too large to have the simulated quantitative estimates on the IPCC 2001 report (Houghton et al. 2001). The focus of this thesis is to understand how clouds, specifically warm clouds, can affect the earth radiation budget. The thesis consists mainly two parts. In the first part, an interesting phenomenon of the cloud humidity halo, which is the regions of enhanced humidity in the vicinity of cumulus clouds, is explored through the combination of a LES cumulus simulation and a 3D radiative transfer model. The humidity halo, radiatively, can absorb the incoming solar radiation and reduce the solar radiation reflected to space. Therefore, the humidity halos result in a positive TOA (top of the atmosphere) forcing and negative surface forcing. The cloud halo dynamical structure and the enhanced atmospheric heating due to the halo with the respect to the cloud temporal evolution is investigated. The modeled halo is also compared with the statistical analysis of the observed halos from an aircraft sampling campaign of the trade wind cumuli – “Cloud Halo” conducted in Hawaii, 2001. The implication for the new particle formation in the cloud halo regions is also investigated. The second part of this thesis is to study the anthropogenic aerosol indirect effect by a LES (Large Eddy Simulation) simulation of the stratocumulus clouds. For this purpose, the cloud microphysical module uses the freely evolved explicit bin microphysics, in which the cloud droplet spectrum is divided into droplet size bins, instead of the bulk microphysics constrained by the gamma shape droplet size distribution in the first part. The aerosol activation is also modified based on the Köhler

theory. The important parameters for assessing the aerosol indirect effect are the cloud optical depth, aerosol number concentration, and cloud liquid water path. In this part, we investigate the sensitivity of the cloud optical depth to the aerosol number concentration and the cloud liquid water path. The former is due to the cloud microphysics (i.e., aerosol activation) and the latter is due to the meteorological/dynamical effect (i.e., SST and large-scale subsidence). The first and the second aerosol effects from the model simulation results are discussed and their contributions to the overall aerosol indirect forcing are analyzed. The giant sea salt aerosol impact on the simulated cloud dynamical and radiative properties is also presented.

## 1.2 Organization of the thesis

Chapter 1 is the introduction. The numerical simulation of dynamical structure and temporal evolution of the humidity halos and the possible mechanisms for the radiative impacts of the humidity halos are presented in Chapter 2. Data analysis from the field measurement of the Hawaiian trade wind cumuli and the associated humidity halos are given in Chapter 3. The increased solar absorption of considering a humidity halo relative to no halo calculated by a 3D radiative transfer model and the implication for new particle formation is also presented in this chapter. In Chapter 4, a series of 98 three-dimensional LES simulations of the stratocumulus are performed to study the aerosol indirect effect. Finally, Chapter 5 discusses the implication for future works.

## Chapter 2

# Cloud halos: numerical simulation of dynamical structure and radiative impact

Reference: Lu, M.-L., R. A. McClatchey, and J. H. Seinfeld, 2002: Cloud Halos: Numerical Simulation of Dynamical Structure and Radiative Impact. *J. Appl. Meteor.*, **41**, 832–848.

### 2.1 Abstract

Significant enhancements in humidity around cumulus clouds, the “cloud halos” observed in many aircraft penetrations, are simulated using a three-dimensional dynamic model. Five case studies show that humidity halos occur mainly near lateral cloud boundaries, and also at cloud top and base when the cloud dissipates. The humidity halo broadens as the cloud ages and is also broader in the presence of wind shear than in its absence, especially on the downshear side of the cloud. The broadband calculation over the solar spectrum (0.2–4.0  $\mu\text{m}$ ) shows that the SW heating rate in the halo is about 11–18% larger than the ambient environmental heating rate. The strongest halo-induced surface SW radiative forcing for all cases studied is about  $-0.2 \text{ W m}^{-2}$ , approximately a 0.02% change from the net downward surface SW flux without a halo.

## 2.2 Introduction

Significant enhancements in humidity above that in the cloud-free atmosphere have been found to occur on the downshear side of cumulus clouds (Malkus 1949, 1954; Ackerman 1958; Telford and Wagner 1980; Radke and Hobbs 1991; Hobbs and Radke 1992; Perry and Hobbs 1996; Kollias et al. 2001). These regions of high humidity, termed cloud or humidity halos, can extend out to substantial distances from the cloud itself. Fig. 2.1 depicts schematically a cloud halo region.

A number of fundamental issues emerge as a result of the existence of humidity halos: What are the horizontal and vertical extents of halo regions for different classes of cumulus clouds? What is the temporal evolution of the halo relative to the cloud evolution? How does halo development depend on prevailing wind conditions? What effect does the existence of a humidity halo have on radiative transfer in the atmosphere? For example, how do shortwave (SW) absorption and heating for the halo compare to those of the cloud itself and to that of the ambient atmosphere? Detailed numerical simulations of cloud halo development and lifetimes have not been reported previously. Our goal in the present paper is to explore the dynamical and radiative aspects of cloud halos through numerical simulation using state-of-the-art dynamic and radiative transfer models.

Some of the early measurements of tropical (trade wind) cumulus were conducted in the Caribbean. Trade wind cumulus patches observed in the Caribbean are roughly 30 km in diameter and contain many individual 1–2 km cumulus clouds (Malkus 1949, 1954). Wide clear areas typically separate these patches. Early aircraft-based studies of trade wind cumulus emphasized turbulence within clouds and in the surrounding clear air. Malkus found that a region of turbulence extended asymmetrically around a cloud with its maximum

in the downshear (and downwind) direction (some confusion over this asymmetry occurs in her paper because of an apparent wind direction definition opposite to convention). She developed a model of a cloud and its turbulent structure, suggesting that the cloud grows in the upwind (and upshear) direction and decays on the downwind (and downshear) side. In this way she speculated that the cloud leaves its influence behind, even as the observable cloud decays. The work of Ackerman (1958) extended these concepts based on a much larger aircraft-based experimental program entailing 379 penetrations of 78 cumulus clouds. Ackerman also found that the cloud develops in the upshear direction and dissipates in the downshear direction, leaving behind a region of “cloud influence” characterized by clear air turbulence. She found time constants of 10 – 25 min to be significant for development and decay processes. And Ackerman appears to be the first to suggest that a humidity halo might accompany these areas of “influence,” even going a step farther as follows: “If the turbulent regions are ‘old’ cloud air from which the liquid water has evaporated, they must also be regions of high humidity and consequently preferred areas for new cloud development.” These regions of high humidity do represent preferred areas for new cloud development, as was later shown in the observations of Telford and Wagner (1980). Aircraft measurements of small cumulus by Radke and Hobbs (1991) and Hobbs and Radke (1992) demonstrated that cumulus clouds are surrounded by regions of high humidity out to distances of several cloud radii from the cloud center.

Perry and Hobbs (1996) found significant humidity enhancements in the clear air, particularly downshear of small to medium-sized (0.4–4.3 km deep) cumulus clouds over the northeast Pacific Ocean near the Washington and Oregon coastlines. The humidity halo was found to broaden with cloud age, and the orientation relative to the vertical wind shear was the most important factor determining the frequency and average size of the halo. For

the clouds sampled, humidity halos were found on the downshear, cross-shear, and upshear sides of the clouds 74%, 40%, and 36% of the time, respectively; their average size was largest downshear and smallest upshear. Bretherton and Smolarkiewicz (1989) and Perry and Hobbs (1996) suggested that in the absence of vertical wind shear, air is detrained from the cloud equally in all directions in the layer where the in-cloud buoyancy decreases with height. In the presence of vertical wind shear, the clear-air humidity field on the downshear side is enhanced by cloud evaporation in the detrained air, while on the upshear side it is limited by the growth of cloud engulfing the detrained air. Recently radar measurements of fair-weather cumuli (Kollias et al. 2001) also showed the moisture gradient to be enhanced far beyond the lateral cloud boundaries.

Radiative transfer in the halo region is a complex issue (Fig. 2.2). The existence of a humidity halo changes not only the radiation balance of the clear sky adjacent to the cloud but also that of the cloud itself. Enhanced short-wave (SW) absorption exists in the halo relative to that far from the cloud, due to absorption of both incident solar radiation and the scattered SW radiation from the cloud. Podgorny et al. (1998) computed enhanced column absorption for broken clouds assuming that the water vapor in the cloud gaps is its saturation value as opposed to an unsaturated water vapor field generally used in the climate model. Prior studies have focused on the enhanced column absorption due to a horizontally homogeneous water vapor layer overlying the cloud top (Davies et al. 1984; Podgorny et al. 1998; Li and Trishchenko 2001), clouds with a water vapor field being its saturation value relative to the drier background (Crisp 1997), and the increase in the background water vapor (Arking 1996). None has considered radiative effects of inhomogeneous three-dimensional (3D) water vapor fields associated with clouds beyond their lateral boundaries, below their bases, or above their tops by either measurement or numerical modelling.

In this paper, we present a numerical study of cumulus cloud development based on several case studies, focusing on addressing the following questions: What are the horizontal and vertical extents and time evolution of humidity halos for several generic cloud-forming conditions? Are there features common to humidity halos for different cumulus conditions? How much does a humidity halo enhance radiative heating in the whole spatial domain including cloud and halo? Section 2.3 presents a brief description of the dynamical cloud model and radiative transfer model used. Discussions of several case studies are presented in section 2.4. Section 2.5 addresses the radiative effect of the humidity halo.

### **2.3 Dynamic cloud model**

The dynamic model used in this study is the LES (Large Eddy Simulation) version of the Regional Atmospheric Modeling System (RAMS) developed at Colorado State University (Pielke et al. 1992). This Eulerian 3D model is nonhydrostatic and compressible. The prognostic variables include the three velocity components, the Exner function (the pressure variable), the ice-liquid water potential temperature (Tripoli and Cotton 1981), and the total water mixing ratio. The LES implementation uses a “1.5th order” subgrid scheme adapted from Deardorff (1970), predicting the turbulent kinetic energy in order to evaluate eddy mixing coefficients when using very fine horizontal grid spacing to resolve convective motions. The parameterization of Harrington (1997) is used in RAMS to update the radiative tendency, i.e., the temperature change due to radiation. This radiation scheme assumes a two-stream approximation, and therefore is only used for cloud simulation (see the discussion about the 3D radiative transfer model later in the text).

### 2.3.1 Microphysical parameterization

The standard microphysical scheme in RAMS is a bulk parameterization, featuring a generalized gamma size distribution function for hydrometeors,

$$n(D) = \frac{N_t}{\Gamma(\nu)} \left(\frac{D}{D_n}\right)^{\nu-1} \frac{1}{D_n} \exp\left(-\frac{D}{D_n}\right) \quad (2.1)$$

where  $N_t$  is the total number concentration of individual hydrometeors of diameter  $D$ ,  $\nu$  is the shape parameter, and  $D_n$  is the characteristic diameter of the distribution. In the pure warm-cloud simulations to be presented here, rain water number concentration is the only predicted hydrometeor property, while rain and cloud water mixing ratios are diagnosed (Walko et al. 1995).

### 2.3.2 Radiative transfer model

O’Hirok and Gautier (1998), using a 3D Monte Carlo-based radiative transfer model with high spectral and spatial resolution, investigated solar radiation within a cloudy atmosphere and demonstrated that plane-parallel one-dimensional (1D) assumptions used in general circulation models can underestimate atmospheric absorption in comparison to a 3D calculation. Wendisch and Keil (1999) and Arking (1996) also show that 3D radiative transfer models are required to perform accurate radiative transfer calculations in the presence of horizontal cloud inhomogeneities.

SHDOM (Spherical Harmonic Discrete Ordinate Method; Evans 1993, 1998), an efficient and flexible 3D atmospheric radiative transfer model that solves the radiative transfer equation to a high degree of accuracy, is employed in the present study. SHDOM can compute unpolarized, monochromatic and broadband (with correlated  $k$  distribution; Fu and Liou

1992), shortwave (0.2–4.0  $\mu\text{m}$ ) and longwave (4.0–100  $\mu\text{m}$ ) radiative transfer in a vertically inhomogeneous atmosphere. Trautmann et al. (1999) show that spatial patterns of the actinic flux fields calculated by the two-dimensional (2D) Monte Carlo method and SHDOM agree closely, to within 1–2% when horizontally averaged. SHDOM enables radiance at any angle, hemispheric fluxes, net fluxes, mean radiances, and net flux convergence to be obtained anywhere in the domain. The source function of the radiative transfer equation is computed on a discrete spatial grid, with the angular variable represented by a truncated series of spherical harmonics. The radiative transfer equation is then integrated along discrete ordinate directions throughout the spatial grid in order to represent the streaming of photons. The solution algorithm takes advantage of an adaptive grid technique, which automatically places additional grid points during the iteration process in those regions where the optical properties of the medium vary most strongly. Cloud optical properties are computed through Mie theory.

Nongray gaseous absorption by methane, ozone, nitrous oxide, carbon dioxide, and water vapor are treated by the correlated  $k$  distribution (Fu and Liou 1992). SHDOM is modified by calculating the  $k$  value at each grid cell. In this way, the 3D water vapor distribution can be considered. The correlated  $k$  distribution has six solar bands with boundaries at 0.2, 0.7, 1.3, 1.9, 2.5, 3.5 and 4.0  $\mu\text{m}$ . A total of 54 monochromatic calculations (54  $k$ 's) are required across these solar bands. For the SW radiation, gaseous absorption by water vapor (2500–14500  $\text{cm}^{-1}$ ), ozone (in the ultraviolet and visible), carbon dioxide (2850–5250  $\text{cm}^{-1}$ ), and oxygen (A, B, and  $\gamma$  bands) are taken into account.

### 2.3.3 Model Setup

It is necessary to initialize several parameters in RAMS prior to simulating cloud development. The cloud droplet distribution must be specified. For this purpose, the cloud droplet gamma distribution in Eq. (2.1) is used, with shape coefficient  $\nu = 3.87$  (Chylek and Ramaswamy 1982, Table 2) and  $N_t = 340 \text{ cm}^{-3}$  for marine cumulus. A warm rain process is considered, taking the mean raindrop diameter to be 0.1 mm. We simulate marine cumulus, using the constant sea surface temperatures of 286 K, 300 K and 300 K for the Oakland, Hawaii and Barbados cases respectively (see section 2.4). The ocean surface albedo is taken to be 0.06 for all radiation wavelengths. A Rayleigh sponge layer is applied adjacent to the top of the domain to damp the reflection of gravity waves from the upper boundary. The upper and lower boundaries are rigid-lid and no-slip, and the lateral boundary conditions are cyclic in both the  $x$  and  $y$  directions. The radiation tendency is updated every 10 min using the parameterization of Harrington (1997). Horizontal resolution is 100 m. A stretched vertical grid is used, with a resolution coarsening upward from 40 m near the surface to a maximum of 1 km near the top of the domain, with a stretching ratio of 1.1. There is a total of  $60 \times 60 \times 37$  grid cells (except for the Barbados cumulus simulation; see section 2.4.3). The simulation time step is 1 s, selecting the simulated local hour near the time of the minimum solar zenith angle for each case (Table 2.1). The above parameter specifications are applied to all case studies.

In the 3D SHDOM calculations, the solution accuracy for radiative fluxes is set to  $0.00001 \text{ W m}^{-2}$ . There are 8 zenith angles and 16 azimuth angles for angular resolution. Adaptive grid splitting criteria for the six solar bands are 1, 1, 0.1, 0.2, 0.2, and  $0.2 \text{ W m}^{-2}$ , above which the grid cell is halved to increase spatial resolution in optically thick media. The solar band calculation uses the delta-M scaling of the medium and the Nakajima and

Tanaka (1988) method of computing radiances.  $\text{CO}_2$ ,  $\text{CH}_4$ , and  $\text{N}_2\text{O}$  mixing ratios are set to 360, 1.6, and 0.28 ppmv, respectively. Molecular Rayleigh scattering as described by Fu and Liou (1992) is included. Air density is taken from RAMS output. The ozone mixing ratio is obtained from McClatchey et al. (1972). The atmospheric profile between the top of the atmosphere and the top of the RAMS domain is taken from McClatchey et al. (1972). Periodic boundary conditions are applied for SHDOM, so that photons that exit one side of the grid re-enter at the opposite side.

## 2.4 Simulations of the cloud and associated halo

In order to study the properties of cloud halos around different types of cumulus clouds, several cases are simulated. The first case, representing shallow cumulus clouds similar to those observed by Perry and Hobbs (1996) (hereafter termed “Oakland case”), performs simulations both without wind and with wind shear. The second case represents cumulus clouds typical of Hawaii (hereafter referred to as “Hawaii case”), for the same wind scenarios. The third case is a Barbados trade wind cumulus (hereafter termed “Barbados case”) that has been studied previously (e.g., GEWEX 2000). The wind profiles for the Oakland and Hawaii cases are idealized, with only the  $u$ -component (east-west wind) present, so that the simulated moving cloud can be tracked easily.

### 2.4.1 Shallow cumulus off the coast of northern California

To simulate shallow cumulus clouds typical of those observed by Perry and Hobbs (1996), we chose 26 October 2000 on the basis of satellite imagery showing numerous cumulus clouds off the coast of northern California. The closest radiosonde site is Oakland, CA, from which the model is initialized with the horizontally homogeneous composite sounding shown in

Fig. 2.3.

Similarly to Kogan (1991), a cumulus cloud is triggered by imposing a horizontally Gaussian-shaped perturbation  $\theta'$  on the potential temperature in the center of the domain. This impulse, assigned sinusoidal variation in the vertical, is effectively 1 km wide and confined to the lowest 2 km:

$$\theta' = 0.1 \exp \left[ -\frac{(x - x_0)^2 + (y - y_0)^2}{R^2} \right] \sin^2 \left( \frac{\pi z}{H} \right) \quad (2.2)$$

where  $(x, y)$  and  $z$  represent the horizontal and vertical coordinates, respectively,  $(x_0, y_0)$  is the horizontal location of the central axis,  $R$  is an effective perturbation radius and  $H$  is the depth. In this case,  $(x_0, y_0) = (3 \text{ km}, 3 \text{ km})$ ,  $R^2 = 1 \text{ km}^2$ , and  $H = 2 \text{ km}$ . This warmer area is also initially humidified by a  $1 \text{ g kg}^{-1}$  water vapor mixing ratio excess below 988 hPa to accelerate cloud formation; when the same simulation was repeated without this humidity perturbation, no cloud formed. The initial sounding is probably not sufficiently moist for clouds to form spontaneously without such a perturbation.

We consider first the case with no mean horizontal wind. The cloud is formed immediately upon starting the simulation. The cumulus reaches its mature stage at 14 min (Fig. 2.4), when it has a maximum in-cloud vertical velocity of  $3.8 \text{ m s}^{-1}$ , and then starts to dissipate after 18 min when the maximum cloud liquid water content (LWC) attained is  $1.58 \text{ g m}^{-3}$ . The cloud lifetime for this case is 28 min, which is typical for small cumulus. The cloud has a virtually symmetric circulation pattern, with an updraft core surrounded by downdrafts. The slight asymmetry in the cloud and halo distribution is the result of non-uniform radiative heating horizontally.

To measure the horizontal extent of the enhanced humidity around the cloud at a given

height, we follow Perry and Hobbs (1996) and represent the humidity in the halo region as decaying exponentially from the average absolute humidity in the cloud at that height,  $\bar{\rho}_{vc}(z)$ , to the background humidity far from the cloud,  $\bar{\rho}_{venv}(z)$ . In doing so, we define the absolute humidity at the outer edge of the halo arbitrarily, based on the  $e$ -folding decay of the profile, as schematized in Fig. 2.1,

$$\rho_{ve}(z) = \bar{\rho}_{vc}(z) - \{[\bar{\rho}_{vc}(z) - \bar{\rho}_{venv}(z)](1 - e^{-1})\} \quad (2.3)$$

The humidity halo is then the region in which the absolute humidity around the cloud exceeds the  $e$ -folding value  $\rho_{ve}(z)$ . The average is performed along the horizontal axis (i.e., the  $x$ -axis in this paper) at each altitude. In the current simulation, the grid points satisfying  $(x, y) = (200 \text{ m}, 200 \text{ m})$  are used as the far-ambient reference column, near which the atmospheric properties are close to horizontally uniform. In addition to the halo near the cloud lateral boundaries, evident humidified regions exist above the cloud top or beneath cloud base in the simulation. In these regions after the cloud fully dissipates, there is no reference value  $\bar{\rho}_{vc}(z)$ . Meanwhile, the absolute humidity at arbitrary  $z$  fluctuates, especially in the presence of wind shear. Therefore, to have a uniform definition of the humidity halo region under all conditions when the averaged cloud LWC at arbitrary  $z$  is zero, we use  $\bar{\rho}_v(z)$ , the horizontally averaged (i.e., the  $x$ -axis in this paper) absolute humidity. Thus the humidity halo is defined when

$$\rho_v(z) > \bar{\rho}_v(z), \text{ and } \frac{\rho_v(z) - \bar{\rho}_v(z)}{\bar{\rho}_v(z)} > 0.05 \quad (2.4)$$

The value of 0.05 is used to avoid noise in the humidity data. Based on the above definition,  $x$ - $z$  sections of the humidity halo region in Fig. 2.4 consist of the shaded grid boxes outside

the cloud in this figure, which depicts the entire simulated cloud evolution. The humidity halo occurs mainly at the lower cloud lateral region, and appears to be below the cloud base when the bottom of the cloud dissipates. Note that the humidity halo surrounds the cloud for the entire cloud life, and broadens during cloud dissipation. Perry and Hobbs (1996) found that the width of the humidity halo is closely related to the age of the cloud, with older clouds tending to exhibit enhanced humidity out to distances significantly greater than younger clouds; the humidity halo gradually broadens with time and is widest when the cloud dissipates.

We now add a vertical wind shear as shown in the sounding profile (Fig. 2.3) to the previous simulation. Because of the wind shear, the cloud, which generally moves with the horizontal wind, is no longer symmetric (Fig. 2.5). The maximum in-cloud vertical velocity and LWC are smaller than in the absence of wind, and the simulated cloud life is slightly shorter at 26 min. This simulation basically conforms with the conceptual model of cloud growth proposed by Ackerman (1958) and Telford and Wagner (1980), depicting a cumulus cloud as consisting of quasi-static turbulent entities that grow on the upshear side and decay on the downshear side. Evaporation of cloud droplets on the downshear side humidifies the clear air there; while the growth of new cumulus turrets limits the humidity modification on the upshear side. The humidity halo occurs mainly in the lower cloud lateral regions, but is more widely distributed vertically than in the absence of wind. The simulation clearly shows that the halo is broader on the downshear side than on the upshear side (e.g., 14 and 22 min in Fig. 2.5), is also broader than in the absence of wind, and widens with time. The vertical extent of the humidity halo parallels that of the cloud itself. After the cloud dissipates, a significant region with increased humidity remains.

### 2.4.2 Convective cumulus (Hawaii)

According to Wang and Chen (1998), trade wind conditions occur in the vicinity of the Hawaiian Islands about 70% of the year. Their maximum incidence is in August, when they occur 92% of the time. These trade winds are a reflection of a subtropical high-pressure center located north of the Hawaiian Islands near 45°N, 150°W. Associated with this subtropical high is the so-called trade wind inversion which produces a “lid effect”, preventing vertical motion from penetrating this inversion. This strong inversion, caused by subsiding air over the North Pacific Ocean, limits clouds to < 2-3 km in height where the temperatures are about 10°C. A typical August inversion is located near 2.2 km, according to Li and Chen (1999), and trade wind velocities are generally in the range of 6–9 m s<sup>-1</sup> out of the east-northeast (Chen and Nash 1994). The magnitude of the inversion is about 3.6 K. The surface water vapor mixing ratio in the marine boundary layer is about 14.5 g kg<sup>-1</sup>.

According to Takahashi (1977), typical Hawaiian cumulus cloud bases are ~0.5 km above sea level. He indicates that a cloud top of 2.2 km, when the base is at 0.5 km, represents a critical height for the initiation of rain. The trade wind zone typically contains both isolated cumulus clouds and “cloud lines”. Individual cumulus clouds are typically 1–2 km in diameter. When showers occur, their duration averages about 18 min, ranging from 10 to 30 min. Warner (1977), reporting on small marine cumulus off the coast of Australia, describes cloud liquid water and vertical motion having lifetimes of 20–60 min. He also notes the existence of a persistent strong updraft on the upshear side of the clouds, identifying this 10–15 min phenomenon with the cloud development phase.

Hawaiian cumulus clouds bear a relationship to large-scale stratocumulus “patches” and/or “cloud lines” moving in the easterly trade winds (Austin et al. 1996). These cloud

patches develop in the trade wind flow downstream of the large shallow stratocumulus cloud mass that covers much of the northeastern Pacific Ocean between Hawaii and California. Cloud pictures from polar-orbiting and geostationary satellites clearly show these cloud fields and the frequent patches containing many individual cumulus cells as the Hawaiian Islands are approached.

A convective cumulus cloud is simulated based on the sounding profile shown in Fig. 2.6, taken in Lihue, Kauai, HI on 8 August 2000 and selected based on satellite imagery. The convective potential energy in this situation favors deeper convection than the Oakland case. We impose an initial perturbation below 500 m in the central region of the domain, 1 km wide and described by Eq. (2.2) with  $H = 0.5$  km. The domain below 997 hPa is initially humidified by  $1 \text{ g kg}^{-1}$  in water vapor mixing ratio to expedite cloud formation. The simulated convective cloud and its halo in the absence of wind are shown in Fig. 2.7. The simulated Hawaii cloud properties are shown in Table 2.1. This case, as anticipated from the sounding profile, has larger maxima for the updraft velocity, cloud depth, and cloud LWC than the previous case. The halo occurs near the lateral cloud boundaries, spread out over the cloud depth during the mature stage. Then dissipation of the upper and middle portion of the cloud leaves a significantly humidified region above the cloud top in the center of the domain. The cloud basically broadens with time.

In the presence of wind shear (Fig. 2.6), the cloud forms at 10 min and moves rapidly with the easterlies in the cloud layer (Fig. 2.8). The simulated bulk cloud properties for the Hawaii cumulus with wind shear (Table 2.1) are consistent with the measurements reported by Takahashi (1977) for cumulus clouds in the vicinity of Hawaii. As expected, the horizontal extent of the simulated humidity halo is larger on the downshear side than on the upshear side and also increases with time. Dissipation of the cloud at the downshear

side leaves a broad humidity halo region which, as also seen in the Oakland case, is broader in the presence of wind shear than in the absence of wind.

### 2.4.3 Trade wind cumulus (Barbados)

Fair-weather cumuli play an important role in regulating the vertical structure of water vapor in the lowest 2 km of the atmosphere over vast areas of the oceans. Recent radar observations (Kollias et al. 2001) of marine fair-weather cumuli near Florida also show enhanced moisture extending far beyond the cloud lateral boundaries. For our third case study, we conduct a simulation of shallow cumulus convection similar to that studied in the model intercomparisons in GCSS (Global Cloud Systems Study) Working Group 1 (GEWEX 2000). The sounding profile (Fig. 2.9), measured during the Barbados Oceanographic Meteorological Experiment (BOMEX; Davidson 1968), was selected for representing a typical trade-wind boundary layer. The simulation is carried out on a  $60 \times 60 \times 75$  grid cell configuration with 100-m grid spacing in the horizontal and 40 m in the vertical. The domain is thus 6 km by 6 km in area, and 3 km deep. A time step of 1 s is used over the entire simulation.

Three distinct layers can be observed from the initial vertical profiles of  $\theta$  (potential temperature) and  $r_v$  (water vapor mixing ratio): a well-mixed layer up to 500m, a conditionally unstable layer from 500 to 1500 m, and then an inversion (Fig. 2.9). The simulation conditions are as described earlier, except that the sensible and latent heat fluxes at the surface are prescribed as

$$\langle w'\theta' \rangle = 8 \times 10^{-3} \text{ K m s}^{-1}$$

$$\langle w'r'_v \rangle = 5.2 \times 10^{-3} \text{ m s}^{-1}$$

where  $w$  is the vertical velocity. The prime denotes deviations from the domain average,

$\langle \rangle$ . The momentum fluxes are prescribed by

$$\langle u'w' \rangle = -u(u^{*2})/\sqrt{(u^2 + v^2)} \quad (2.5)$$

$$\langle v'w' \rangle = -v(u^{*2})/\sqrt{(u^2 + v^2)} \quad (2.6)$$

where  $u^* = 0.28 \text{ m s}^{-1}$ , and the velocities are averaged from the lowest two levels in the model. The GCSS simulation of trade wind cumulus was conducted by imposing numerous random perturbations in the domain, a technique which produced many cumulus clouds. To produce a single isolated cumulus cloud, an initial perturbation similar to that described in section 2.4.1 is applied, in which  $H = 360 \text{ m}$  and the domain below 999 hPa is initially humidified by  $1 \text{ g kg}^{-1}$  in water vapor mixing ratio to expedite cloud formation.

The simulated fair-weather cumulus cloud properties are in Table 2.1 and the simulated results are shown in Fig. 2.10. The cloud has a circulation pattern of an in-cloud updraft core, with a maximum vertical velocity of  $8.1 \text{ m s}^{-1}$  at 24 min, and a narrow downdraft region at the downshear side (not shown). Jiang and Cotton (2000) reported simulation results showing a maximum cloud water mixing ratio of  $1.6 \text{ g kg}^{-1}$  and a maximum vertical velocity of  $3 \text{ m s}^{-1}$ , both averaged over the cloud updraft region. Our maximum vertical velocity and cloud water mixing ratio are one-point values inside the cloud; therefore, we expect them to be larger than the updraft-region averaged values in Jiang and Cotton (2000). Radar observations in Miami, FL for fair-weather cumuli (Kollias et al. 2001) showed that a maximum vertical velocity of  $6 \text{ m s}^{-1}$  with smaller cloud depth than in our simulation (i.e., 700 versus 1400 m). We can expect the current simulation to have a higher vertical velocity since the modeled cloud developed much deeper than what Kollias et al. (2001) observed. The humidity halo exists initially near the lower portions of the

lateral cloud boundaries, broadening with time. When the cloud starts to dissipate at the downshear side, halo regions appear both at the lateral cloud boundaries and above the cloud top. A broad halo remains after the cloud is totally dissipated.

#### 2.4.4 Summary of case studies

A summary of the simulated cloud properties of these case studies is given in Table 2.1. From the above five simulations, we can conclude that cloud halos appear at the lower cloud lateral regions at the early cloud stages and then start to spread vertically. The vertical extent of the humidity halo parallels the associated cloud depth. Deeper cloud, such as in the Hawaii case, favors a more vertically extensive halo. When the upper or lower portion of the cloud dissipates, the humidity halo appears above the cloud top or beneath the cloud base. The halo broadens with cloud age. The presence of wind shear can result in a non-symmetric humidity halo, broader downshear of the cloud than upshear of it. Due to the difficulty of choosing or following a particular cross-shear 2D slice of a moving cloud at each timestep, we have not studied cross-shear results in this paper.

## 2.5 Radiative effects of cloud halos

### 2.5.1 Net downward fluxes

To study the radiative impact of the humidity halo, we perform 3D radiative calculations using SHDOM. Because SHDOM is very efficient for a 2D medium, but computationally prohibitive when applied to a realistic 3D cloud field, we therefore decided to use a 2D ( $x-z$ ) slice of RAMS simulation data in the central domain for the radiation calculation, effectively assuming that the cloud is homogeneous in the  $y$ -direction. The radiation calculation is

performed at 4-min intervals. Fig. 2.11 displays the vertical profile of the temporally (over the cloud lifetime) and spatially (over the  $x$ -axis) averaged net downward radiative flux for all cases. The decrease of the net downward flux, averaged over the cloud column (as illustrated in Fig. 2.12), between the cloud top and the base, is a result of cloud extinction. However, the cloud-column averaging and the slant of sun's rays cause the flux to increase when approaching the surface. As illustrated in Fig. 2.12, by comparing the two levels,  $z_i$  and  $z_{i+1}$  where  $z_{i+1} > z_i$ , we see that a larger portion of the direct solar flux comes from the surrounding atmosphere, not attenuated by the cloud, at level  $z_i$  than at level  $z_{i+1}$ . Therefore, in Fig. 2.11 for the Barbados case where the solar zenith angle is close to zero, the flux does not increase from the cloud base to surface, while for the Hawaii case with a higher cloud base than the Oakland case, this increase of flux begins at a higher altitude than the latter case. The net downward flux averaged over the halo columns, rather than decreasing with increasing pressure as in the clear-sky, instead increases with increasing pressure in the presence of the cloud. The vertical profile of the net downward flux in the halo shows a trend opposite to that in the cloud from the surface up to above the cloud top. In the lower part of the halo region, the lower-lying of the peaks of the net downward flux is collocated with the minimum in the cloud region, and the multiple peaks are the results of cloud patches formed during the cloud dissipation. If there were no cloud, the water vapor absorption would decrease the net downward flux passing through the halo layer. Therefore, the results illustrate the influence of cloud scattering on radiative properties of the cloud-edge environment. The results also suggest that a 3D radiative transfer calculation, rather than a plane-parallel or independent pixel approximation that assumes no horizontal photon transport, is required for assessing radiative impacts of the humidity halo. This is because significant numbers of photons are scattered from the adjacent cloud into the lateral halo

region to enhance the net downward flux therein. The net downward flux averaged over the halo columns decreases below the cloud base because there is no enhancement through cloud scattering, leaving only the atmospheric gaseous absorption.

### 2.5.2 SW heating rate

From the radiative energy balance equation, it can be shown that the heating rate ( $H$ ) at an arbitrary point  $(x, y, z)$  can be related to the absorbed power per unit volume ( $F_a$ ) within the grid cell by

$$H = -\frac{1}{\rho c_p} \nabla \cdot \mathbf{F}(x, y, z) = \frac{1}{\rho c_p} F_a(x, y, z) \quad (2.7)$$

where  $\rho$  is air density,  $\mathbf{F}$  is the radiative flux vector, and  $c_p$  is specific heat of dry air. The net amount of photons accumulating in a grid cell can be estimated from the radiative heating rate, which is proportional to the divergence of the radiative flux by Eq. (7). The  $x$ - $z$  plot of the SW heating rate (Fig. 2.13, showing only the Hawaii case without wind) has a non-symmetric pattern with a minimum in the direction opposite to that of the incoming solar radiation. The minimum is due to the large extinction by the cloud along the incoming solar path with zenith angle  $\sim 10^\circ$ . The maximum heating rate can appear at both sides of the cloud for suitable combinations of the cloud shape, cloud depth and solar zenith angle, as in this case. Other cases also show the same pattern as in Fig. 2.13. Because the solar zenith angle for the Barbados case is very close to zero, the heating rate minimum in the halo region covers a negligible area.

To understand the enhanced absorption in the humidity halo relative to the far-ambient absorption, we perform the same type of averaging as in Fig. 2.11. The resulting profiles are shown in Fig. 2.14, displaying the time-averaged vertical profiles of the ambient and

halo heating rates (averaged over the humidity halo columns, schematized in Fig. 2.12) for all cases. For the Oakland and Hawaii cases, the halo heating rate is larger than the ambient heating rate except at the lowest levels. This is because of the minimum of the heating rate near the cloud base at the opposite side to the incoming solar radiation, as discussed above. There are two contributions to the increased halo heating (as illustrated in Fig. 2.2): (a) significant scattering of photons from the cloud edge, thus enhancing the net downward fluxes in the halo region as shown in Fig. 2.11; and (b) enhanced water vapor absorption by the halo itself. The maximum difference between the time-averaged in-halo and far-ambient heating rates, for the Oakland case without wind, is  $0.0058 \text{ K hr}^{-1}$  at 900 hPa. In other words, the enhanced heating rate in the halo at that level amounts to  $\sim 11\%$  of the far-ambient heating rate of  $0.052 \text{ K hr}^{-1}$ . The result for the sheared Oakland case (Fig. 2.14b) is similar to that for no wind (Fig. 2.14a); the maximum difference between the in-halo and far-ambient heating rates is  $0.0065 \text{ K hr}^{-1}$  at 950 hPa,  $\sim 12\%$  of the far-ambient heating rate of  $0.055 \text{ K hr}^{-1}$ . The enhanced halo heating rate occurs at higher levels for the Hawaii case (Fig. 2.14c, d) than for the Oakland case, because of a higher cloud base. The maximum difference between the two heating rates for the Hawaii case without wind (Fig. 2.14c) is  $0.019 \text{ K hr}^{-1}$  at 788 hPa,  $\sim 16\%$  of the far-ambient heating rate  $0.12 \text{ K hr}^{-1}$ . In the sheared Hawaii case (Fig. 2.14d), the larger and more significant humidity halo and the many small cloud patches lead to larger halo absorption; the maximum enhancement of the heating rate in the humidity halo, relative to the far-ambient region, is  $0.022 \text{ K hr}^{-1}$  at 831 hPa,  $\sim 18\%$  of the clear-sky heating rate of  $0.12 \text{ K hr}^{-1}$ . The Barbados case (Fig. 2.14e) exhibits a more uniform enhancement of the halo heating below 850 hPa than the other cases, because the solar zenith angle is close to zero. The maximum value of the time-averaged halo heating rate enhancement is  $0.013 \text{ K hr}^{-1}$  at 955 hPa,  $\sim 11\%$  of the

ambient heating rate of  $0.12 \text{ K hr}^{-1}$ .

In short, several factors can affect the humidity halo absorption including the cloud shape, cloud depth, 3D halo distribution and solar zenith angle. Factors other than the solar zenith angle, cannot be simply determined before a simulation, making the the humidity halo absorption a complex issue.

### 2.5.3 Change of SW heating rate due to the halo

One approach to assessing the radiative effect of the humidity halo region is to compare SW radiative heating rates in the presence and absence of the halo. The presence-of-halo scenario is chosen as the output from the RAMS model, and the absence-of-halo scenario is defined by replacing the water vapor field of the shaded regions in Figs. 2.4, 2.5, 2.7, 2.8 and 2.10 with the far-ambient values at the corresponding heights. Fig. 2.15 shows the vertical profiles of this heating rate difference, temporally and spatially averaged, for each cloud considered. For the Oakland case without wind (Fig. 2.15a), the halo has a radiative effect between 890 and 990 hPa with large positive values below 960 hPa, with the humidity halo being evident mainly at lower levels. However, for the Oakland case with wind shear (Fig. 2.15b), the radiative effect is pronounced between 900 and 990 hPa, because the halo is more vertically extensive. The difference between the heating rates is negative below the halo area, as a result of absorption in the halo above. The Hawaii case without wind (Fig. 2.15c) shows two regions of significant positive time-averaged heating rate differences. The halo radiative effect is stronger at the lower levels than at the upper levels, consistent with the halo being correspondingly more persistent and broader at the lower levels. Another key point from this figure is that the halo radiative effect in the absence of wind is larger for the Hawaii case than for the Oakland case, as we can anticipate that

stronger convection causes a broader and more humidified halo. In a sheared environment (Fig. 2.15d), the halo is both deeper and broader, especially during cloud dissipation, and the halo radiative effect is more significant than in the absence of wind (Fig. 2.15c). For the Barbados trade wind cumulus, the difference of heating rates (Fig. 2.15e) displays layers of positive values through 960-930 hPa and 870-800 hPa. The lower region of positive halo heating rate differences results from a thin layer of halo at cloud base, whereas the humidity halo formed by the dissipation of upper portions of the cloud results in a large radiative effect at these upper levels. All of the case studies illustrate that the vertical distribution of the halo radiative effect is directly related to the vertical distribution of the halo. The Hawaii case in a sheared environment exhibits the largest time-averaged effect. Strong convection in a sheared environment, therefore, is a key factor in producing relatively broad and vertically extensive cloud halos with concomitant strong radiative effects.

#### 2.5.4 Halo radiative forcing at the surface of the earth

We further calculate the halo-induced radiative forcing at the surface of the simulated domain. Halo-induced radiative forcing is defined by the difference between the radiative fluxes in the presence-of-halo scenario and in the absence-of-halo scenario. The boundary condition of the radiative transfer model is such that horizontal radiative transport of the domain is zero. Therefore, the radiative forcing can be estimated from only the net downward flux at the surface. The temporally and spatially averaged halo SW surface radiative forcing for all cases, given in Table 2.2, shows all negative values, indicating that the presence of the halo can reduce the SW energy at the surface. The results also clearly demonstrate that this forcing is larger with wind shear than for no wind. The strongest forcing, for the Hawaii case with wind shear, is  $-0.19 \text{ W m}^{-2}$ , which is approximately 0.02%

change compared to no halo. The halo radiative effect is generally small when the cloud starts to form, and becomes larger with time. Therefore, the results of the halo surface forcing are consistent with the conclusions in previous sections.

## 2.6 Summary

From our simulations of several cumulus cloud scenarios, we can conclude that the spatial distribution of cloud halos has the following common characteristics: (1) The humidity halo occurs primarily near the lateral cloud boundaries, as verified by many observations. When the upper (lower) portion of a cloud dissipates, it leaves behind a humidified area; (2) the humidity halo is broader in the presence of wind shear than in the absence of wind, and broadens with cloud age; (3) the humidity halo is broader near the downshear cloud boundary than near the upshear side, owing to cumulus cloud dynamics that favor growth on the upshear side and decay on the downshear side. Evaporation of cloud droplets on the downshear side humidifies the clear air there. However, the growth of new cumulus turrets limits the clear-air humidity modification on the upshear side.

The halo can absorb both incoming solar energy from the clear sky above and scattered SW radiation from the cloud, and hence increases the total absorption in the domain. The SW (0.2–4.0  $\mu\text{m}$ ) radiative heating rate in the halo is 11 to 18% larger than the ambient environmental heating rate. The strongest halo-induced surface SW radiative forcing, temporally and spatially averaged, among all cases studied is about  $-0.19 \text{ W m}^{-2}$ , a 0.02% change compared to no halo. The radiative effect of the halo is closely related to the cloud evolution. It is largest at cloud dissipation when the halo expands, as shown by the calculated net downward flux, heating rate and surface radiative forcing.

Increased absorption due to the humidity halo depends on the amount of water vapor,

cloud morphology, solar zenith angle, spatial halo distribution, incoming solar energy, cloud age and the interaction of the environmental wind with the cloud evolution.

## 2.7 Acknowledgment

We thank Prof. Frank Evans at the University of Colorado for providing and helping with the SHDOM model. Constructive reviews from anonymous reviewers helped in the presentation of this paper. This work was supported by National Science Foundation Grant ATM-9907010.

Table 2.1: Summary of case studies.

Location <sup>a</sup>	Wind condition	Cloud lifetime (min)	Cloud formation time (min)	Cloud mature time <sup>b</sup> (min)	Maximum cloud depth <sup>c</sup> (km)	Maximum cloud LWC <sup>c</sup> (g m <sup>-3</sup> )	Maximum in-cloud updraft velocity <sup>c</sup> (m s <sup>-1</sup> )	Solar zenith angle (degree)
Oakland, CA	No	28	0	14-18	0.9	1.58	3.8	51.2
Oakland, CA	Wind shear	26	0	12-16	0.7	1.24	2.9	51.2
Kauai, HI	No	44	10	18-30	2.7	3.11	15.2	10.6
Kauai, HI	Wind shear	36	10	18-20	1.7	2.49	9.3	10.6
Barbados	Wind shear	36	14	24-26	1.4	2.45	8.1	3.6

<sup>a</sup> based on the maximum cloud LWC and maximum in-cloud vertical velocity.

<sup>b</sup> see section 3 for details of the location for each case.

<sup>c</sup> peak value for the entire simulation and domain.

Table 2.2: Temporally and spatially averaged halo SW radiative forcing at the surface of the earth.

Location <sup>+</sup>	Wind Condition	Halo Radiative Forcing ( $\text{W m}^{-2}$ )
Oakland, CA	No	-0.001
Oakland, CA	Wind shear	-0.023
Kauai, HI	No	-0.067
Kauai, HI	Wind shear	-0.190
Barbados	Wind shear	-0.085

<sup>+</sup> See section 3 for details of the locations for each case.

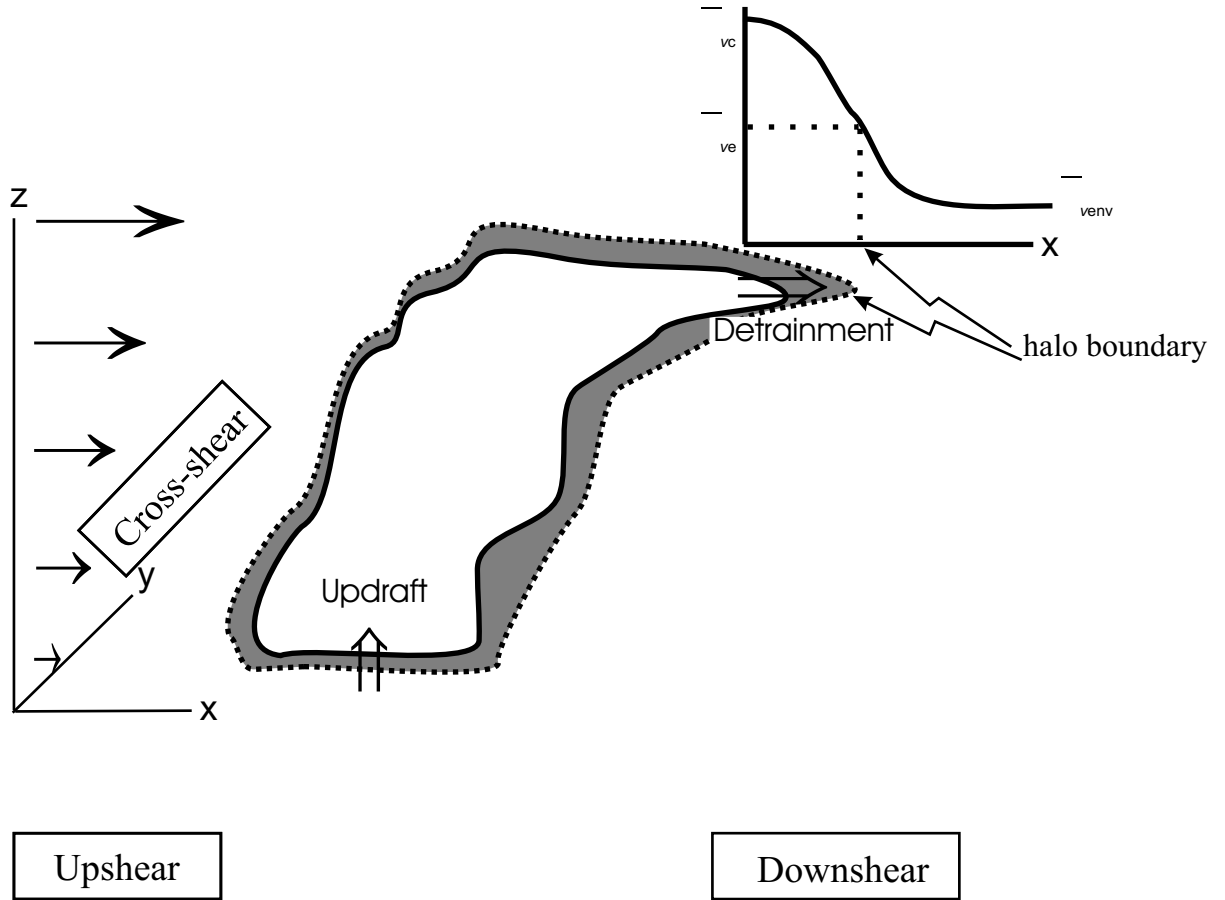


Figure 2.1: Schematic of cloud halo (shaded region). This depiction shows a westerly wind increasing with height. Upshear and downshear are defined relative to the vertical wind shear. In the upper right corner, average absolute humidity is sketched as a function of the distance from the cloud edge.  $\bar{\rho}_{vc}(z)$  is the mean absolute humidity of the cloud. When the absolute humidity approaches a constant value, it is defined as  $\bar{\rho}_{venv}(z)$ .  $\bar{\rho}_{ve}(z)$  is the  $e$ -folding absolute humidity calculated by Eq. (2.3). If there is cloud at an arbitrary height  $z$ , the cloud halo is defined by that region of the humidity field where  $\bar{\rho}_{vc}(z) > \rho(z) > \bar{\rho}_{ve}(z)$ . If there is no cloud at that altitude, the halo is defined by Eq. (2.4).

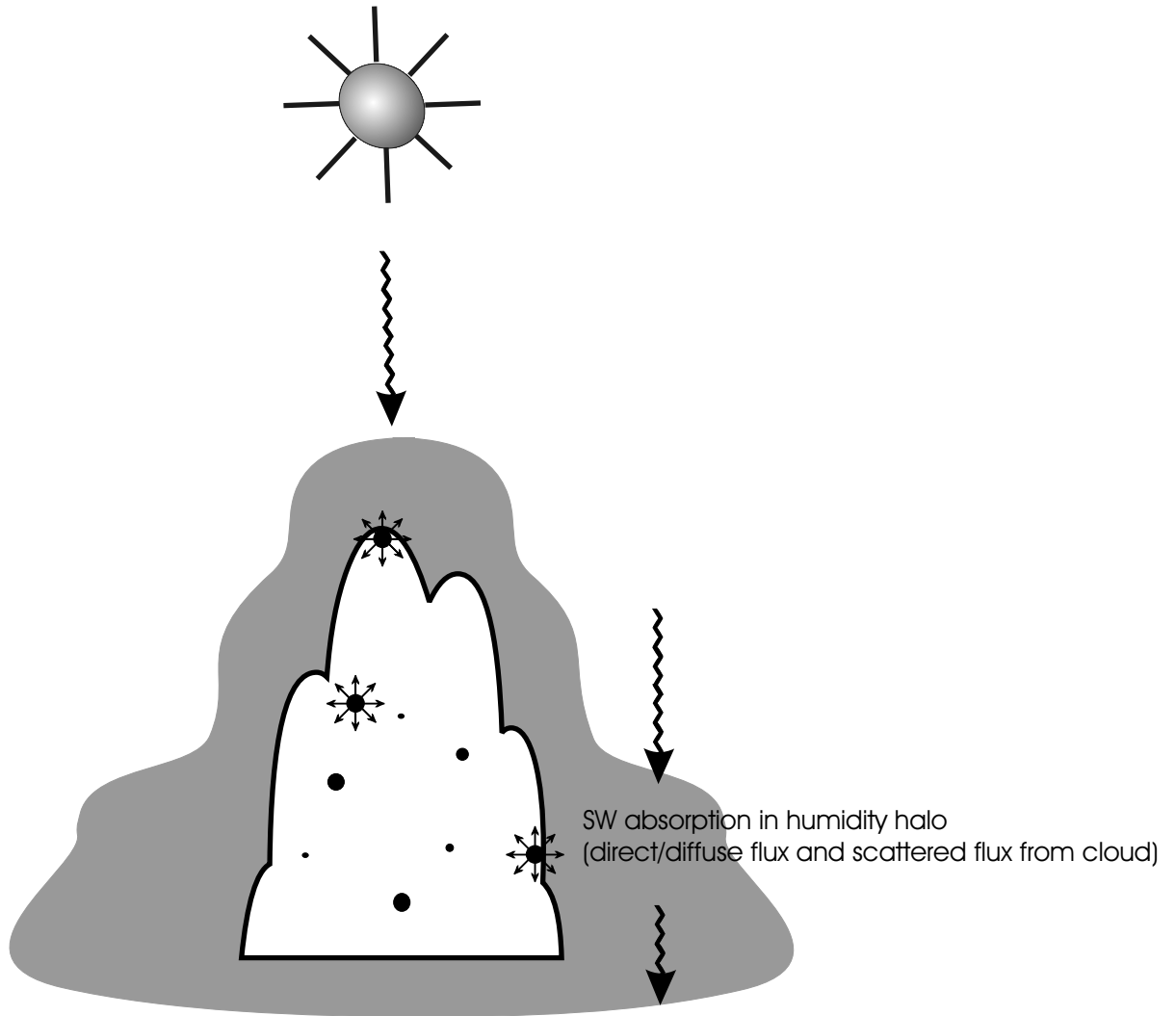


Figure 2.2: Schematic of radiative transfer in the cloud halo for a cumulus cloud. The cloud halo absorbs incident solar radiation directly, as well as the scattered radiation from nearby cloud droplets.

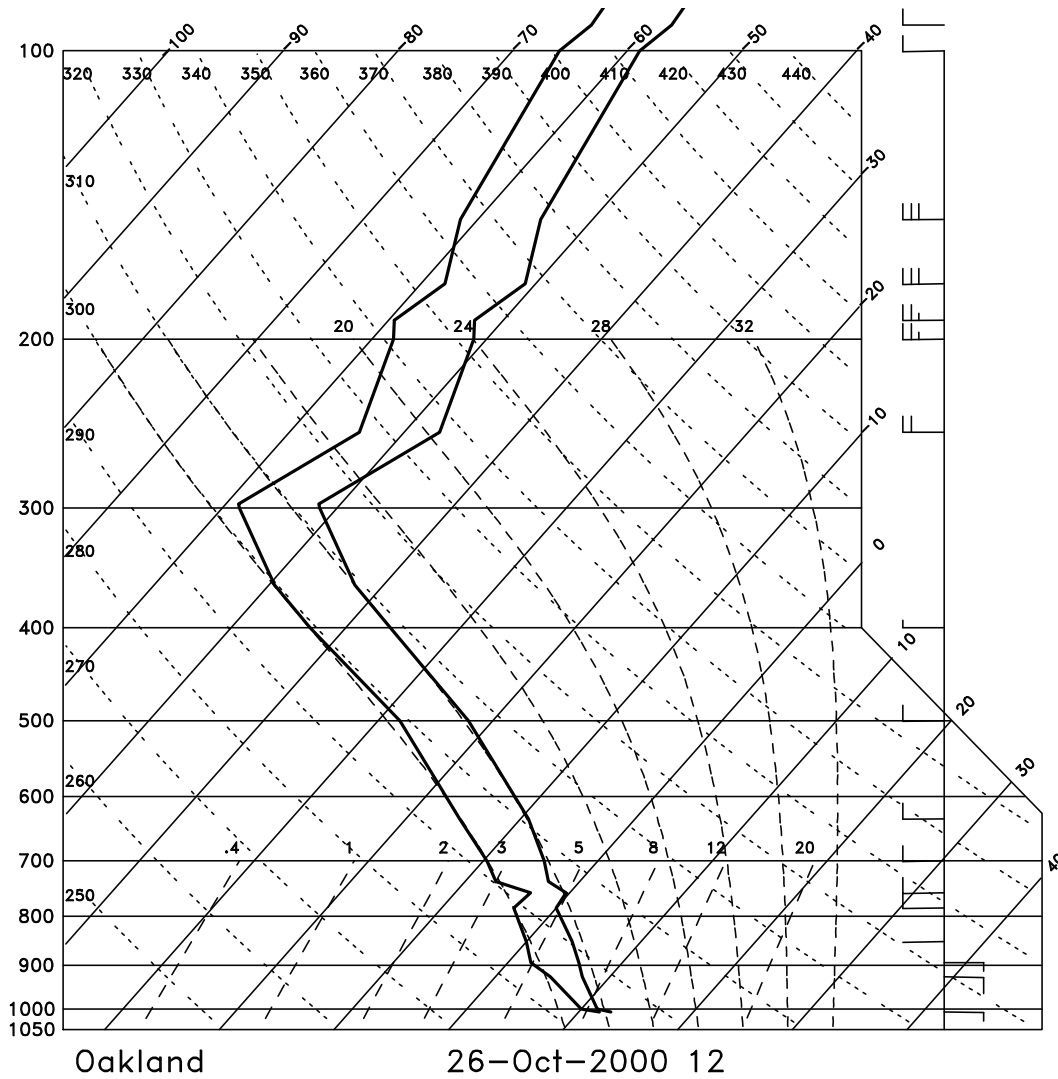


Figure 2.3: Skew T-log  $p$  diagram of environmental conditions for a typical shallow cumulus off the northern California coastline. Temperature and dew point temperature profiles are represented by thick lines. The skewed abscissa is temperature ( $^{\circ}\text{C}$ ) and the ordinate is pressure (hPa). Dotted lines labeled in Kelvins represent dry adiabats while curved, dashed lines labeled in  $^{\circ}\text{C}$  are pseudoadiabats. Straight-dashed lines labeled in  $\text{g kg}^{-1}$  are isopleths of the saturation water vapor mixing ratio. This vertical sounding profile was obtained in Oakland, CA ( $37^{\circ}44'\text{N}$ ,  $122^{\circ}13'\text{W}$ ) at 1200 GMT, 26 October 2000. The north-south wind is arbitrarily set to zero. The sounding profile features an increasing easterly wind with height below 925 hPa.

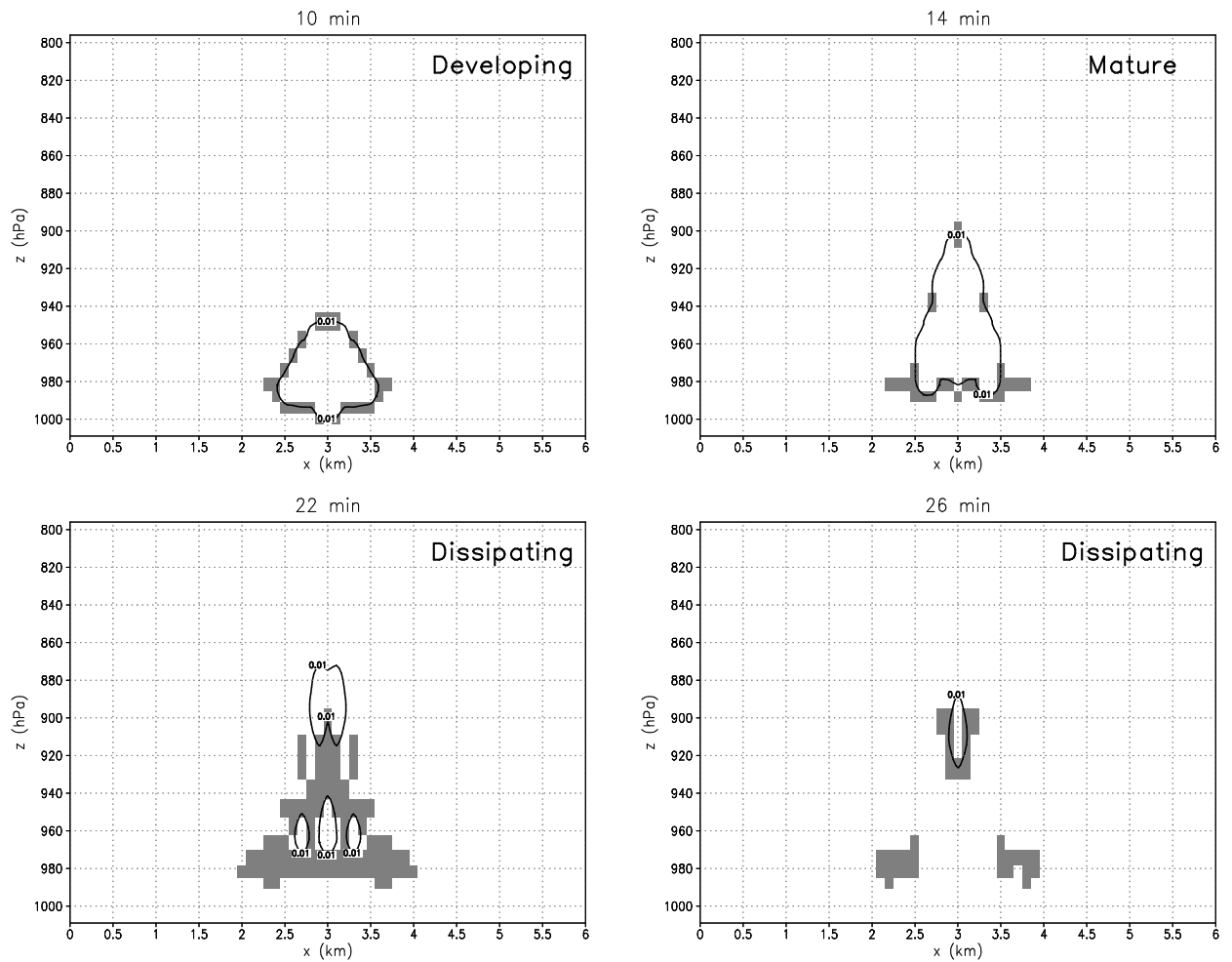


Figure 2.4: Simulated development of shallow cumulus off the northern California coast near Oakland in the absence of wind, for several selected time stages. The contour represents a cloud liquid water content (LWC) of  $0.01 \text{ g m}^{-3}$ , chosen to define the cloud boundary. The shaded region outside the cloud boundary, defined to be the cloud halo, is where the absolute humidity exceeds the  $e$ -folding water vapor density (see Fig. 2.1).

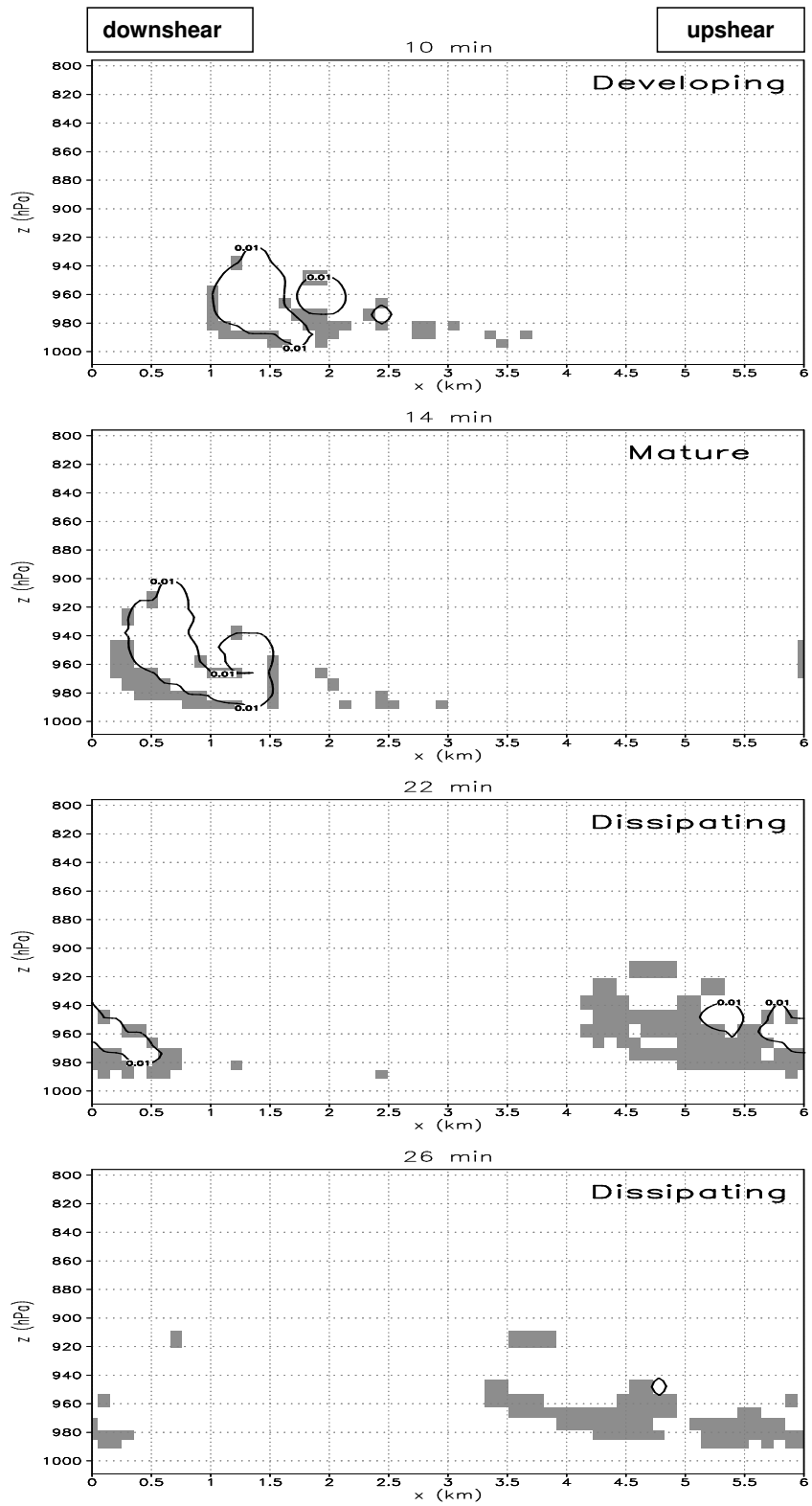


Figure 2.5: Same as Fig. 2.4 but in the presence of the wind shear shown in Fig. 2.3.

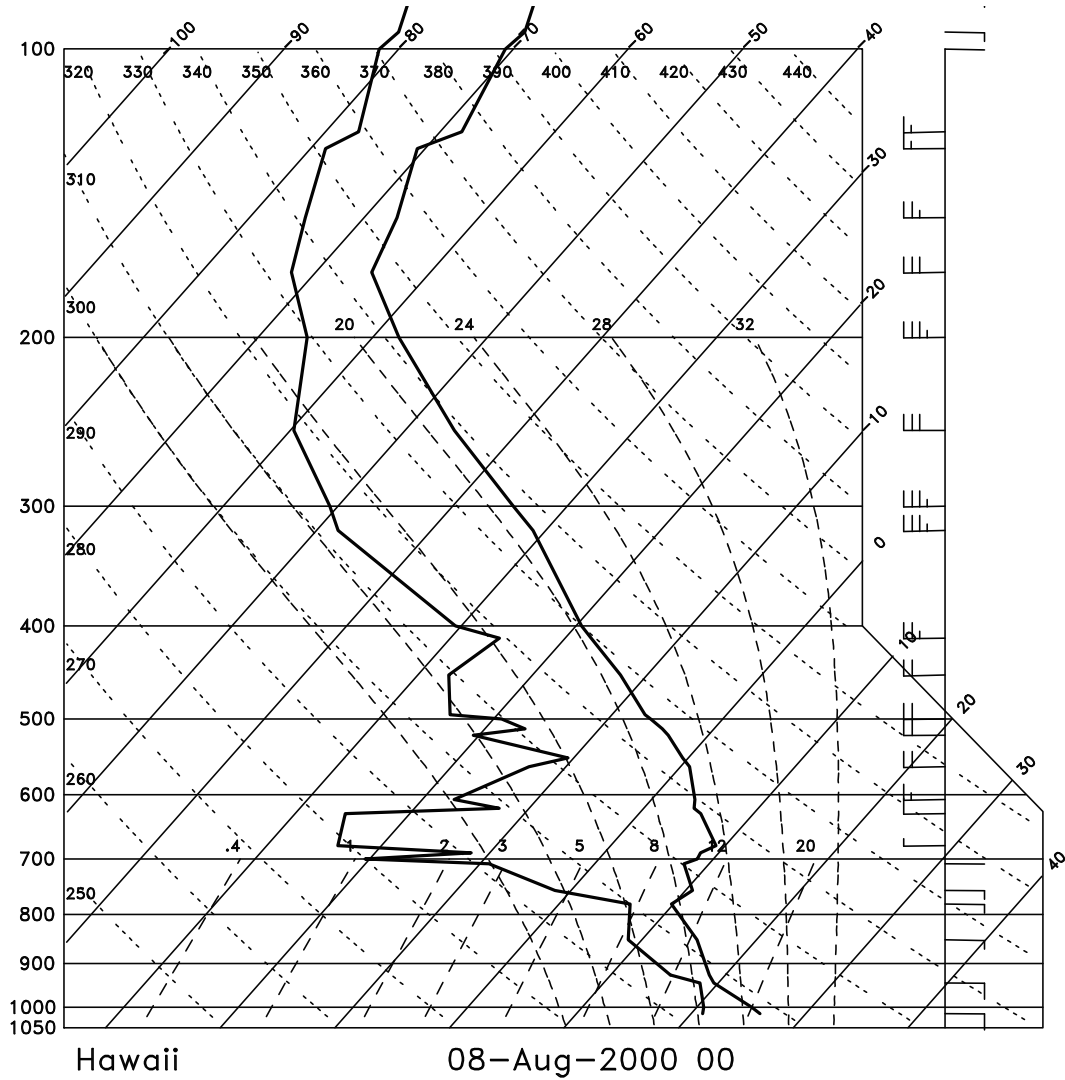


Figure 2.6: Skew T-log  $p$  diagram of environmental conditions for a typical cumulus near Hawaii. The description of the lines and ordinates is as in Fig. 2.3. This vertical sounding profile was observed at Lihue on Kauai, Hawaii ( $21^{\circ}59'N$ ,  $159^{\circ}21'W$ ) at 0000 GMT, 8 August 2000. The north-south wind is arbitrarily set to zero. The sounding profile features a decreasing easterly wind with height up to 700 hPa, overlain by an increasing westerly wind with height in the cloud layer.

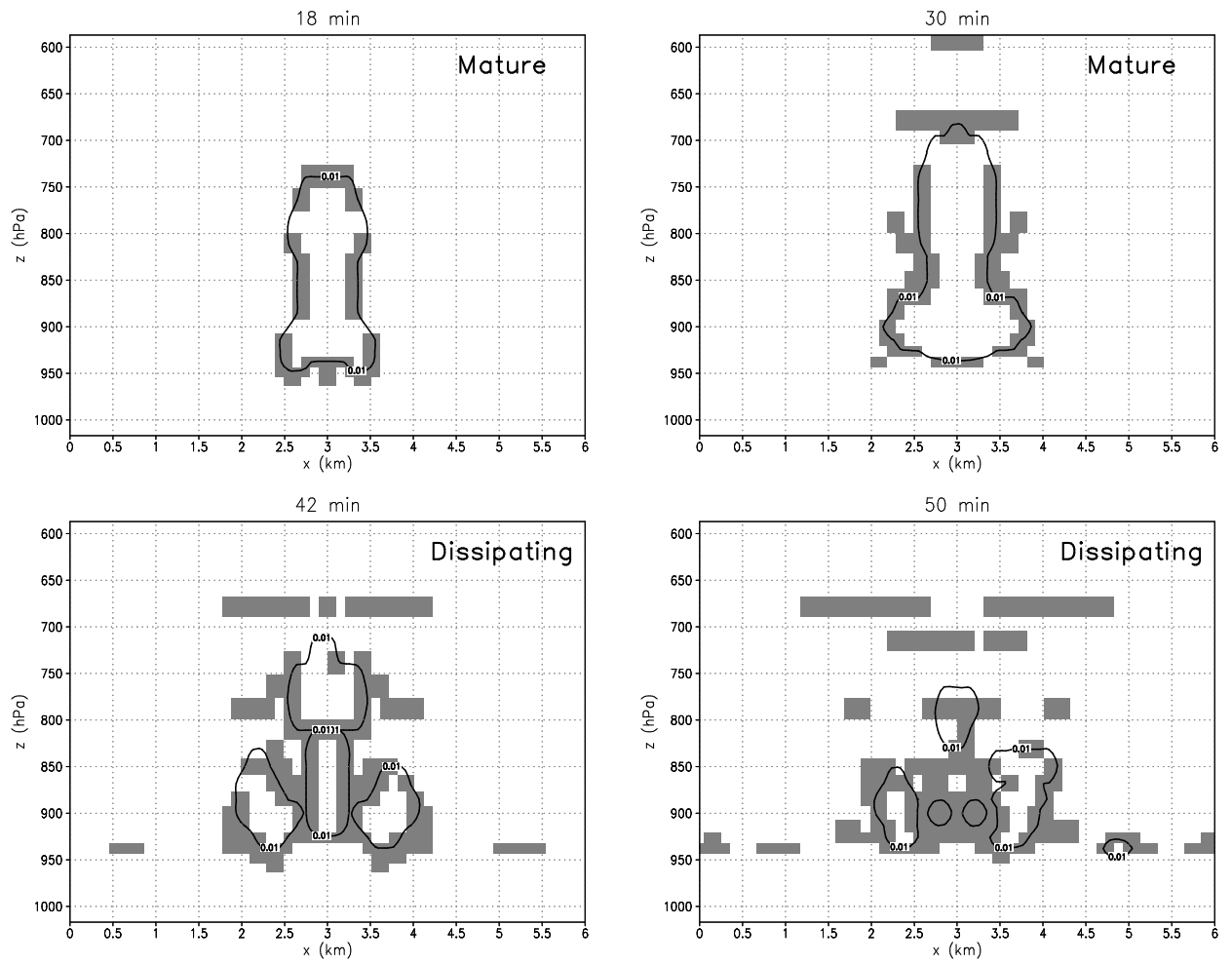


Figure 2.7: Same as Fig. 2.4, but for cumulus cloud near Hawaii in the absence of wind.

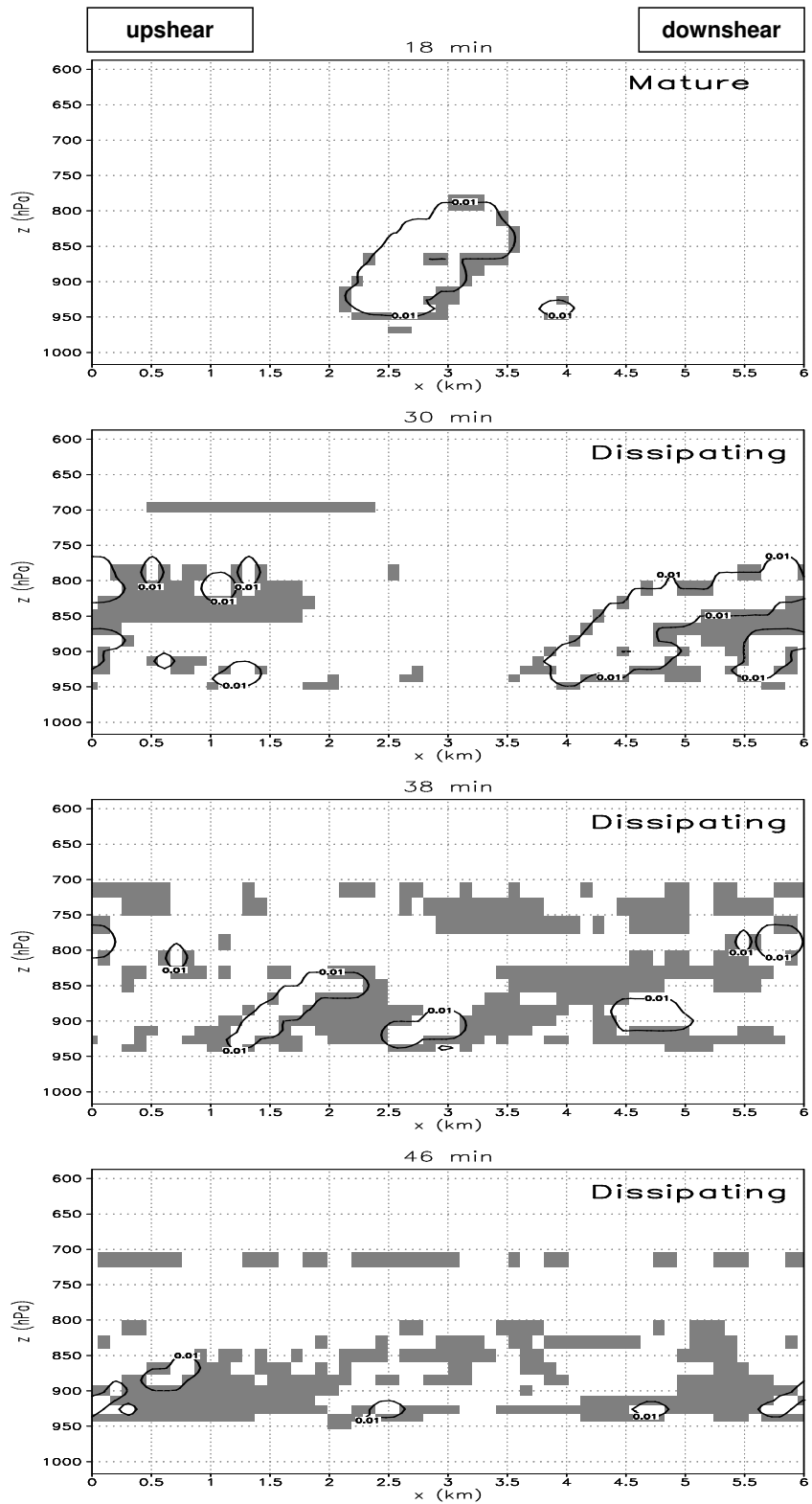


Figure 2.8: Same as Fig. 2.7 but in the presence of the wind shear shown in Fig. 2.6.

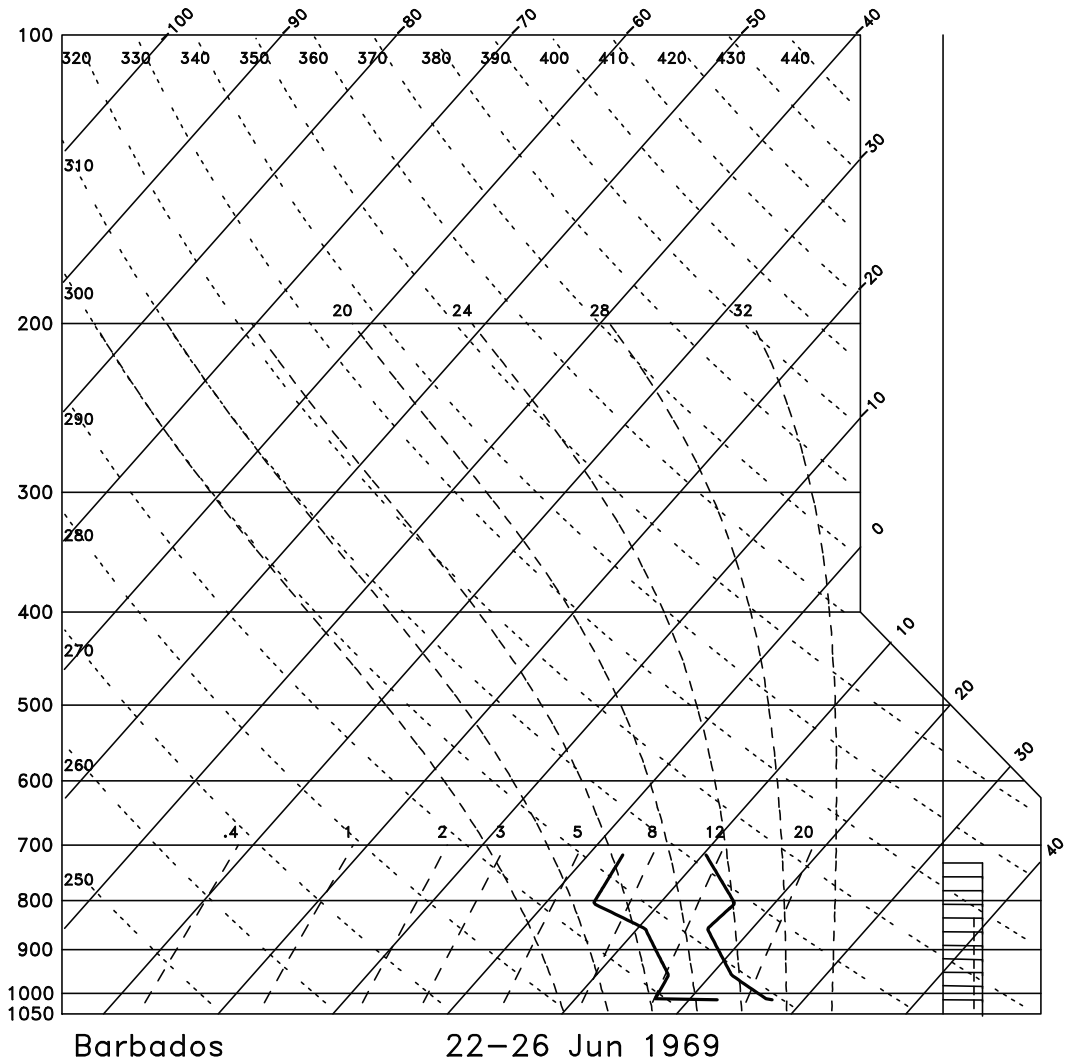


Figure 2.9: Skew T-log  $p$  diagram of environmental conditions for a Barbados trade-wind cumulus cloud (data taken from <http://www.knmi.nl/~siebesma/gcss/bomexcomp.append.html>). The description of the lines and ordinates is as in Fig. 2.3. The simulation date is set to 4 August 2000.

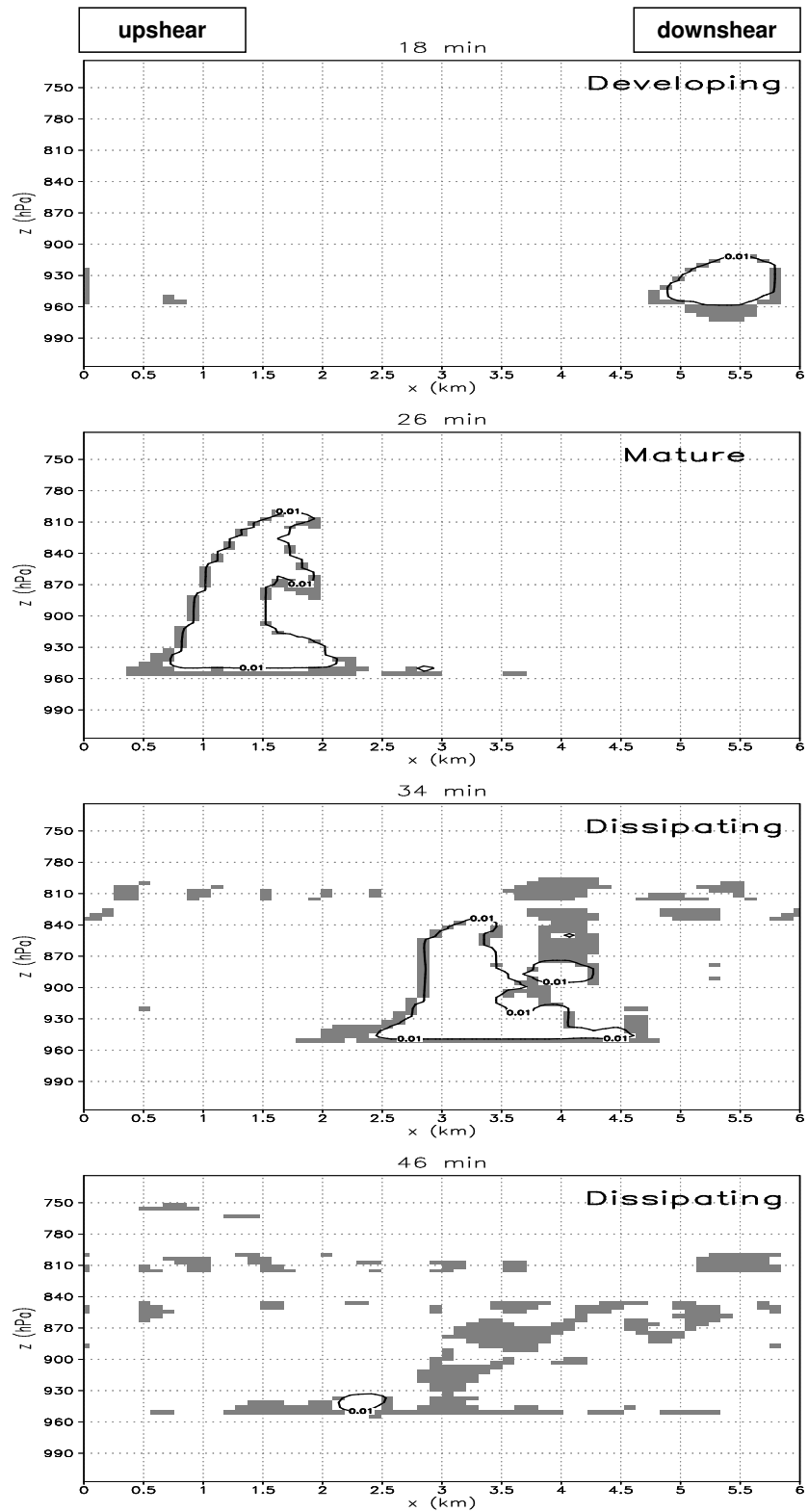


Figure 2.10: Same as Fig. 2.4. but for Barbados trade wind cumulus.

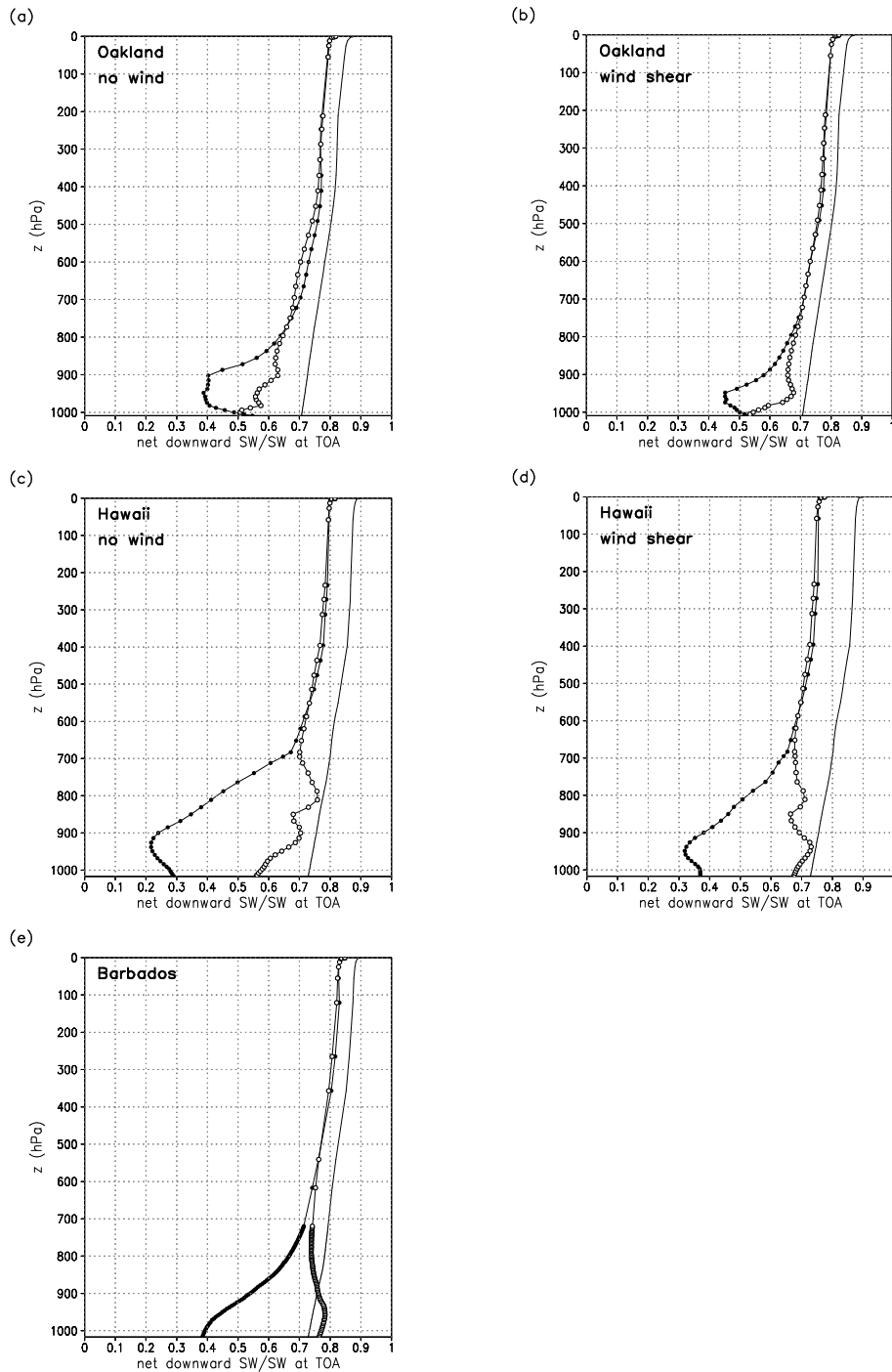


Figure 2.11: Vertical profile of the temporally and spatially averaged net downward SW flux normalized to the incoming SW at the TOA (top of the atmosphere) for the cloud of (a) Oakland case without wind (Fig. 2.4), (b) Oakland case with wind shear (Fig. 2.5), (c) Hawaii case without wind (Fig. 2.7), (d) Hawaii case with wind shear (Fig. 2.8), (e) Barbados case (Fig. 2.10): cloud (closed circle), halo (open circle), and far-ambient (solid line only). The area average is illustrated in Fig. 2.12

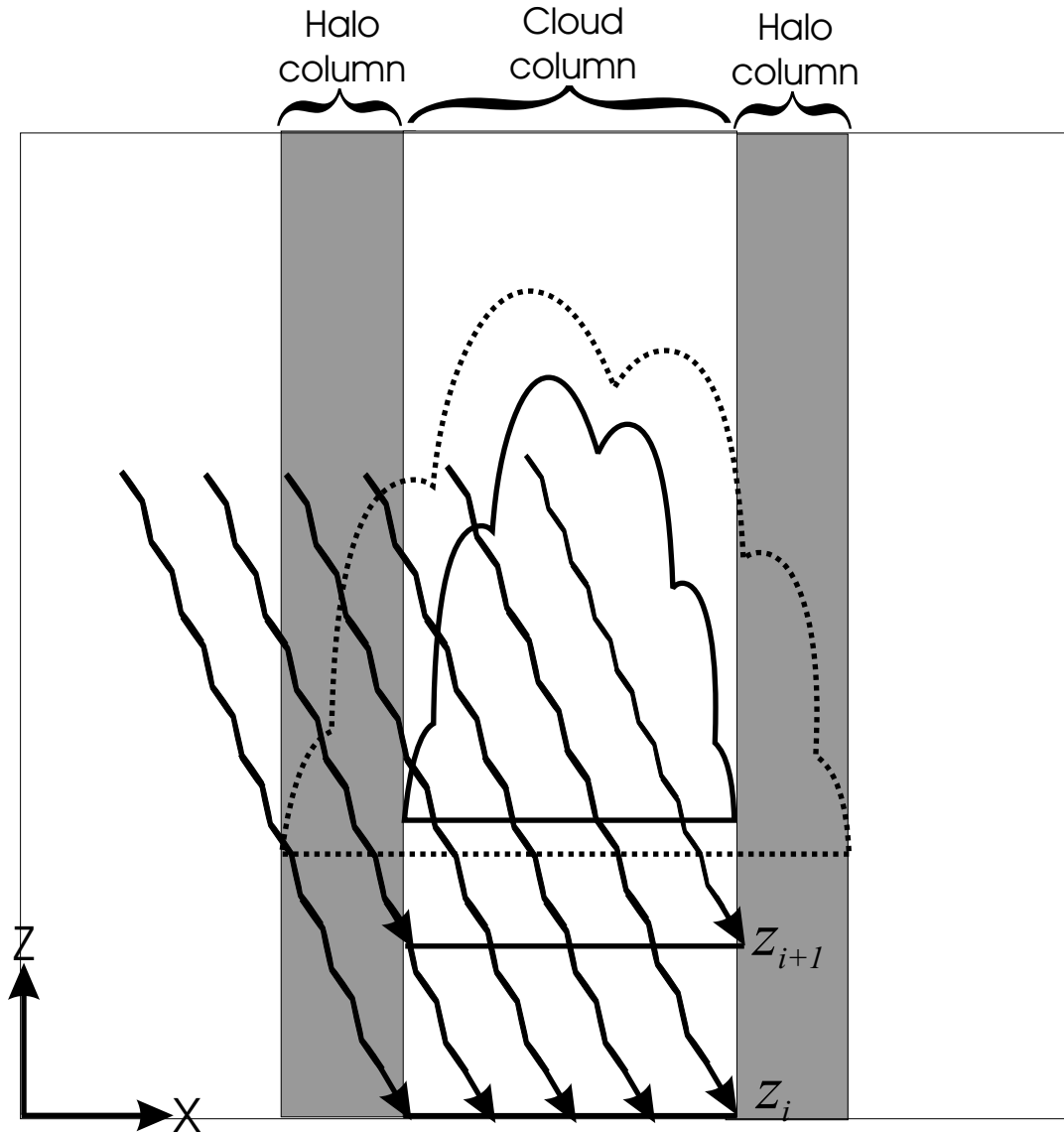


Figure 2.12: Illustration of the increased net downward flux below cloud base (see text for details). The shaded columns are halo columns, and between them is the cloud column. The solid line is the cloud, and the region between the dotted line and the cloud defines the cloud halo. The two bold horizontal lines represent levels  $z_i$  and  $z_{i+1}$  with  $z_{i+1} > z_i$ .

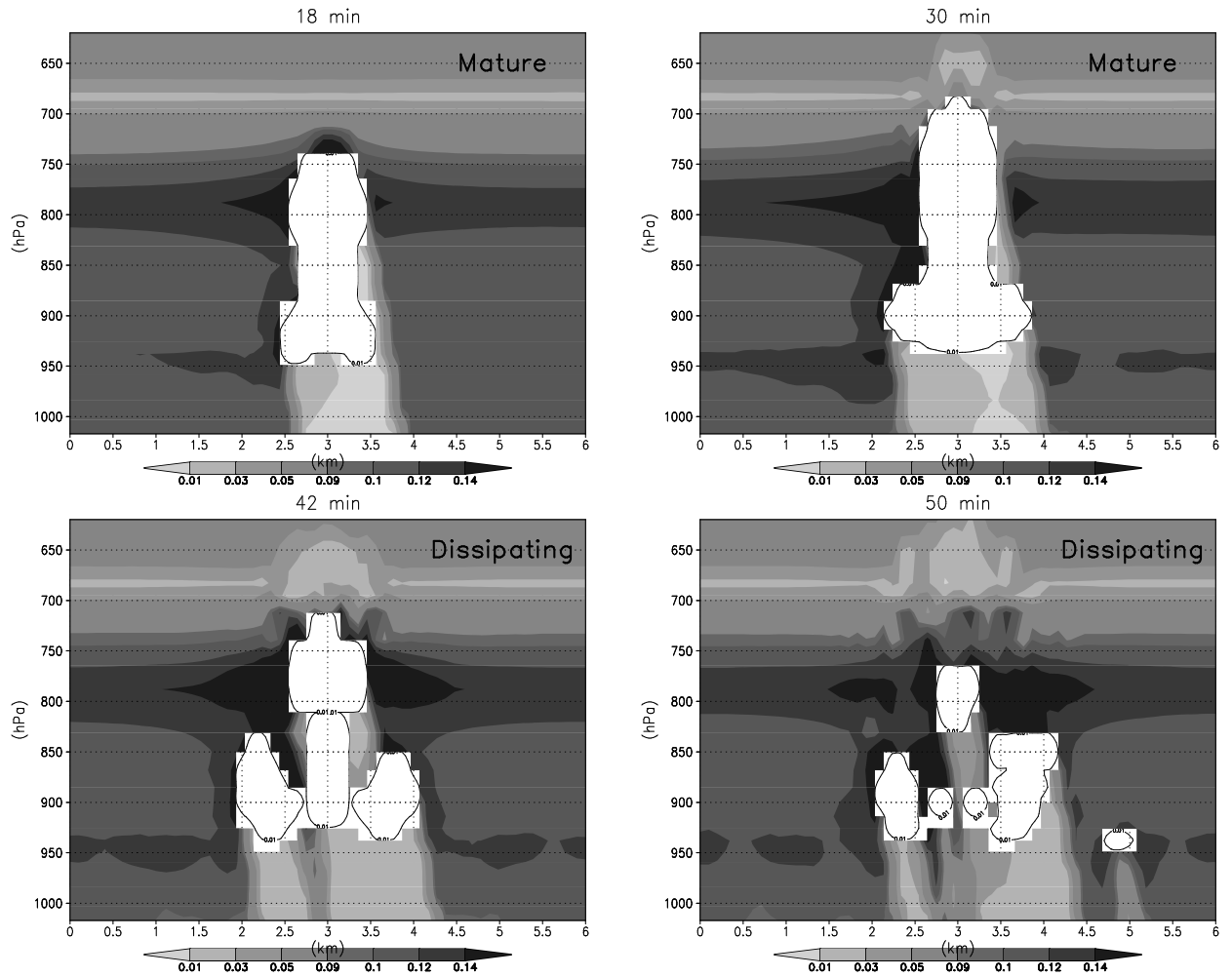


Figure 2.13: SW heating rate (K hr<sup>-1</sup>) for the small cumulus of Fig. 2.7. In-cloud values are not shown in order to show details in the halo region. Cloud boundaries are defined by the 0.01 g m<sup>-3</sup> contour line for the cloud LWC.

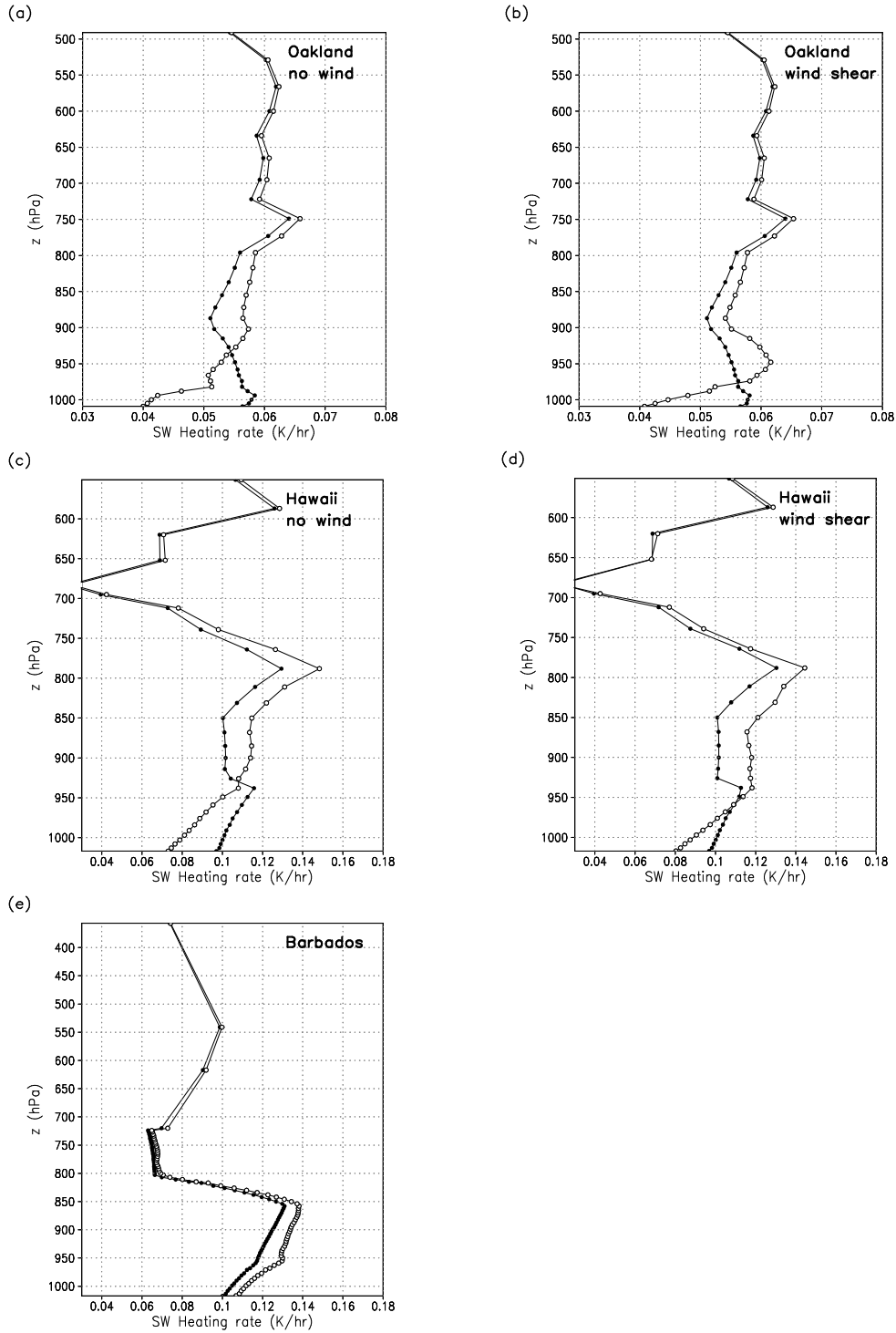


Figure 2.14: Vertical profile of the temporally and spatially averaged SW heating rate for the cloud of (a) Oakland case without wind (Fig. 2.4), (b) Oakland case with wind shear (Fig. 2.5), (c) Hawaii case without wind (Fig. 2.7), (d) Hawaii case with wind shear (Fig. 2.8), (e) Barbados case (Fig. 2.10): halo (open circle) and far-ambient (closed circle).

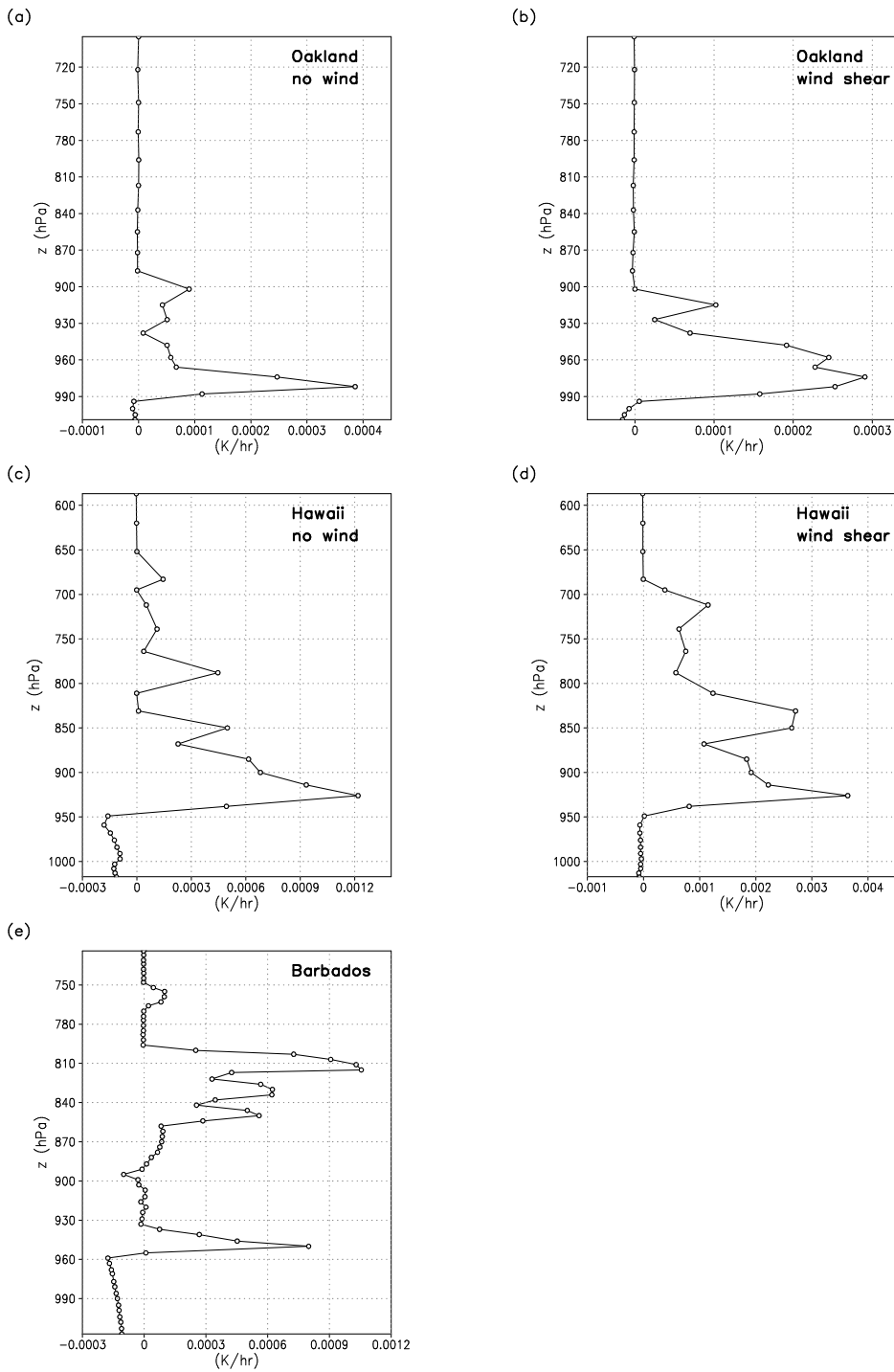


Figure 2.15: The radiative effect of the cloud halo, computed by subtracting the domain-averaged heating rate in the presence of the halo from that in the absence of the halo, for (a) Oakland case without wind, (b) Oakland case with wind shear, (c) Hawaii case without wind, (d) Hawaii case with wind shear, (e) Barbados case. These heating rate profiles are temporally averaged over the cloud lifetime and spatially averaged over the horizontal domain.

## Chapter 3

# Analysis of humidity halos around trade wind cumulus clouds

Reference: Lu, M.-L., J. Wang, A. Freedman, H. H. Jonsson, R. C. Flagan, R. A. McClatchey, and J. H. Seinfeld, 2003: Analysis of Humidity Halos Around Trade Wind Cumulus Clouds. *J. Atmos. Sci.*, **60**, 1041–1059.

### 3.1 Abstract

Regions of enhanced humidity in the vicinity of cumulus clouds, so-called cloud halos, reflect features of cloud evolution, exert radiative effects, and may serve as a locus for new particle formation. We report here the results of an aircraft sampling campaign carried out near Oahu, Hawaii from July 31 through August 10, 2001, aimed at characterizing the properties of trade wind cumulus cloud halos. An Aerodyne Research Inc. fast spectroscopic water vapor sensor, flown for the first time in this campaign, allowed characterization of humidity properties at 10-m spatial resolution. Statistical properties of 60 traverses through cloud halos over the campaign were in general agreement with measurements reported by Perry and Hobbs (1996). One particularly long-lived cloud is analyzed in detail, through both airborne measurement and numerical simulation to track evolution of the cloud halos

over the cloud's lifetime. Results of both observation and the simulation show that cloud halos tend to be broad at lower levels and narrow at upper levels and broader on the downshear side than on the upshear side, broadening with time particularly in the downshear direction. The high correlation of clear-air turbulence distribution with the halo distribution temporally and spatially suggests that the halo forms, in part, due to turbulent mixing at the cloud boundary. Radiative calculations carried out on the simulated cloud and halo field indicate that the halo radiative effect is largest near cloud top during mature and dissipation stages. The halo-enhanced atmospheric shortwave absorption, averaged over this period, is about 1.3% of total solar absorption in the column.

## 3.2 Introduction

Cloud halos, which are regions of enhanced humidity in the vicinity of isolated cumulus clouds, are intimately associated with atmospheric dynamics, as they reflect features of cloud formation and dissipation, and might also serve as the predominant region of cloud-associated new particle formation. Moreover, halos exert radiative effects, in addition to those of the clouds themselves, which have an impact on the energy balance of the atmosphere. Halos have been identified in aircraft studies (Malkus 1949; Ackerman 1958; Telford and Wagner 1980; Radke and Hobbs 1991; Hobbs and Radke 1992; Perry and Hobbs 1996), ground-based measurements (Platt and Gambling 1971; Kollias et al. 2001), modeling studies of detrainment (Raymond and Blyth 1986; Bretherton and Smolarkiewicz 1989; Raga et al. 1990; Taylor and Baker 1991), and numerical simulations (Lu et al. 2002). Such regions have been also reported associated with frontal clouds (Weber et al. 2001) and mountain thunderstorms (Raymond et al. 1991). Summaries of these airborne and ground-based measurements of cloud halos are given in Table 3.1.

From aircraft measurements of 31 small to medium sized, isolated marine cumulus clouds off the coast of Washington and Oregon, Perry and Hobbs (1996) identified three factors dominant in determining the existence and extent of halos — cloud age, wind shear, and presence of a stable atmospheric layer. The halo region was found to broaden with increasing cloud age, with the region being most significant in the downshear direction from the cloud (see section 3.4.1 for definition of upshear and downshear).

Lu et al. (2002) utilized the three-dimensional (3D) RAMS (Regional Atmospheric Modeling System) model to simulate the spatial and temporal development of cloud halos for isolated, small to medium sized cumulus both in the presence and absence of wind shear. The simulated temporal and spatial patterns were in reasonable quantitative agreement with reported observations. They further calculated the radiative effect of the humidity halo using a 3D radiative transfer model. Through case studies, Lu et al. (2002) found that halos exert their greatest radiative effect for more convective clouds with vertical wind shear in the dissipation stage of cloud lifetime.

A number of investigators (e.g., Weber et al. 2001; Clarke and Kapustin 2002) have reported new particle formation in the vicinity of clouds. Kerminen and Wexler (1994) showed that atmospheric nucleation is most favored when there is a rapid transition from moderate to high humidity. Perry and Hobbs (1994) observed elevated ambient CN (Condensation Nuclei) levels associated with conditions of high humidity, low total aerosol surface area, low temperature, high SO<sub>2</sub>, and enhanced actinic flux. Their observations indicate that clear air above cloud top and downwind of the cloud in the outflow anvil are possible loci for new particle formation.

We report here on an aircraft sampling campaign, termed Cloud Halo, conducted between July 31 and August 10, 2001 in the vicinity of Oahu, Hawaii, a campaign that had as

its goal measurements and analysis of humidity distributions around trade wind cumulus clouds. The measurements from this campaign add to the existing body of information on cloud halos, their frequency of occurrence, spatial extent, and meteorological characteristics. These data will aid in assessing the shortwave (SW) radiative impact of halo regions and the extent to which halo regions are of importance in the SW energy balance of the atmosphere. Radiative flux measurements in the vicinity of cloud edges are difficult to interpret. When numerical simulation of cloud development can be demonstrated to agree qualitatively with observations, then numerically simulated halo fields can be used as a basis to assess radiative impacts.

In section 3.3 the sampling campaign and the airborne instruments employed are described. We then select for detailed analysis one cloud sampled during the campaign for which an extraordinary degree of observation was achieved (section 3.4). A numerical simulation of the development of that particular cloud is presented in section 3.5. In section 3.6, we simulate the radiative properties of halos and the extent to which halos influence overall atmospheric SW absorption.

### **3.3 Cloud Halo field experiment and instrumentation**

In the Cloud Halo campaign, the Center for Interdisciplinary Remotely-Piloted Aircraft Studies (CIRPAS) Twin Otter aircraft flew nine missions out of the Marine Corps Base Hawaii at Kaneohe, Oahu, Hawaii ( $21.44^{\circ}\text{N}$ ,  $157.77^{\circ}\text{W}$ ) from 31 July through 10 August 2001. Ambient conditions northeast of Kaneohe Bay, Hawaii are typical of those giving rise to trade wind cumulus (Austin et al. 1996). Forty-four isolated cumulus clouds were sampled over the nine missions. The Twin Otter aircraft executed a similar flight pattern for each cloud, sampling at a near constant aircraft velocity of  $50\text{ m s}^{-1}$ , starting over the

cloud top, followed by horizontal traverses through the cloud at ever decreasing altitudes, ending with a traverse just below the cloud. The horizontal passes through a given cloud, chosen to be in the upwind and downwind directions, commenced at least 3 km from the visible cloud boundary. Ambient soundings in clear air were usually taken each day at the beginning and the end of the mission.

The meteorological instrument package on the Twin Otter consisted of a Rosemount E102AL total temperature probe, Setra 270 static pressure transducer, and Setra 239 differential pressure transducers for measurements of dynamic pressure, side slip, and angle of attack. The Rosemount total temperature probe uses a sensing element in the airstream to measure the temperature. The accuracy of this instrument has been reported in Lawson and Cooper (1990) to be  $0.3\text{ }^{\circ}\text{C}$  in clear sky and  $-1\text{ }^{\circ}\text{C}$  at a liquid water content (LWC) of  $2\text{ g m}^{-3}$ . A NovAtel Propack GPS system reported location as well as ground speed, track, and vertical speed. The Trimble TANS (Trimble Advanced Navigation System) Vector provided the aircraft attitude in addition to a redundant measurement of location. Humidity measurements were carried out by a new high-speed (10 Hz bandwidth) spectroscopic water vapor concentration monitor developed by Aerodyne Research, Inc. (described in more detail below) and an Edgetech 137-C3 chilled mirror dewpoint probe.

Cloud LWC was measured by the CAPS (Cloud/Aerosol Precipitation Spectrometer) probe manufactured by Droplet Measurement Technologies, Inc. It contains a Cloud and Aerosol Spectrometer (CAS: measuring particle diameters from  $0.5\text{--}50\text{ }\mu\text{m}$ ) and a Cloud Imaging Probe (CIP: measuring particle diameters from  $25\text{--}1550\text{ }\mu\text{m}$ ). The CAS collects both forward ( $2^{\circ}\text{--}12^{\circ}$ ) and backward ( $168^{\circ}\text{--}178^{\circ}$ ) scattered light from particles passing through a focused laser beam and sorts the measured pulse heights into 20 channels, each of which corresponds to a particle diameter. The CIP measures particle images by captur-

ing the shadow of the particles that pass through a focused laser. The collimated beam illuminates a linear array of 64 photodiodes. The array is scanned at a rate corresponding to 25  $\mu\text{m}$  of distance traveled, which thus determines the resolution of the probe.

A Differential Mobility Analyzer (DMA) system in the main cabin was used to measure aerosol size distributions from 10- to 350-nm diameter. The aerosol sample was drawn from the community inlet that was shared by other instruments in the main cabin. For the particle size range measured by the DMA system, the transmission efficiency of aerosol through the community inlet has been established to be essentially 100%. The aerosol sample flowed first to a Nafion drier (PermaPure PD07018T-12SS), in which the relative humidity of the sample was reduced to below 27%. The charging distribution of the dried aerosol was then brought to a known steady state by a  $^{210}\text{Po}$  charger. Nearly monodisperse aerosols were selected by a Cylindrical Differential Mobility Analyzer (CDMA, TSI Inc., model 3081) and counted by a Condensation Nucleus Counter (TSI Inc., model 3010), which has a 50% counting efficiency at 10-nm diameter. The CDMA was operated with an aerosol to sheath flow ratio of 0.604 L  $\text{min}^{-1}$  to 6.04 L  $\text{min}^{-1}$ . All flows were monitored and maintained by feedback controllers to compensate for environmental changes during airborne measurement. Using the scanning mobility technique (Wang and Flagan 1990), the DMA system generates a complete size distribution over the range of 10- to 350-nm diameter every 50 s. The DMA system was calibrated prior to the Halo experiment and accurately recovered both the peak size and number concentration of monodisperse calibration aerosols down to 15-nm diameter. Data from the DMA system were analyzed using the data inversion procedure described by Collins et al. (2002).

In addition to the DMA system, a Particle Measuring Systems, Inc. (PMS) Passive Cavity Aerosol Spectrometer Probe (PCASP)-100X and a PMS Forward Scattering Spec-

trometer Probe (FSSP)-100 were deployed. The two PMS optical probes were mounted under the left wing of the Twin Otter aircraft. Since a heater on the inlet of the PCASP reduced the relative humidity to below 30%, the PCASP provided measurements of dry aerosol size distributions. The PCASP has a measurement range of 0.1–3.5  $\mu\text{m}$  in diameter and was calibrated using Polystyrene Latex spheres of known sizes. Since the PCASP infers particle size from light scattered by the particle, the bin size of the PCASP was adjusted for measurement of dry marine aerosol, using the procedure of Liu and Daum (2000). The FSSP provided cloud droplet size distributions from 2.9- to 40- $\mu\text{m}$  diameter during the experiment. The FSSP was calibrated with spherical glass beads, and the bin sizes were adjusted for the refractive index of cloud droplets through Mie calculations. Three condensation nucleus counters were operated in parallel. One of them is the Ultrafine Condensation Nucleus Counter (UCNC, TSI model 3025), which measures the total concentration of particles larger than 3-nm diameter. The other two are Condensation Nucleus Counters (CNC, TSI model 3010) that report the total concentrations of particles larger than 6- and 10-nm diameter, respectively.

The Aerodyne Research, Inc. fast spectroscopic water vapor sensor (Kebabian et al. 2002) was employed for the first time in field measurements in the present study. The instrument operates by measuring the differential absorption of emission lines emanating from a simple argon gas discharge lamp in a water vapor absorption band in the near infrared ( $\sim 935$  nm) (Kebabian 1998; Kebabian et al. 1998, 2002). The lamp emission of interest is the neutral argon line at a frequency of  $10,687.43$   $\text{cm}^{-1}$  (Moore 1971; Kaufman and Edlen 1974). This line is close to, but not coincident with, a strong water vapor absorption line at  $10,687.36$   $\text{cm}^{-1}$  (Rothman et al. 1998). A longitudinal magnetic field of the proper strength (the Zeeman effect) (Jenkins and White 1957), is used to divide the lamp emission into one

frequency component (at lower energy,  $\nu_1$ ) that is strongly absorbed by the water vapor line, and a second frequency component (at higher energy,  $\nu_2$ ) that is only weakly absorbed. This fact forms the basis for a differential absorption measurement.

Referring to a schematic diagram of the sensor shown in Fig. 3.1, the argon discharge lamp, in the presence of the magnetic field, produces two components with equal intensity, but orthogonal circular polarizations. Discrimination between the two frequency components is accomplished by using polarization selection. The polarization selector produces a linearly polarized light beam of half the intensity and comprising alternate frequency components. When this light passes through a multipass absorption cell of off-axis astigmatic design (McManus et al. 1995) containing air with finite humidity, the lower frequency component,  $\nu_1$ , is more strongly absorbed than the other component. The resulting modulated signal ( $\Delta I = I_{\nu_2} - I_{\nu_1}$ ) can be measured using synchronous detection techniques and compared to the average DC signal level ( $I_0 = [I_{\nu_1} + I_{\nu_2}] / 2$ ) to provide an absorbance measurement ( $\Delta I / I_0$ ). A full description of the sensor and a comparison of its performance to a chilled mirror hygrometer and capacitance-based polymer sensor during the flight are presented in Keabian et al. (2002).

As shown in Fig. 3.1, air was drawn into the sensor through a stainless steel tube (2.5 cm outside diameter) that extended past the boundary layer of the aircraft and was positioned so that clean air was being sampled. In order to minimize water droplet intake, the tube inlet faced backward and had a protective lip welded onto it in order to prevent intake of liquid water that had condensed on the outside of the intake tube. No discernible uptake of liquid water was noted in approximately 40 hours of flight time. Upon entry into the fuselage cabin, the air flowed through a resistive heater in order to prevent any condensation in the polyethylene tubing that transported the air to the sensor. A  $15 \text{ L s}^{-1}$  blower, located

at the exit of the sensor, was used to maintain the air volume flow at  $\sim 10 \text{ L s}^{-1}$ . The air was then exhausted into the cabin. The sensor was operated at an electronic bandwidth and sample rate which provided a spatial resolution of 10 m at the  $50 \text{ m s}^{-1}$  flight speed of the Twin Otter aircraft.

### 3.4 Halo observations

Nine missions were flown over the period July 31 – August 10 2001, during which 44 individual cumulus clouds were sampled. Because of typically short cloud lifetimes, most of the sampled clouds were characterized by only a few (e.g., three) aircraft traverses. Subsequently we will present statistical data on the sampled clouds, in terms of frequency of halo occurrence and the spatial distribution. At 0047 UTC, on August 8, 2001, a particularly long-lived cumulus cloud (cloud 6 in Table 3.2) was encountered and sampled extensively. This cloud constitutes an ideal test case of a trade wind cumulus. For this reason, we devote considerable attention to measurements made on this cloud. We also focus on the ability to numerically simulate the development of this particular cloud because it provides an opportunity to study the development of the cloud halo and its radiative impact in some detail. As noted, for each traverse, the aircraft was at least 3 km away from the cloud lateral boundary at the beginning and end of the traverse. The aircraft made two complete cycles of penetrations from above cloud top to below cloud base; observation 1 consists of traverses 1 through 8, and observation 2 corresponds to traverses 9 through 14 (Fig. 3.2). The total elapsed time of the 14 traverses through the cloud was 78 min.

The vertical profile of ambient conditions (Fig. 3.3) was acquired by the aircraft during vertical probing about 2.5 h before the cloud was sampled. The sounding profile features a tropical inversion layer between 1600–1900 m, capping the trade-wind boundary layer with

stable, dry air. The sounding shows the atmosphere is conditionally unstable below 890 hPa, with an absolutely stable layer at 810–840 hPa. At its mature stage, the cloud base was at about 500 m and the top around 2200 m, 300 m above the top of the inversion layer, as shown in Fig. 3.4. The cloud was widest, 6–8 km, at an altitude of about 1500 m. The cloud region is operationally defined by a measured LWC exceeding  $0.01 \text{ g m}^{-3}$ . The cloud width so defined might not necessarily correspond to the visible cloud width. The maximum and the horizontally-averaged values of in-cloud LWC at each altitude, shown in Fig. 3.4b, exhibit a similar trend that increases with height until a point about 300 m below the cloud top, after which LWC falls rapidly to zero. This LWC trend is similar to that of Australian marine cumulus reported by Warner (1955). The cloud LWC and cloud width (Fig. 3.4) exhibited comparatively little change with time over the entire observation ( $\sim 78$  min). This LWC persistency agrees with Warner’s (1977) observations of small cumuli that the average turbulent velocity and LWC can last nearly unchanged for periods up to 20 min during the mid stage of the cloud lifetime, although the life of the present cloud was relatively long compared with observations reported by Warner (1977). The mean and maximum LWC show similar vertical distribution patterns, also peaking around 2000 m.

### 3.4.1 Measured humidity profiles

The measured humidity profile and LWC distribution for a particular traverse (traverse 12) are shown in Fig. 3.5. We report the water vapor in terms of specific humidity ( $\text{g kg}^{-1}$ ). An empirical expression similar to that used by Lu et al. (2002) is used to define the edge of the halo based on the e-folding decay of specific humidity,  $q_{ve}(z)$ , from the in-cloud average,  $\bar{q}_{vc}(z)$ , to the ambient value,  $\bar{q}_{venv}(z)$ ,

$$q_{ve}(z) = \bar{q}_{vc}(z) - \{[\bar{q}_{vc}(z) - \bar{q}_{venv}(z)](1 - e^{-1})\} \quad (3.1)$$

The humidity far away from cloud lateral boundaries was not necessarily smooth; for example in Fig. 3.5, the smoothed data still show a wavy distribution with small amplitude. Because sounding profiles were not available for each cloud, we approximate  $\bar{q}_{venv}(z)$  by averaging data points sufficiently far from the cloud. (Interestingly, the ambient values are not necessarily the same on both sides of the cloud.) From the smoothed data shown in Fig. 3.5, it can be seen that the measured humidity profile outside the cloud, beginning from the mark “c” to the two lower horizontal lines, can be approximated by an exponential decay. For some traverses, for example traverse 4 (Fig. 3.6), the aircraft did not fly far enough from the cloud to reach a constant ambient humidity. In this case, the humidities at the start and the end of the traverse are used to define the far-ambient humidities. Returning to Fig. 3.5, the humidity halo at the downshear side of the cloud is about four times broader than that at the upshear side.

The wind vector  $\mathbf{u}$  is defined as positive in the positive  $x$  direction for Cartesian coordinates ( $x - z$ ) in the east-west and vertical directions. For example, an easterly wind is defined as negative. The vertical wind shear vector is defined as  $d\mathbf{u}/dz$ . The direction of the shear vector is positive if  $d\mathbf{u}/dz > 0$ , and vice versa. The downshear and upshear directions are defined by the direction of the shear vector; in that sense, the shear vector always points in the downshear direction. The cloud morphology is tilted and stretched by the vertical shear, and the cloud is basically tilted to the downshear direction. Consider an easterly wind ( $\mathbf{u} < 0$ ) the velocity of which decreases as  $z$  increases; in this case, the shear vector is positive ( $d\mathbf{u}/dz > 0$ ) and points in the positive  $x$  direction. Then for a cloud, the

downshear direction is in the positive  $x$  direction, which is on the east side of the cloud. A westerly wind ( $\mathbf{u} > 0$ ) the velocity of which increases with height has the same direction of the shear vector as the previous case. Therefore, the downshear and upshear directions are the same in these two cases.

The vertical distribution of the humidity halo on both sides of the cloud was determined (Fig. 3.7). Perry and Hobbs (1996) found that the presence of a stable layer can limit the vertical distribution of the halo. In Fig. 3.7, in accord with this observation, we note that the cloud halo is distributed mainly below the inversion layer on both sides of the cloud. The vertical east-west wind profile shows a weak wind shear with the easterly wind increasing with height roughly below the inversion base where most of the halo is present; therefore, the downshear side is on the west side relative to the cloud. The vertical distribution of halo shows that halo width is largest at the lowest altitudes, decreasing with height below the inversion base, also in both of the downshear and upshear directions. This trend is similar to the observations of Perry and Hobbs (1996) that when the inversion layer lies in the middle of the cloud, the halo tends to be broader at the lower levels. The figure also shows the halo is wider in the downshear than the upshear direction. The peak of the halo width above the inversion base for observation 1 could be due to a hole in the cloud as shown in the simulation later. The halo becomes much broader at later times (e.g., observation 2) at the lower cloud levels in the downshear direction, but the halo at the upshear side stays relatively unchanged with time.

From the 44 individual clouds sampled over the two-week period, we select nine clouds for which four or more traverses were made for statistical analysis (Table 3.2). Humidity halos were identified approximately 54% of the time during the total of 60 traverses. All halos were less than two cloud radii in horizontal extent. In general, as indicated in Table

3.3, humidity halos are more frequent and broader at the downshear side (55% and 0.67 cloud radii) than the upshear side (44% and 0.41 cloud radii). The frequency of occurrence and width of the cloud halo on the upshear side observed in the present study are close to those of the cumulus clouds off the coasts of Oregon and Washington reported by Perry and Hobbs (1996); however, the frequency of occurrence and width at the downshear side in the present study are less than reported by Perry and Hobbs (1996). One possible explanation is that the clouds sampled in the present study consist of a higher fraction of young/mature clouds.

The vertical distribution of these sampled halos is shown in Fig. 3.8. The data points are categorized into five altitude bins. The mean of the data for each altitude bin represents the halo width at that altitude range with the standard deviation as its error bar. The figure shows the halo basically is broad at the lower levels of the cloud and narrow around cloud top. In this figure, the large error bars for the downshear side suggests that the halo width is not a strong function of height. The sampled halo might correspond to different cloud ages because the halo width in the downshear direction increases with cloud age; however, the halo width decreases with height at the upshear direction, especially at lower levels. According to the study of Perry and Hobbs (1996), the vertical distribution of halos in the figure implies that the majority of clouds sampled in this study were at their young/mature stage.

### **3.4.2 Aerosol and cloud droplet size distribution measurements**

Trade wind cumulus clouds are frequently situated in a transition region between the marine boundary layer and the free troposphere. Aerosol distributions in these two regions are typically quite different (Raes et al. 2000), and understanding the nature of new particle

formation in each region remains an important issue. As noted in the Introduction, new particle formation has been reported in the vicinity of clouds. Because of the elevated humidity, the cloud halo represents a potentially fertile region for new particle formation.

Typical profiles of the total particle concentration ( $D_p > 10$  nm) and particle size distribution ( $0.10 \mu\text{m} < D_p < 3.5 \mu\text{m}$ ) measured during the campaign are shown in Fig. 3.9. Generally, the total particle number concentration showed little variation within the marine boundary layer, and was about  $150 \text{ cm}^{-3}$ . The total particle number concentration increased to about  $300 \text{ cm}^{-3}$  in the free troposphere, with a maximum near cloud top, at an altitude of 1900 m in the case shown. The number concentration of particles measured by the PCASP ( $0.10 \mu\text{m}$  to  $3.5 \mu\text{m}$ ) were anti-correlated with total particle number concentration; in this size range particle number concentration decreased from  $60 \text{ cm}^{-3}$  in the marine boundary layer to about  $20 \text{ cm}^{-3}$  in the free troposphere. This change is likely due to aerosol processing by clouds within the marine boundary layer, which produces particles with diameters that fall into the PCASP measurement range.

Fig. 3.9 shows a typical example of the dry aerosol size distributions measured in the vicinity of clouds at different altitudes. Based on the characteristics and measurement altitudes, the size distributions are grouped into three categories: free troposphere, transition region, and marine boundary layer. The size distributions are shown as  $dN/d\log D_p$  ( $\text{cm}^{-3}$ ). In the free troposphere, the aerosol generally has the highest number concentration, with the majority of the particles smaller than  $0.1 \mu\text{m}$ . The size distribution is unimodal with a peak concentration of about  $300 \text{ cm}^{-3}$  at about 65 nm (A and G). In the marine boundary layer, particles displayed typical bimodal distributions that result from aerosol processing through nonprecipitating cloud cycles. The mode at the smaller diameter ( $\sim 45$  nm), which is too small to be activated to form cloud droplets, is often referred to as the interstitial

mode. The mode near 200 nm results from evaporated cloud droplets; these particles are larger than their pre-cloud sizes, mainly as a result of uptake of soluble trace gases and subsequent conversion to nonvolatile compounds. Within the marine boundary layer, the aerosol size distributions at different altitudes (D, E, F, J, and K) are similar to each other. The peak concentrations of the two modes are about 150 and 220  $\text{cm}^{-3}$ . The local minimum between the two modes is at  $75\pm 10$  nm, which reflects the supersaturation in the clouds (Hoppel et al. 1996). Assuming the aerosol to be composed mainly of  $\text{NH}_4\text{HSO}_4$ , the supersaturation of the marine boundary layer clouds is estimated as  $0.075\pm 0.02\%$ .

The aerosol distributions at locations B, H, C, and I, which are measured near the inversion layer, displayed a transition from free tropospheric to marine boundary layer aerosol. As the average measurement altitude decreases into the marine boundary layer, the mode resulting from evaporated cloud droplets emerges.

Particles resulting from recent nucleation events were observed at three altitudes (1500, 1180, and 900 m, Fig. 3.9a), on the downshear side of the cloud (cloud 6 in Table 3.2). The newly formed particles were evidenced by the difference between the particle concentrations reported by the three CNC, which have different detection limits of 3, 6, and 10 nm, respectively (Figs. 3.9f–g). In all three cases, the newly formed particles were observed in the region with high relative humidity, a condition that favors homogeneous nucleation.

### 3.5 Numerical simulation

Lu et al. (2002) evaluated the ability to numerically simulate cloud and halo development for several cases that have been reported in the literature. The numerical simulations focused on the development of humidity regions around the clouds (these regions had not necessarily been probed in the reported aircraft studies). In this section, we numerically

simulate the large, persistent cloud discussed in detail in section 3.4, for which we employ the three-dimensional, nonhydrostatic version of RAMS (Pielke et al. 1992; Walko et al. 1995).

Jiang and Cotton (2000) conducted a large eddy simulation of trade-wind cumulus convection in Barbados using RAMS. The simulation was initialized by imposing a random white noise in temperature at the lowest levels of the model. With initial random temperature fluctuations, many small cumuli tend to evolve in the domain (e.g., Stevens et al. 2001). An alternate initialization procedure, better suited to generating a single cloud, is to apply a thermal bubble method. The thermal perturbation is assumed to be a Gaussian function, similar to that used by Steiner (1973),  $\theta' = \alpha \exp\{-[(x-x_c)/0.5\lambda_m]^2\} \sin^2(\pi z/h)$ , where  $\alpha$  is the maximum amplitude of the perturbation,  $x_c$  is the center of the model domain,  $\lambda_m$  is a characteristic horizontal length scale of the thermal fluctuation (McNider and Kopp 1990), and  $h$  is the effective perturbation depth. The size of the initial pulse greatly influences the numerical development of the cloud (e.g., Murray 1971). Different perturbations were tested to find that for which the simulated cloud resembled that observed. An initial thermal perturbation of  $\alpha = 0.1$  K with  $\lambda_m = 632$  m applied in the central domain of  $1 \text{ km} \times 1 \text{ km}$  below  $h = 500$  m produced a simulated cloud closest to that observed. (Although cases were tried with  $\lambda_m = 4$  km, close to the observed averaged cloud width, this perturbation did not produce a cloud similar to that observed.) Our experience shows that a humidity perturbation saturating the lower levels (e.g., below 214 m) of the model, confined in the central region, is required. We have arbitrarily set the  $v$ -component of wind to be zero, so that the cloud movement can be followed easily.

The simulation domain has a horizontal resolution of 100 m, equivalent to a 2 s measurement resolution (at  $50 \text{ m s}^{-1}$  flight speed), and vertical resolution of 40 m at the lowest altitude with a vertical stretching ratio of 1.1. The simulation domain is thus  $6 \text{ km} \times 6 \text{ km} \times$

11 km, the horizontal domain size being large enough to cover the cloud and the associated cloud halo. The sea surface temperature (SST) was prescribed using the NCEP Reynolds average SST of 300 K ([http://podaac.jpl.nasa.gov/reynolds/reynolds\\_browse.html](http://podaac.jpl.nasa.gov/reynolds/reynolds_browse.html)) in the vicinity of Hawaii in August 2001. The lateral boundary condition is periodic, and the upper and lower boundaries are rigid lids. The averaged cloud droplet size distribution (Fig. 3.10) observed during traverse 7 by the FSSP-100, was integrated over the droplet spectrum to give a cloud droplet number concentration ( $N_t$ ) of  $76 \text{ cm}^{-3}$ . By fitting the data with a modified gamma distribution used in RAMS (Walko et al. 1995),

$$n(D) = \frac{N_t}{\Gamma(\nu)} \left( \frac{D}{D_n} \right)^{\nu-1} \frac{1}{D_n} \exp \left( -\frac{D}{D_n} \right) \quad (3.2)$$

with this cloud droplet number concentration value, we obtain the gamma distribution shape parameter  $\nu = 7.8$  and the characteristic diameter  $D_n = 1.8 \mu\text{m}$ . The observed cloud droplet size distribution shown in Fig. 3.10 is well represented by a gamma distribution.

The simulated cloud at 16 min (Fig. 3.11) most closely resembles that during the period of observation. The simulated cloud base and top are around 500 m and 2000 m, respectively, which are close to the observation (300 m and 2200 m). The cloud top is a few hundred meters above the inversion, as also seen in observations by Raga et al. (1990). The vertical profile of the simulated maximum LWC at 16 min, shown in Fig. 3.12, exhibits reasonable agreement with the observed vertical profile and values of the maximum LWC. The simulated maximum LWC is only slightly smaller than the observation. Also, the simulated vertical profile of the maximum specific humidity at 16 min matches that sampled. Since the simulated cloud is smaller than the observation, the simulated halos are expressed in units of cloud radii so that the factor of absolute cloud width can be eliminated. The

vertical profile of the simulated cloud halo (Fig. 3.13) agrees well with the observation. For example, the simulated halo is similar to the observation 2 (1) below (above) 0.6 cloud depth. The broadest halo is predicted at the cloud base with the width of 0.6 cloud radii at the upshear side and 1.5 cloud radii at the downshear side, as compared to the observations of 0.7 cloud radii and 1.3 cloud radii, respectively. The peak value of the halo width at a cloud depth of 0.7 in Fig. 3.7 resulted from the hole in the cloud (Fig. 3.11). In general, the simulated halo is broader at the downshear side of the cloud than the upshear side throughout the simulated cloud life. However, in this simulation, the cloud only lasts for 24 min, considerably shorter than the observation (78 min).

In order to demonstrate a clear relationship between the halo and the shear vector, we conduct a simulation by increasing the wind shear. In the presence of wind shear, the cloud is tilted and stretched in the downshear direction, and the cloud is basically moving with the dominant ambient easterlies. This simulation shows the cloud is growing on the upshear side and dissipating on the downshear side, as reported in the numerical simulation (e.g., Vaillancourt et al. 1997) and observation (e.g., Telford and Wagner 1980). Results in Fig. 3.14a show an asymmetric distribution of halo relative to the cloud, and the halo is encompassed by an asymmetric clear-air turbulence adjacent to the cloud. Dissipation of the cloud formed previously can produce the halo. However, the halo forming on the upshear side of the cloud in Fig. 3.14a is in the direction of cloud propagation (also the halo on the downshear side of the cloud in Fig. 3.11), and can not be due to the remains of the cloud formed previously. The vertical wind velocity in this area shows the updraft velocity outside the cloud boundary at the upshear side and a large fluctuation with updraft and downdraft at the downshear side. Therefore, the high correlation of clear-air turbulence area with the halo distribution suggests that lateral turbulent mixing of the humid cloudy air with dry

ambient air can either evaporate the cloud droplets or detrain the high humidity outside the cloud boundary and produce the halo. This clear-air turbulent mixing area is broader at the dissipating downshear side than at the growing upshear side. The above mechanism and the cloud-environment relative motion result in this asymmetric halo distribution. This strong correlation of the asymmetric halo distribution with the turbulent mixing area also emerged in the previous simulation (Fig. 3.11) and observations of Malkus (1949) and Ackerman (1958). When the cloud starts to dissipate, the dissipated cloud gradually leaves a broad area of humidity halo and turbulence (Fig. 3.14b). At this time, the halo is not only limited to the lower levels but distributed vertically.

In summary, while the simulated cloud width and lifetime are smaller than those of the observed cloud, the vertical profiles of LWC and water vapor, the locations of cloud top and base, and the magnitude and the vertical profile of the cloud halo width (in terms of cloud radii) in different wind shear regimes, agree well with observation. By conducting a numerical experiment with increased vertical wind shear, we find the halo distribution is highly correlated with the clear-air turbulence temporally and spatially as also seen in past observations. This suggests that turbulent mixing at the cloud boundary can evaporate cloud droplets or detrain high humidity to the adjacent clear-air region, in addition to the remains of the cloud formed previously, producing the halo.

### **3.6 Simulated radiative effect of cloud and halo**

The simulated cloud and other atmospheric properties are used as input for a radiation calculation. The 3D radiative transfer model utilized in this study is SHDOM (Spherical Harmonic Discrete Ordinate Method; Evans 1993, 1998). For the SW broadband (0.2–

4  $\mu\text{m}$ ) calculation, the correlated  $k$  distribution (Fu and Liou 1992) is assumed for the gaseous absorption by methane, ozone, nitrous oxide, carbon dioxide, and water vapor. There are a total of 54  $k$ 's over the six solar bands. Cloud droplet optical properties are calculated based on Mie theory. The model has been modified to allow a 3D water vapor distribution for the purpose of calculating the halo radiative effect.

The 2D simulated cloud and its associated halo from RAMS serve as input into the 3D SHDOM due to the extensive computation time involved for the 3D cloud geometry. The radiative calculation by SHDOM is carried out every two minutes. The solar zenith and azimuthal angles at the time of measurement are  $33.38^\circ$  ( $\cos \theta = 0.835$ ) and  $177.2^\circ$ , respectively. In the calculation, there are 8 zenith angles in both hemispheres and 16 azimuthal angles used to calculate radiation flux. One important issue associated with the cloud halo is the amount of solar energy absorbed by it. Based on the radiative energy balance, the atmospheric absorption between two altitudes  $z_a$  and  $z_b$  ( $z_b < z_a$ ) for a vertical column located at  $x$  of a 2D ( $x - z$ ) medium can be calculated by (see the appendix of Marshak et al. 1998),

$$\int_{z_b}^{z_a} -\frac{\partial F_z}{\partial z} dz + \int_{z_b}^{z_a} -\frac{\partial F_x}{\partial x} dz \quad (3.3)$$

where  $F_z$  is the net downward flux ( $\text{W m}^{-2}$ ) and  $F_x$  is the net horizontal flux in the  $x$ -direction. If the domain-averaged horizontal photon transport is zero, that is,

$$\frac{1}{L} \int_0^L \int_{z_b}^{z_a} -\frac{\partial F_x}{\partial z} dz dx = 0 \quad (3.4)$$

where  $L$  is the length of the horizontal domain ( $x$ ), the atmospheric absorption can be calculated by only the first term of Eq. (3.3). Because of the cyclic boundary condition

used for the SHDOM calculation, we can apply Eq. (3.4) so that the domain-averaged (over the  $x$ -axis) atmospheric absorption ( $A$ ) is simply

$$\frac{1}{L} \int_0^L [F_z(z_a) - F_z(z_b)] dx \cong \sum_{i=1}^{N_x} [F_z(z_a) - F_z(z_b)]_i, \quad (3.5)$$

where  $N_x$  is the number of grid cells in the  $x$  direction. Fig. 3.15 shows the atmospheric column absorption (between the surface and 3.4 km) both in the presence and absence of the halo. The absence of the halo scenario is established numerically by replacing the absolute humidity of the halo region (shaded boxes as shown in Fig. 3.11) with that of the far ambient; therefore, the difference of the two scenarios represents the maximum halo radiative effect. The largest value the halo-enhanced SW column absorption ( $\Delta A$ , dotted line in Fig. 3.15) is  $2.49 \text{ W m}^{-2}$  (2.3% of the column absorption without the halo,  $106.29 \text{ W m}^{-2}$ ) and appears at 18 min simulation time when the lower portion of the cloud dissipates, leaving a significant amount of high humidity. It is noted that  $\Delta A$  strongly depends on the cloud age, the magnitude being small when the cloud is forming but becoming larger at the mature and dissipation stages. The enhanced atmospheric absorption due to the halo averaged over the mature and dissipation stages of the cloud, is  $1.32 \text{ W m}^{-2}$ , approximately 1.3% of the column absorption in the absence of the halo ( $103.28 \text{ W m}^{-2}$ ). We are also interested in estimating the amount of the increased SW absorption of the cloud over its lifetime. Although information on the measured cloud before or after the observations is not available, we can utilize the model results to perform this calculation. The value of  $\Delta A$  averaged over the simulated cloud lifetime of 24 min is  $0.63 \text{ W m}^{-2}$ , corresponding to a 0.6% increase of the column absorption over that without the halo ( $103.78 \text{ W m}^{-2}$ ).

The spatial pattern of the radiative effect of the cloud halo at simulation time 16 min is

shown in Fig. 3.16. This figure represents the difference between radiative heating rates in the presence and absence of the cloud halo. Because the radiative heating rate is proportional to the absorbed power per unit volume, the positive values in the figure indicate that there is increased absorption due to the halo. Fig. 3.16 shows maxima near the cloud top at both sides, with maximum value of  $0.32 \text{ K hr}^{-1}$  at 2100 m. Other simulation results (not shown) also show that the largest local halo radiative effect is located near the cloud top, and this local effect is largest for the mature cloud. Both simulated and observed clouds are relatively shallow, without an anvil or horizontal outflow region.

Conant et al. (1998) and Vogelmann et al. (1998) find little discrepancy between predictions of radiative transfer models of water vapor absorption and observations for the case of clear skies. Arking (1999), however, reports some discrepancy when clouds are present. Some enhancement of atmospheric absorption will exist due to cloud inhomogeneity (Marshak et al. 1998). Because of the covariance of cloud fields and water vapor fields in trade cumulus systems and the potential enhancement in atmospheric absorption this geometry produces, a question relevant in the present simulation is the extent to which cloud halos contribute to discrepancies between observed and predicted atmospheric absorption based on the assumption of horizontally homogeneous water vapor fields.

In summary, the radiative effect of the halo depends on the stage of the cloud development and the location with respect to the cloud. The halo radiative effect is largest near the cloud top during the cloud mature and dissipation stages. The enhanced SW column absorption (surface to 3.4 km) averaged over this period for the simulated cloud is  $1.32 \text{ W m}^{-2}$ , contributing 1.3% change to the column absorption in the absence of the halo. However, the enhanced absorption is only  $0.63 \text{ W m}^{-2}$  (0.6%) averaged over the simulated cloud lifetime. This represents a small fraction of the 6% discrepancy between models and

observations reported by Arking (1999) and others and commonly referred to as “anomalous cloud absorption.”

### 3.7 Conclusions

An aircraft campaign sampling trade wind cumulus clouds termed, Cloud Halo, was conducted in the vicinity of Oahu, Hawaii in July–August 2001, the main purpose of which was to study humidity distributions around the clouds. One especially persistent cloud was extensively sampled and numerically simulated using the RAMS model. The simulated cloud, though narrower than the actual, resembled the observations with respect to locations of cloud top and base, vertical distribution and magnitude of maximum/mean LWC, maximum specific humidity, and halo vertical profile and width at the mature cloud stage. The halo broadens with time at the lower levels at the downshear side of the cloud. Both observations and simulations suggest that an inversion layer limits the presence of cloud halos to below the layer.

Among 60 traverses through clouds, halos were identified around half of the time, all of which had spatial extent less than two cloud radii. The frequency of occurrence and width of the halos in the downshear and upshear directions are 55% and 0.67 cloud radii and 44% and 0.41 cloud radii, respectively. In the young/mature stage of cloud development, halos tend to be broad at the lower levels of the clouds and narrow around the cloud top, on both sides of the cloud. The halos are also broader in the downshear direction than in the upshear direction.

Numerical simulation shows the asymmetric halo distribution relative to the cloud in the presence of vertical wind shear is associated with the asymmetric clear-air turbulence area,

in agreement with past observations in Malkus (1949) and Ackerman (1958). Therefore, the simulation results suggest that turbulent mixing of the humid cloudy air with the dry adjacent clear air can either evaporate cloud droplets or detrain the high humidity from the cloud boundary, adding it to the halo resulting from the remains of the cloud formed previously. Because of growth on the upshear side and dissipation on the downshear side, the halo is broader on the downshear than the upshear side of the cloud. Simulation also shows that the halo distribution broadens with cloud age.

Observations and simulation of the cloud halos in this study generally agree with observations of Perry and Hobbs (1996) and numerical simulations of Lu et al. (2002). The trade wind cumulus clouds sampled in this study were shallow clouds without anvils or cloud outflows. We can expect that more convective clouds, such as thunderstorms or clouds in the ITCZ, with cloud outflow regions near cloud tops, will exhibit broader halos.

Regions in the vicinity of clouds are favorable for new particle formation. Aerosols measured in the vicinity of the trade wind cumulus clouds reflected the three regimes — free troposphere, transition zone, and marine boundary layer. In the free troposphere, the aerosol size distribution was found to be unimodal with a peak size at about 65 nm, while being bimodal in the marine boundary layer with peaks at about 45 nm and 185 nm. These observations are consistent with prior measurements reported in the literature. Particles resulting from recent nucleation events, when observed, occurred on the downshear side of the cloud, coincident with the region of largest halo.

Radiative absorption of the simulated halo has been estimated using the radiative transfer model, SHDOM. Results show that the halo radiative effect is largest at the cloud mature and dissipating stages. A peak column absorption (surface to 3.4 km) due to the halo of  $2.49 \text{ W m}^{-2}$  (2.3%) is noted early in the cloud dissipation stage. The temporally and spatially

averaged SW column absorption during this period for the simulated cloud is  $1.32 \text{ W m}^{-2}$ , a 1.3% increase of the column absorption over that in the absence of a halo. However, the increased absorption is only  $0.63 \text{ W m}^{-2}$  (0.6%) when averaged over the simulated cloud lifetime. This represents a small fraction of the 6% discrepancy between models and observations reported by Arking (1999) and others and commonly referred to as anomalous cloud absorption. The spatial distribution of the halo radiative effect is largest near cloud top, which, in addition to the humidity halo, results in conditions favorable to homogenous nucleation.

### 3.8 Acknowledgments

This work was supported by National Science Foundation Grants ATM-9907010 and ATM-9910744. This work was also supported in part by the Office of Naval Research. The authors wish to acknowledge Dr. William C. Conant for helpful comments. We also thank anonymous reviewers for their valuable comments on this work.

Table 3.1: Airborne and ground-based measurements of cloud halos

	<b>Cloud</b>	<b>Location</b>	<b>Halo observations</b>
Malkus (1949)	trade-cumulus	Caribbean Sea	Clear-air disturbance was found generally in the downshear from the cloud, broader on the downshear than the upshear side. This clear-air disturbance was later related to the humidity halo by Ackerman.
Ackerman (1958)	trade-cumulus	Caribbean Sea	The major regions of clear-air disturbance (e.g. water vapor field) was found on the downshear side of the cloud and broadens as cloud ages.
Telford and Wagner (1980)	small cumulus	off the northeast shoreline of Chesapeake Bay, USA	Clear-air disturbance in water vapor mixing ratio was only on the dissipating (downshear) side of the cloud.
Radke and Hobbs (1991)	small cumulus	east of the Cascade Mts., Washington, USA	High humidity and Aitken nucleus concentration in clear-air regions near cloud extended out to distances of several cloud radii.
Raymond et al. (1991)	mountain thunderstorm	New Mexico, USA	Layers of elevated humidity were visible as detraining stratus clouds.
Hobbs and Radke (1992)	small cumulus	east of the Cascade Mt., Washington, USA	Elevated humidity and Aitken nuclei in the vicinity of cloud at the cross-shear direction.
Perry and Hobbs (1996)	small-medium sized cumulus	off the coast of Washington and Oregon, USA	First statistical analysis of cloud halos
Kollias et al. (2001)	marine fair-weather cumuli	Virginia Key, Miami, Florida, USA	Large moisture gradients were observed at the cloud laterals by radar wind profiler.
Weber et al. (2001)	frontal clouds	remote South Pacific Ocean (153°E, 47°S)	Gradual decrease in RH (3% per km) beyond the cloud boundary was identified.

Table 3.2: Characteristics of nine trade wind cumulus clouds studied

<b>cloud no.</b>	<b>cloud</b>	<b>top (m)</b>	<b>base (m)</b>	<b>depth (m)</b>	<b>*average width (km)</b>	<b>traverses</b>
1	August 3 cloud 3	1925	457	1468	1.15	4
2	August 6 cloud 1	1731	488	1243	6.77	5
3	August 6 cloud 6	1782	594	1188	1.53	7
4	August 7 cloud 1	2026	453	1573	4.66	6
5	August 7 cloud 5	1970	568	1402	2.05	6
6	August 7 cloud 6	2327	534	1793	2.44	14
7	August 9 cloud 2	**	690	**	**	6
8	August 9 cloud 3	1681	486	1195	7.29	8
9	August 9 cloud 4	1676	742	934	2.62	4
average		1890	557	1350	3.56	total=60

\* Average cloud width is obtained by averaging the cloud width throughout the cloud depth

\*\* Cloud top altitude is not available for this cloud

Table 3.3: Cloud halo statistics for the current study as compared with Perry and Hobbs (1996)

Wind direction	this study			Perry and Hobbs (1996)		
	Hawaii trade wind cumulus averaged			Cumulus clouds off the coast of averaged halo		
	sample size	halo frequency	halo width (cloud radii)	sample size	halo frequency	width (cloud radii)
Downshear	38	55%	0.67	56	75%	1.3
Upshear	39	44%	0.41	57	35-40%	0.3

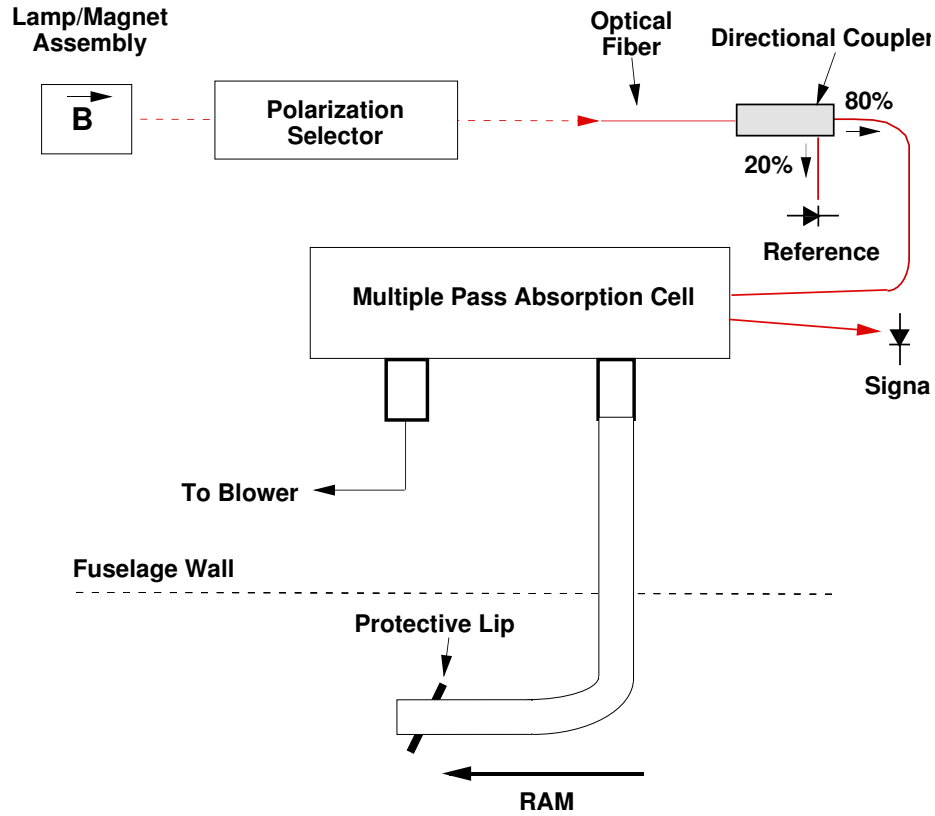


Figure 3.1: Schematic of the Aerodyne Research, Inc. spectroscopic water vapor sensor. Also shown are the relative intensities of the frequency components produced by the Zeeman (magnetic) splitting of the lamp output. The lower frequency component,  $\nu_1$ , is absorbed by the water vapor in the absorption cell, producing a net AC signal at the detector. See text for a full explanation.

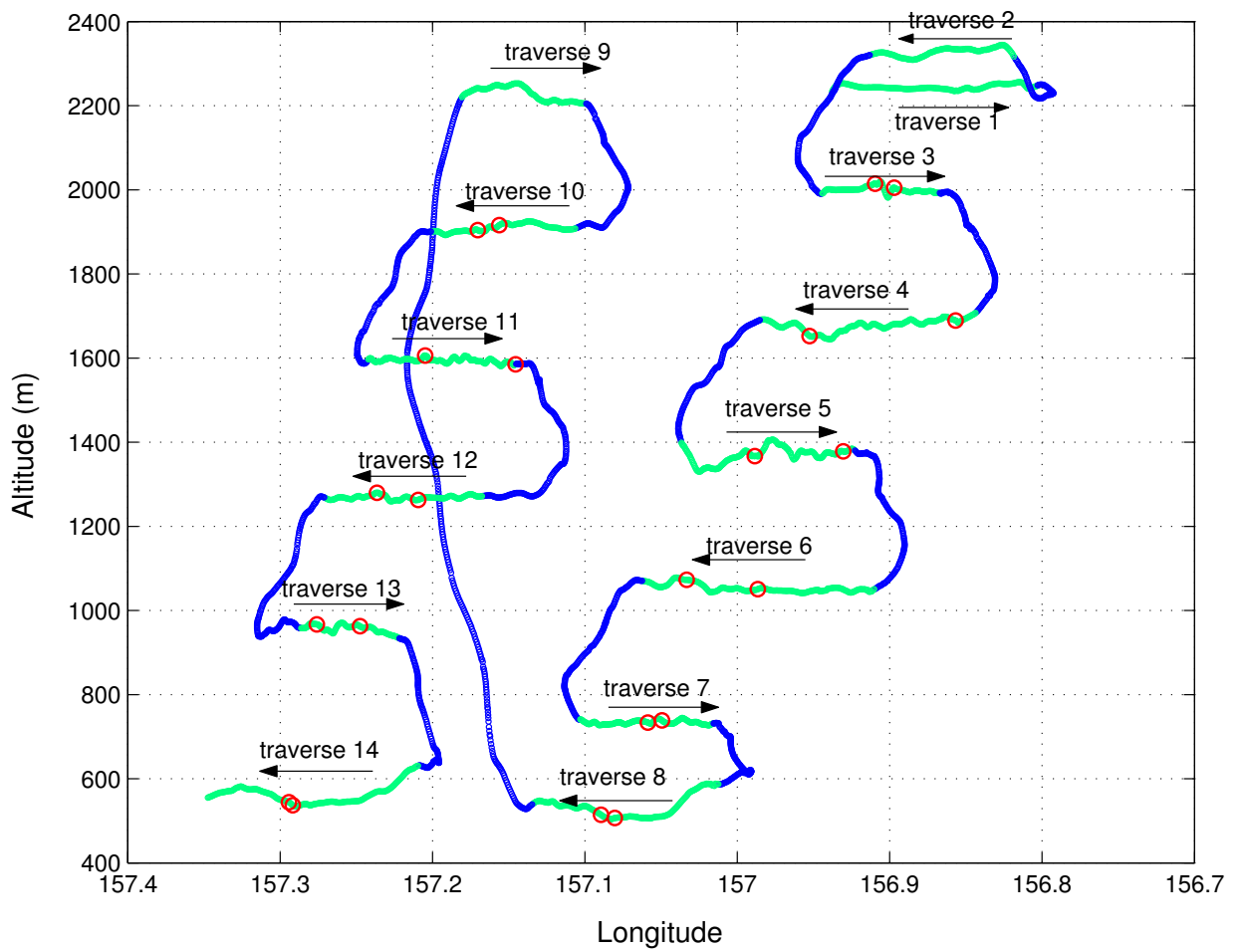


Figure 3.2: Flight path for the cumulus cloud at 0047 UTC, on August 8, 2001. A total of 14 traverses (green) are shown. Observation 1 represents traverses 1 through 8; observation 2 represents traverses 9 through 14. Red circles denote the cloud boundary.

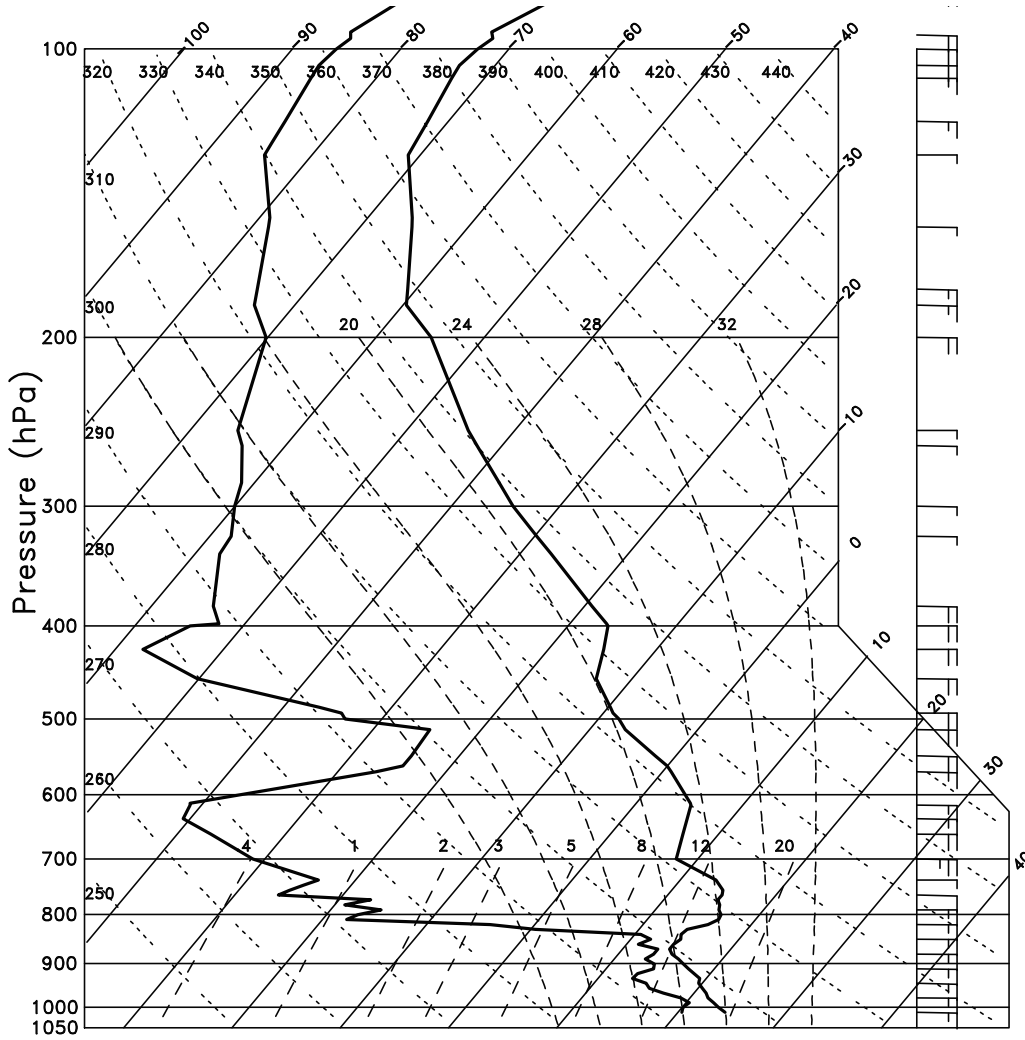


Figure 3.3: Skew  $T$ -log $p$  diagram of the ambient sounding profile on August 8, 2001 taken for the extensively studied cloud (in Sections 3.3 and 3.4) at 0047 UTC, 21.57°N, 156.82°W. Temperature and dewpoint temperature profiles are represented by thick lines. The skewed abscissa is temperature (°C), and the ordinate is pressure (hPa). Dotted lines (K) represent dry adiabats. Curved, dashed lines (°C) are pseudoadiabats. Straight-dashed lines ( $\text{g kg}^{-1}$ ) are isopleths of the saturation water vapor mixing ratio. The north-south wind is not shown.

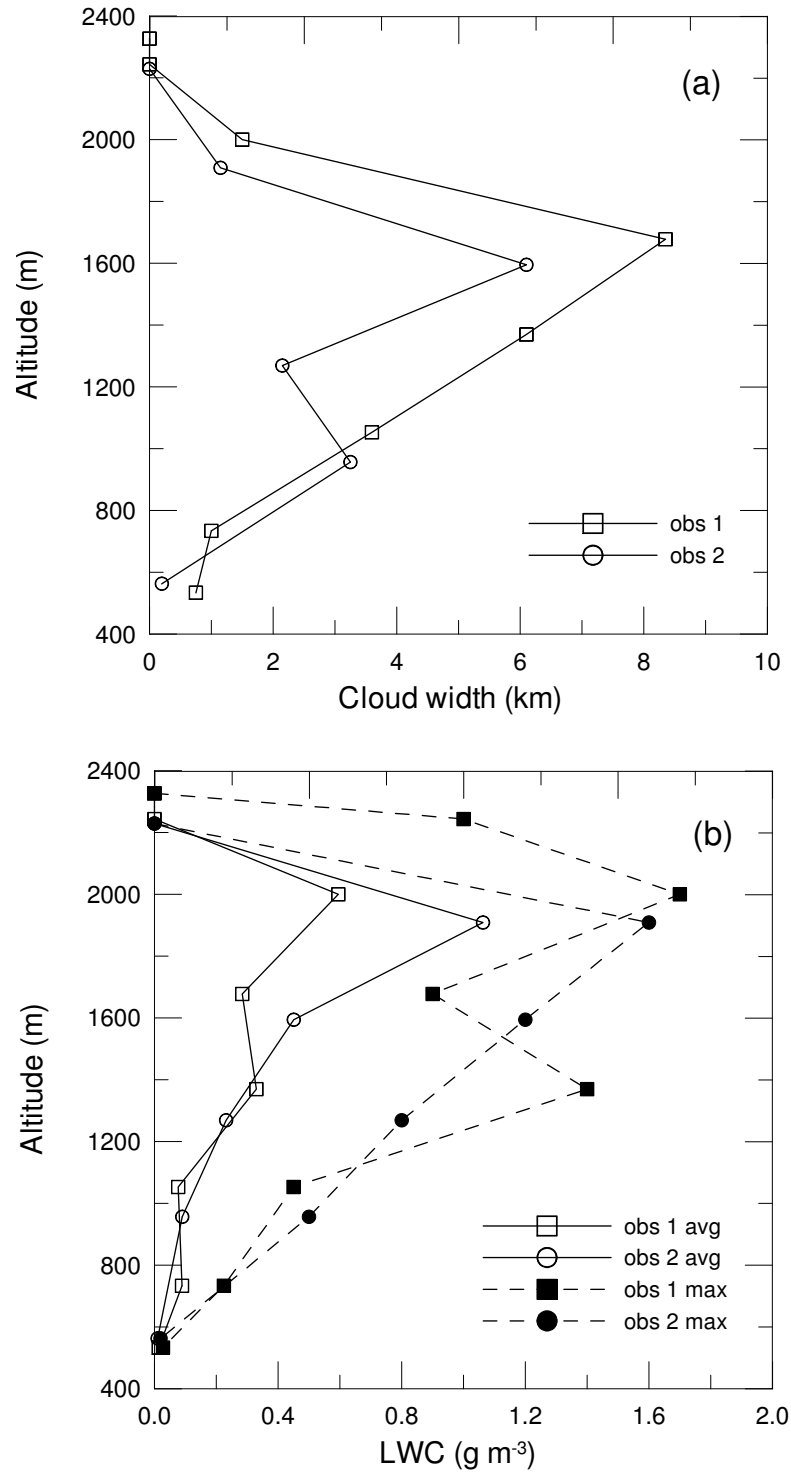


Figure 3.4: Vertical profiles of (a) cloud width and (b) the horizontally averaged and maximum cloud LWC for each traverse for observations 1 (traverses 1–8) and 2 (traverses 9–14).

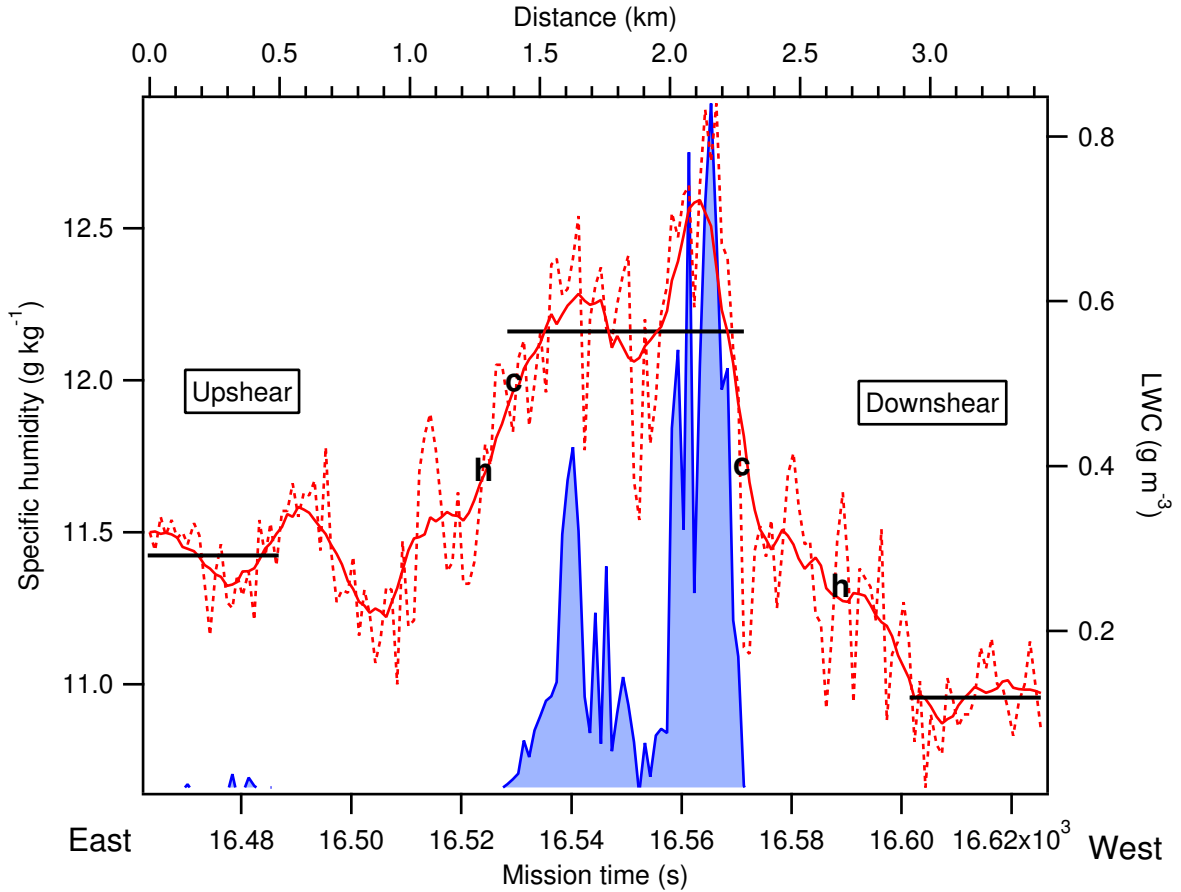


Figure 3.5: Specific humidity ( $\text{g kg}^{-1}$ ) distribution on aircraft traverse 12. The dotted line is the actual data, and the solid line through it are the smoothed data (11-point moving average of the dotted line). The shaded area is the cloud liquid water content ( $\text{g m}^{-3}$ ). The cloud boundary is defined by a liquid water content of  $0.01 \text{ g m}^{-3}$ , and is displayed as “c”, and the edge of the halo is denoted by “h” in the humidity distribution. The horizontal line in the cloud area is the in-cloud specific humidity,  $\bar{q}_{vc}(z)$ , while the two lines outside the cloud are the environmental specific humidity  $\bar{q}_{env}(z)$ . The distance from the beginning of this traverse is given on the top axis.

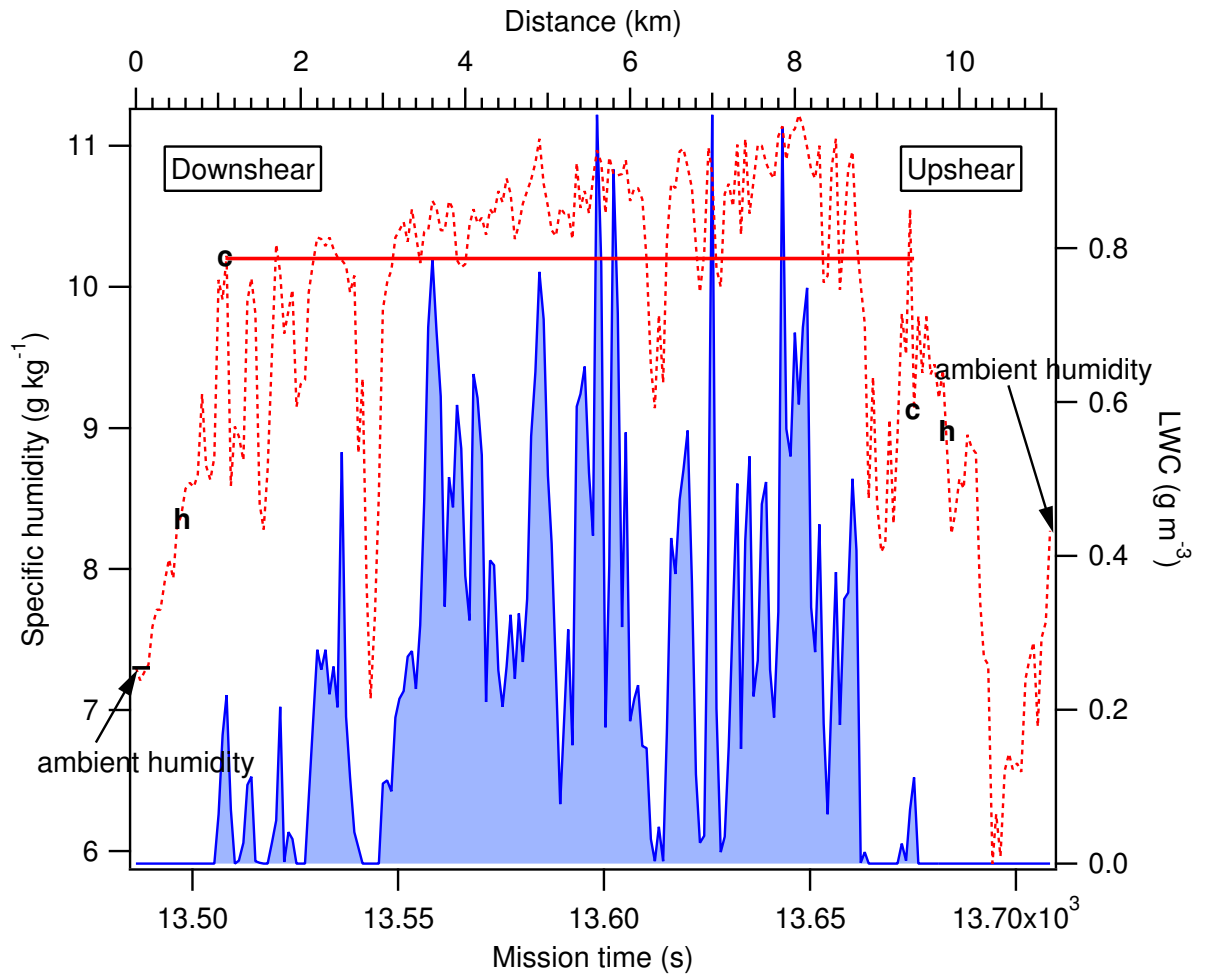


Figure 3.6: Same as Fig. 3.5 but for traverse 4. The ambient specific humidity is defined as that at the start and end of the traverse.

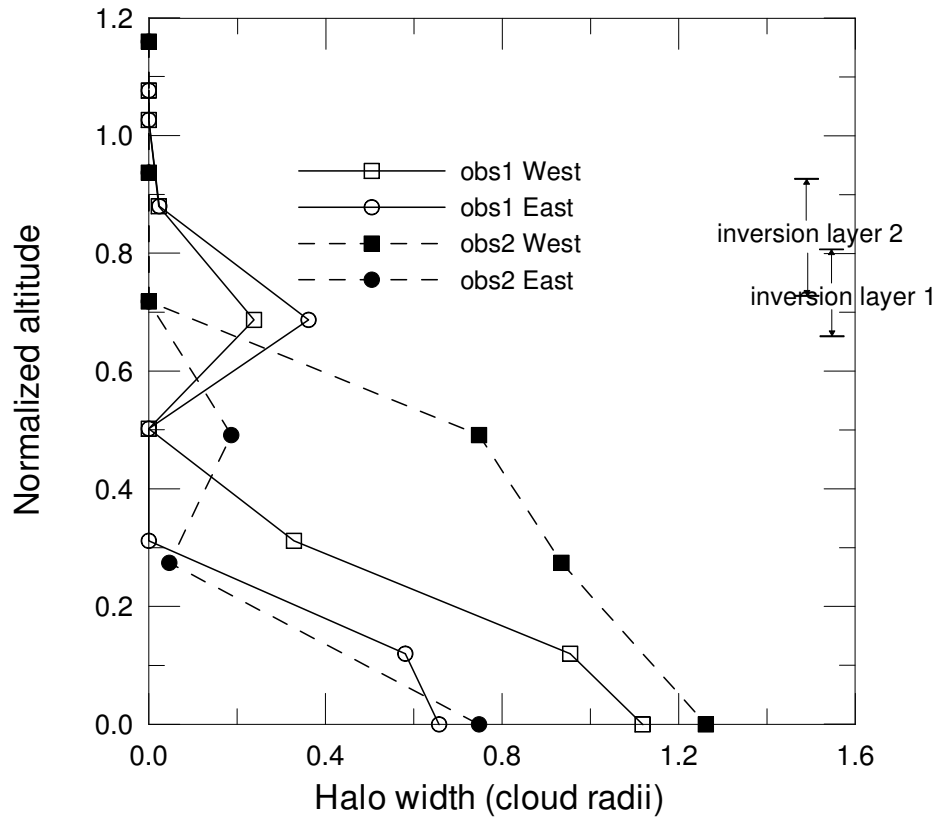


Figure 3.7: Vertical profile of cloud halo width at the west and east sides of the cloud. versus the altitude normalized with the cloud depth for observations 1 and 2. The normalized altitudes of 0 and 1 refer to cloud base and cloud top, respectively. Below the inversion base, the west side relative to the cloud is the downshear direction.

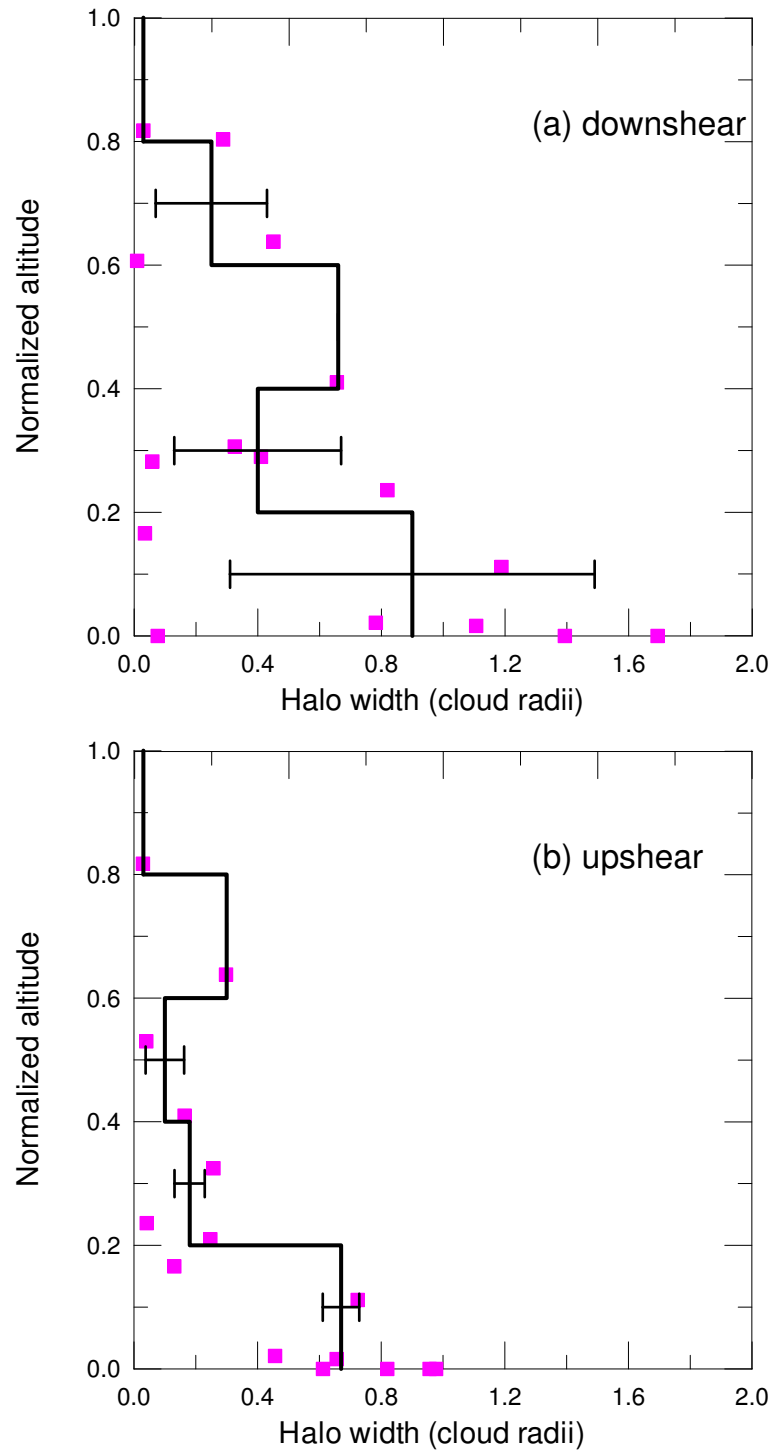


Figure 3.8: Vertical profile of the halo width for the sampled clouds shown in Table 3.2 in the (a) downshear and (b) upshear directions of the cloud. The data points are categorized into five altitude bins. The thick solid line is the averaged halo width of each altitude bin. Error bars indicate the standard deviations of the data points in each altitude bin. The square symbols indicate the observational data points.

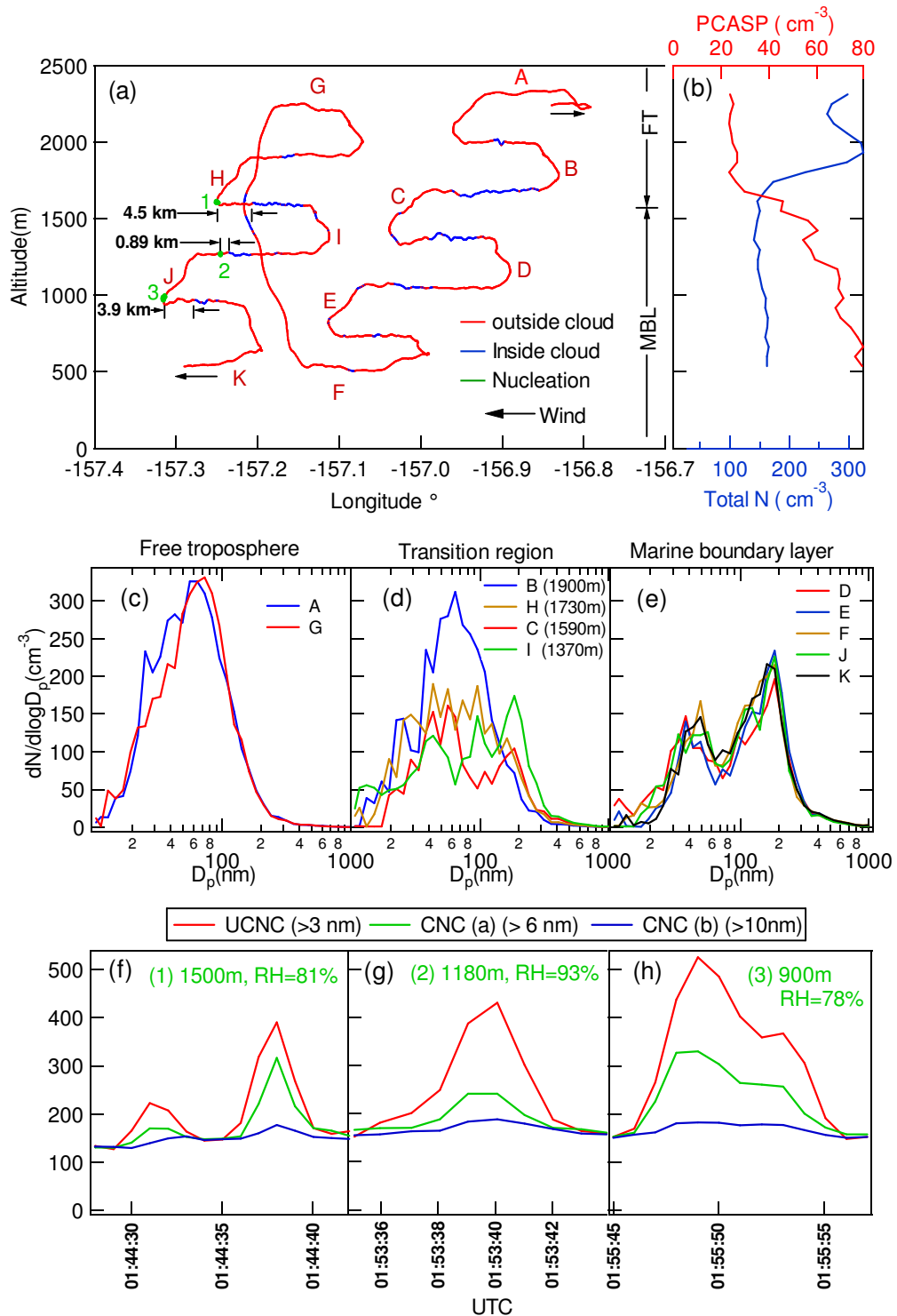


Figure 3.9: (a) Flight track during sampling of a convective cumulus cloud from UTC 00:50 to 02:04 on August 60 2001, with different altitudes labelled A–K; (b) Vertical profile of total particle concentration and particle concentration in the size range, 0.1 to 3.5  $\mu\text{m}$  diameter; (c)–(e) dry aerosol size distributions in free troposphere, transition region, and marine boundary layer; (f)–(g) Particle concentrations measured by three CNCs when newly formed particles were detected.

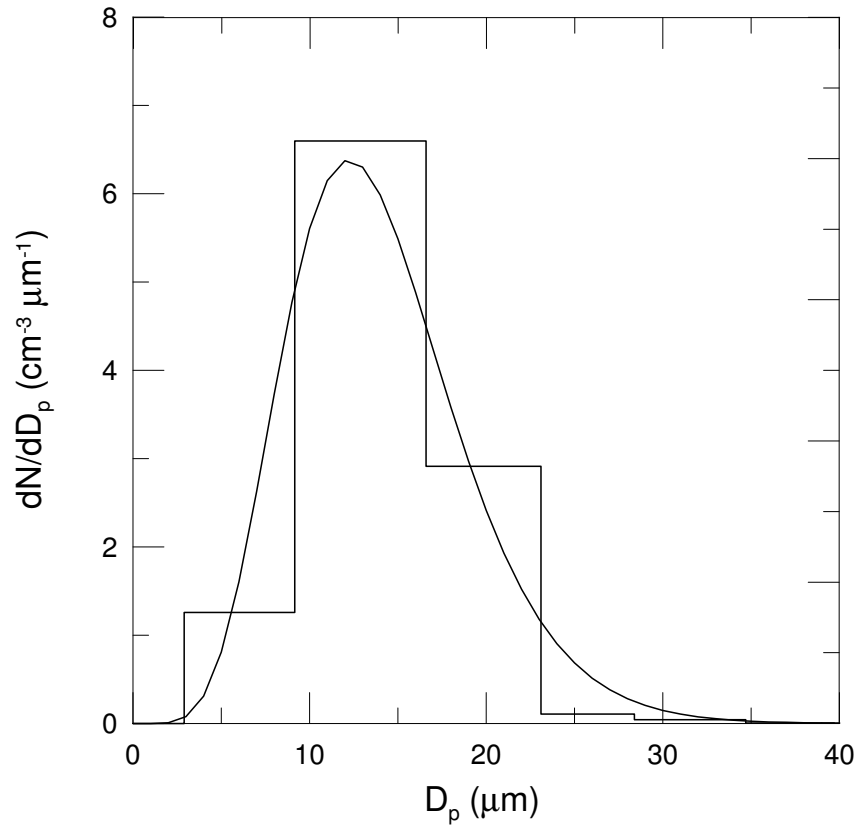


Figure 3.10: Averaged cloud droplet size distribution for traverse 7, together with continuous fitted gamma distribution [Eq. (3.2)] used for simulation.

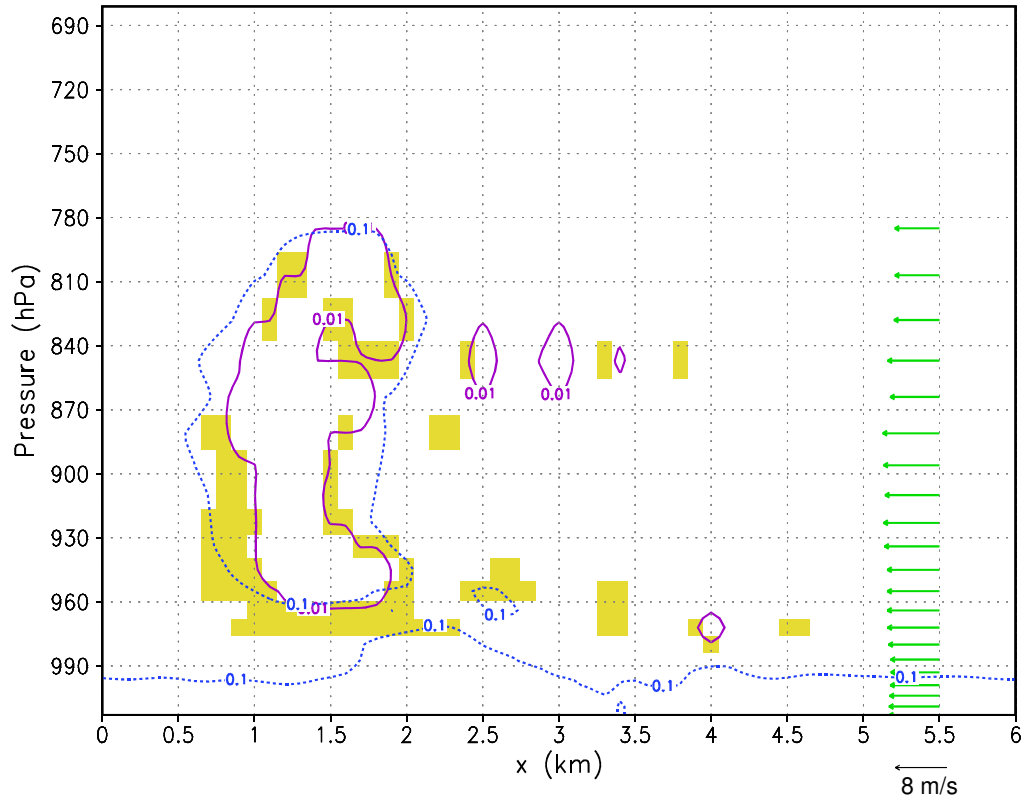


Figure 3.11: Simulated cloud (LWC contour line of  $0.01 \text{ g m}^{-3}$ ) and cloud halo (shaded regions) at  $t = 16$  min. Below the inversion base, the west side of the cloud is the downshear side. The dotted line is the isopleth of turbulent kinetic energy of  $0.1 \text{ m}^2 \text{ s}^{-2}$ . The vertical profile of horizontal wind speed is shown as horizontal arrows.

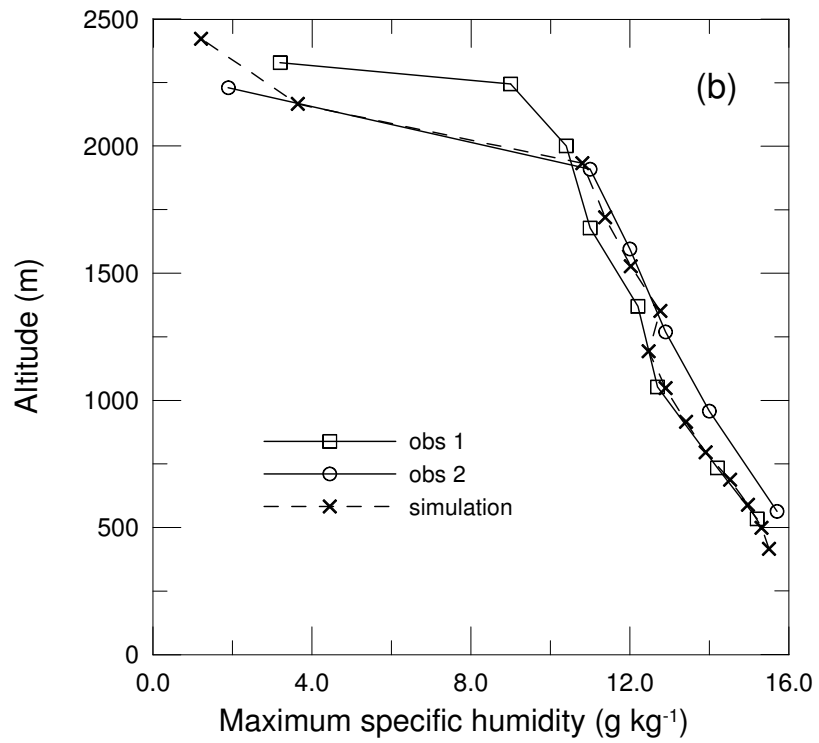
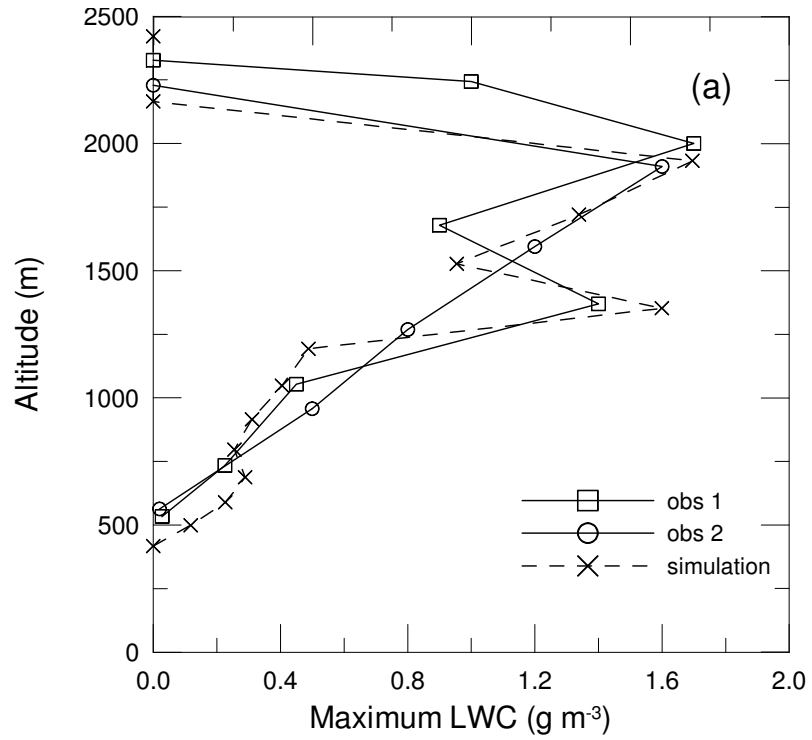


Figure 3.12: Vertical profiles of the maximum (a) LWC and (b) specific humidity from RAMS simulation at  $t = 16$  min, observation 1 and observation 2.

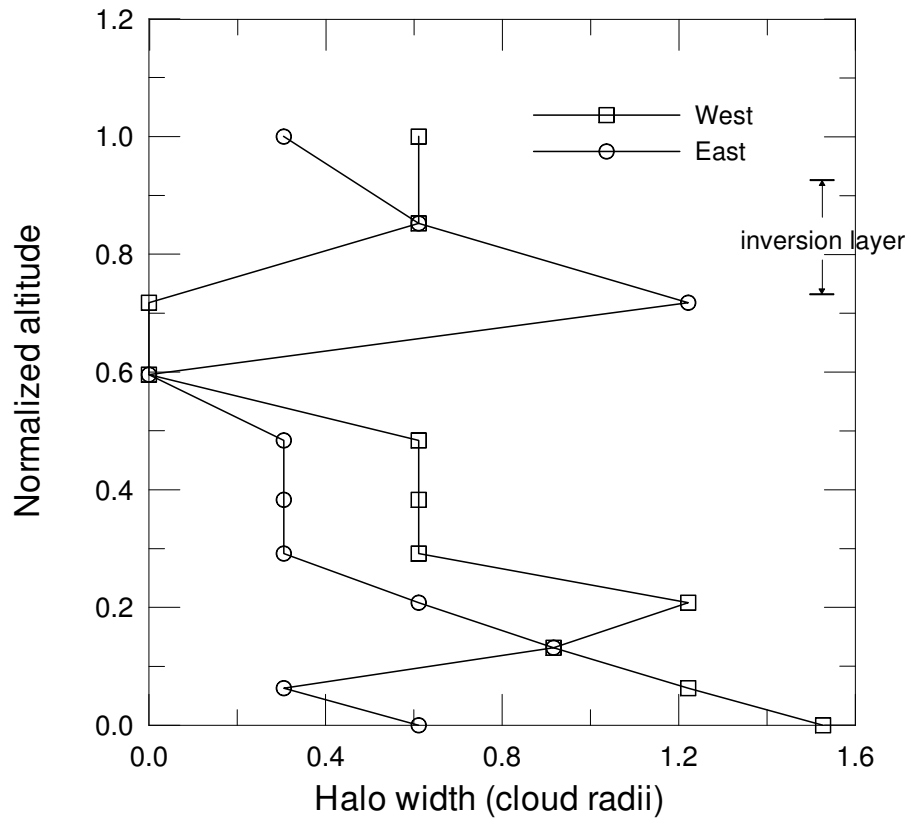


Figure 3.13: Vertical profile of the simulated cloud halo as shown in Fig. 3.11 at the west side and east side of the cloud at  $t = 16$  min. Wind is from the east. Below the inversion base, the west side relative to the cloud is the downshear direction.

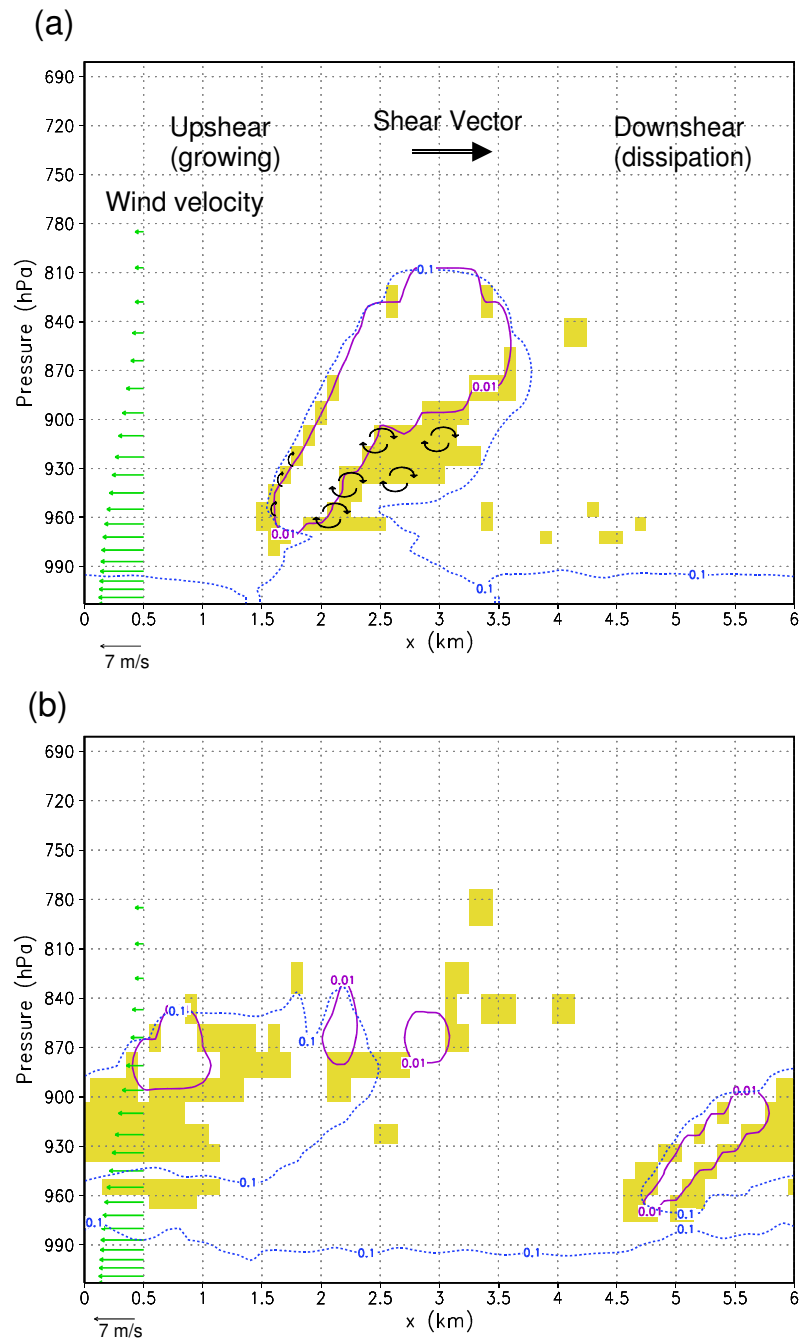


Figure 3.14: Halo (shaded regions) simulation by imposing a stronger wind shear into the simulation as shown in Fig. 3.11 for (a) mature stage and (b) dissipation stage. The turbulent mixing area is encompassed by the isopleth (dotted) of turbulent kinetic energy of  $0.1 \text{ m}^2 \text{ s}^{-2}$ . The vertical profile of horizontal wind speed is shown as horizontal arrows. The LWC contour line (solid) of  $0.01 \text{ g m}^{-3}$  represents the cloud.

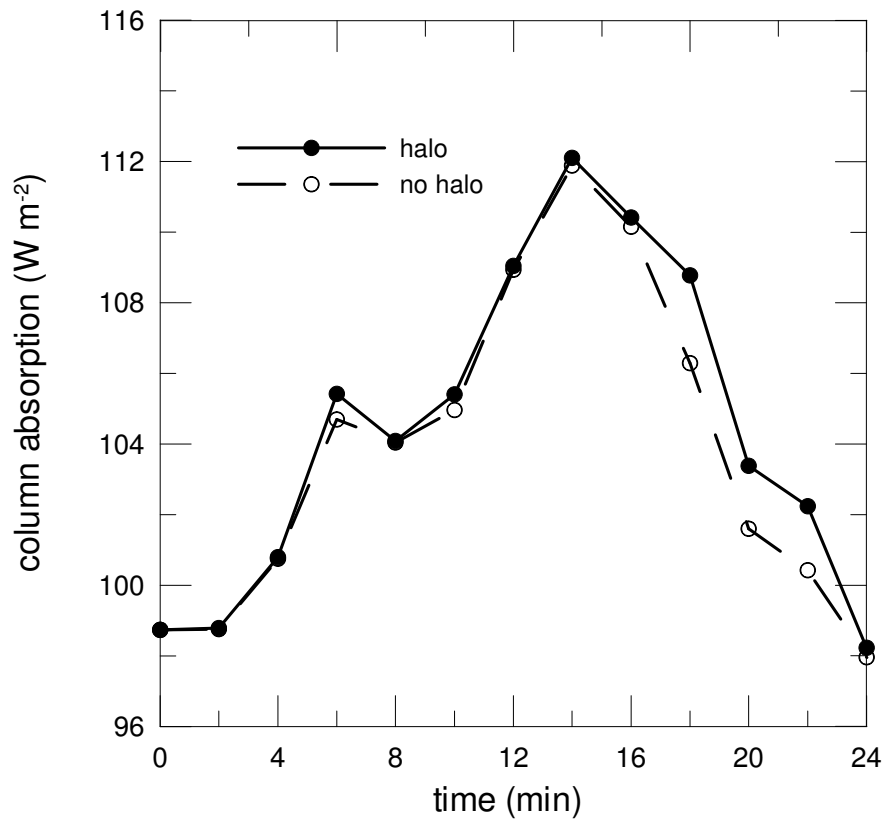


Figure 3.15: Domain-averaged (over the  $x$ -axis) SW atmospheric column (surface to 3.4 km) absorption ( $A$ ) as a function of simulation time in the presence and absence of humidity halo. The dotted line is the halo-enhanced atmospheric absorption ( $\Delta A$ ).

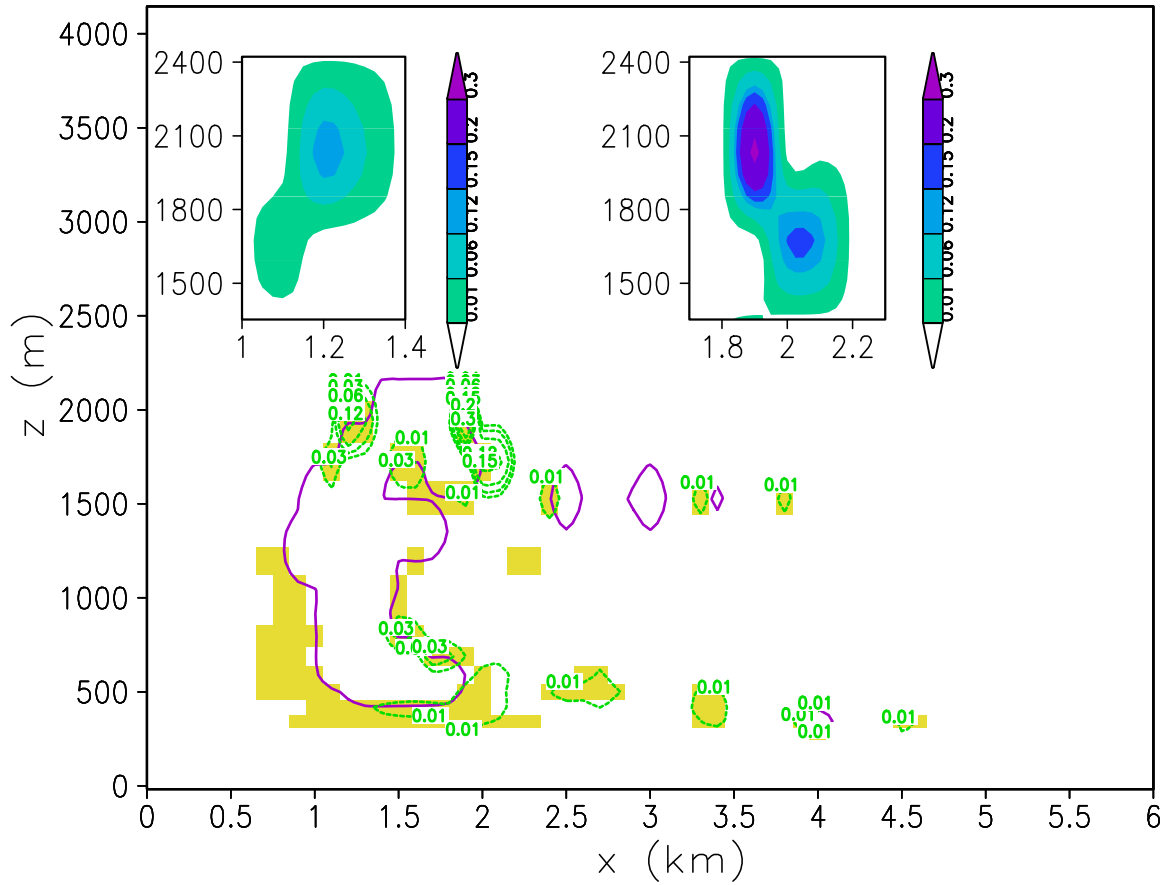


Figure 3.16: Increase of the atmospheric heating rate in the presence of a cloud halo over that in the absence of a halo for the simulation shown in Fig. 3.11. Contour lines (green dashed) are 0.01, 0.03, 0.06, 0.12, 0.15, 0.2, 0.3 K hr<sup>-1</sup>. The LWC contour line (purple solid) of 0.01 g m<sup>-3</sup> is the cloud, and shaded regions (yellow) are the halo. Two shaded contour plots provide an expanded view of the enhanced heating rate near the cloud top.

## Chapter 4

# Study of the aerosol indirect effect by large-eddy simulation of marine stratocumulus

Reference: Lu, M.-L. and J. H. Seinfeld, 2005: Study of the Aerosol Indirect Effect by Large-Eddy Simulation of Marine Stratocumulus. Submitted to *J. Atmos. Sci.*.

### 4.1 Abstract

A total of 98 3D LES simulations of marine stratocumulus clouds covering both nighttime and daytime conditions were performed to explore the response of cloud optical depth ( $\tau$ ) to various aerosol number concentration ( $N_a = 50 - 2500 \text{ cm}^{-3}$ ) and the co-varying meteorological conditions (large-scale divergence rate and SST). The idealized FIRE and the ASTEX Lagrangian 1 sounding profiles were used to represent the lightly and heavily drizzling cases, respectively. The first and second aerosol indirect effects are identified. Through statistical analysis,  $\tau$  is found to be both positively correlated with  $N_a$  and cloud liquid water path (LWP) with a higher correlation associated with LWP, which is predominantly regulated by large-scale subsidence and SST. Clouds with high LWP occur under low SST or weak large-scale subsidence. Introduction of a small amount of giant sea salt

aerosol into the simulation lowers the number of cloud droplets activated, results in larger cloud droplets, and initiates precipitation for non-drizzling polluted clouds or precedes the precipitation process for drizzling clouds. However, giant sea salt aerosol is found to have a negligible effect on  $\tau$  for lightly precipitating cases, while resulting in a relative reduction of  $\tau$  of 3% – 77% (increasing with  $N_a$ , for  $N_a = 1000 - 2500 \text{ cm}^{-3}$ ) for heavily precipitating cases, suggesting the impact of giant sea salt is only important for moist and potentially convective clouds. Finally, a regression analysis of the simulations shows that the second indirect effect is more evident in clean than polluted cases. The second indirect effect is found to enhance (reduce) the overall aerosol indirect effect for heavily (lightly) drizzling clouds, that is  $\tau$  is larger (smaller) for the same relative change in  $N_a$  than considering the Twomey (first indirect) effect alone. The aerosol indirect effect (on  $\tau$ ) is lessened in the daytime afternoon conditions and is dominated by the Twomey effect; however, the effect in the early morning is close but slightly smaller than that in the nocturnal run. Diurnal variations of the aerosol indirect effect should be considered to accurately assess its magnitude.

## 4.2 Introduction

Particles in the atmosphere affect the radiation balance of the Earth by reflecting and absorbing incoming sunlight and by acting as cloud condensation nuclei (CCN). So-called aerosol indirect climate forcing refers to perturbation of the Earth’s radiation balance through modification of cloud albedo and cloud lifetime by anthropogenic aerosols. Uncertainty in the magnitude of indirect aerosol radiative forcing is large; in the 2001 IPCC (Intergovernmental Panel on Climate Change) report (Houghton et al. 2001), global aerosol indirect forcing was estimated to vary from  $-1.1$  to  $-3.7 \text{ W m}^{-2}$ , a range that is comparable,

but opposite in sign, to that of greenhouse gases. Whether such a large negative forcing can be consistent with firmly established greenhouse gas radiative forcing and global observed temperature rise is, in itself, a major question, but the immediate need is to understand in a detailed and specific way the microphysical mechanisms underlying the aerosol indirect effect.

The so-called first indirect, or Twomey, effect refers to the radiative impact of decrease in cloud droplet effective radius that results from increases in aerosol number concentration, assuming a constant liquid water content (Twomey 1977). The second indirect effect refers to a decrease in precipitation efficiency and a resulting increase in cloud liquid water path and lifetime and, hence, albedo as a result the smaller droplet effective radius (Albrecht 1989). Observational evidence for the first indirect effect is substantial and is based on in situ measurements (e.g., ship track studies (Coakley et al. 1987) or airborne observations (Brenquier et al. 2000 and Heymsfield and McFarquhar 2001), satellite retrievals (e.g., Han et al. 1998 and Bréon et al. 2002), and surface remote sensing measurements (Feingold et al. 2003; Kim et al. 2003; Penner et al. 2004). Observational evidence for precipitation suppression exists in biomass burning smoke (Rosenfeld 1999; Rosenfeld et al. 2002; Andreae et al. 2004; Koren et al. 2004), urban and industrial air pollution (Rosenfeld 2000), and desert dust (Rosenfeld et al. 2001).

Ultimately, prediction of the global indirect aerosol effect requires a general circulation model (GCM) with an explicit link between aerosol properties (size, number, and composition) and cloud properties. This will involve the development of appropriate aerosol-cloud parameterizations (see, for example, Ghan et al. 1997, Abdul-Razzak and Ghan 2000, and Nenes and Seinfeld 2003). To unravel the intricate mechanisms by which perturbations in aerosol properties lead to perturbations in cloud properties, mechanisms that must be

represented in parameterizations, it is necessary to perform individual cloud simulations at a high level of detail.

Stratocumuli have been identified as having a potentially significant impact on climate. Satellite imagery shows that marine stratiform clouds reflect much more sunlight (albedo  $\sim 30\text{-}40\%$ ; Randall et al. 1984) than the darker underlying ocean surface (albedo  $\sim 10\%$ ) and strongly enhance the Earth's global albedo. They also radiate in the long-wave at approximately the same temperature as the ocean surface. Moreover, they occur with high frequency and have extensive spatial coverage with annually averaged cloud cover of approximately 34% (Warren et al. 1986). It has been estimated that the global cooling that would result from a 4% increase in the area covered by marine stratocumulus would offset the expected warming from doubling the atmospheric concentration of  $\text{CO}_2$  from the preindustrial period (Randall et al. 1984).

The responses of clouds to regional-scale variations in CCN are invariably subject to co-varying meteorological conditions, causing the cloud microphysical response to occur together with changes from purely dynamical forcing. For example, satellite identification of the aerosol indirect effect is usually confounded by the strong dependence of cloud albedo on the cloud liquid water path (Schwartz et al. 2002). Through a six SCM (single column model) comparison study, Menon et al. (2003) found that cloud optical depth alone is not indicative of the effect of CCN variations because of the LWP variability associated with different meteorological conditions. Therefore, the ability to characterize the changes in LWP resulting from dynamical forcing variables, such as large-scale subsidence and sea surface temperature, and the link to the cloud optical properties, is needed. Large Eddy Simulation (LES) studies of the aerosol indirect effect have generally been limited by the computation time required for 3D LES; some have employed a 2D version (e.g., Feingold

et al. 1994, 1997, 1999b; Jiang et al. 2002), while others have performed 3D simulations (Feingold et al. 1999b and Ackerman et al. 2003).

The goal of the present paper is to computationally investigate the indirect effect using LES for two reasonably well-studied marine stratocumulus cases. One of the key issues that has arisen from previous studies is that purely dynamical factors may exert an effect on cloud optical depth and cloud fraction as large as or even greater than that exerted by varying microphysical properties. We therefore study the effect on cloud optical depth resulting from variations both in aerosol number concentration and key dynamical variables, as embodied by the large-scale divergence rate and the sea surface temperature. Because several previous studies have noted the particular effect of giant sea salt as a CCN, when occurring together with pollution aerosols, we also consider the effect of giant sea salt aerosol on the cloud optical depth. The overall study is based on a series of 98 3D LES simulations. For the cases considered, we are able to generate statistical correlations between cloud optical depth, liquid water path, aerosol number concentration, subsidence rate, and sea surface temperature. The correlations are useful in quantifying the results of the LES simulations in separating dynamical effects from microphysical effects.

## 4.3 Model setup

### 4.3.1 Numerical model

In this study, we employ the three-dimensional, nonhydrostatic version of RAMS (Regional Atmospheric Modeling System)(Pielke et al. 1992 and Walko et al. 1995). The predicted variables include the three velocity components, the Exner function (the pressure variable), the ice-liquid water potential temperature (Tripoli and Cotton 1981), and the

total water mixing ratio. The radiation scheme is that of Chen and Cotton (1983), which parameterizes the long- and short-wave radiative flux divergences using the mixed emissivity approach. The LES implementation uses a subgrid scheme adapted from Deardorff (1970), predicting the turbulent kinetic energy in order to evaluate eddy mixing coefficients.

The simulation uses the explicit bin-resolving warm cloud microphysics model (Tzivion et al. 1987, 1989; Feingold et al. 1994; Stevens et al. 1996a), which follows the moment-conserving techniques described by Tzivion et al. (1987, 1989). This microphysical model predicts for both number and mass concentration of drops in each of 36 size bins. The drop size bins are specified as mass doubling, spanning the radius size spectrum of  $1.56 \mu\text{m} - 0.64 \text{ cm}$ . The microphysical processes of drop condensation/evaporation, stochastic collision-coalescence, sedimentation, and aerosol activation are considered in the simulation. The RAMS-bin microphysics model has been applied in numerical studies of Arctic boundary layer cloud from the FIRE/SHEBA (Jiang et al. 2001), the entrainment of free tropospheric aerosols into the marine boundary layer (Jiang et al. 2002), stratocumulus clouds with the FIRE or ASTEX sounding profiles (Feingold et al. 1994; Stevens et al. 1996a, 1998), and stratocumulus coupled with the aqueous chemistry (Feingold and Kreidenweis 2002).

### **4.3.2 Aerosol activation scheme**

#### **4.3.2.1 Single mode aerosol**

In the basic droplet activation scheme implemented in the RAMS model the aerosols are assumed to have a constant size distribution in space and time; cloud droplet activation is calculated such that the number of cloud drops is based on the model-derived supersaturation but not exceeding the number concentration of aerosol. The supersaturation is prognosed in the model by the semianalytic method of solving the semi-Lagrangian con-

densation/evaporation equations derived in Tzivion et al. (1989), described in more detail by Stevens et al. (1996a). Although the Eulerian model has been known to suffer from the spurious production of cloud-top supersaturations leading to the spurious production of cloud droplets at cloud-top (Stevens et al. 1996b), we have not found an immediate and practical solution for this numerical artifact. For our sensitivity studies of varying the CCN number concentrations, this numerical artifact does not impose a significant effect on our conclusions.

The normalized aerosol size spectrum,  $f(a; a_g, \sigma_g)$ , is assumed to be log-normal,

$$f(a; a_g, \sigma_g) = \frac{1}{\sqrt{2\pi} a \ln \sigma_g} \exp\left(-\frac{\ln^2 \frac{a}{a_g}}{2 \ln^2 \sigma_g}\right) \quad (4.1)$$

where  $a$  is the aerosol radius, and  $a_g$  and  $\sigma_g$  are the median radius and the geometric standard deviation of the spectrum, respectively. The characteristics of the aerosol size distribution can be varied through the parameters  $a_g$  and  $\sigma_g$ . The number of activated drops at any time is estimated by the difference between the number of particles that would activate at the ambient supersaturation and the number of existing drops. Therefore, at each time step the drop concentration in the smallest size interval is incremented by an amount

$$\Delta N_c = \max\left[0, N_a \int_{a_{cut}}^{\infty} f(a; a_g, \sigma_g) da - N_c\right] \quad (4.2)$$

where  $N_a$  is the total aerosol concentration,  $a_{cut}$  is the dry radius of the smallest particle activated at the ambient supersaturation  $S$  (calculated by the model), and  $N_c$  is the number concentration of cloud droplets in the previous time step. The integral in Eq. (4.2) is the potential fraction of activated particles, which can be obtained by integrating the log-normal

size distribution (Von der Emde and Wacker 1993),

$$\int_{a_{cut}}^{\infty} f(a; a_g, \sigma_g) da = \frac{1}{2} [1 - \text{erf}(u)]$$

where  $u = \ln(a_{cut}/a_g)/\sqrt{2} \ln \sigma_g$ . The activation radius  $a_{cut}$  can be calculated based on the Köhler equation (Seinfeld and Pandis 1998)

$$a_{cut} = \left( \frac{4A^3 \rho_w M_s}{27\nu (\ln S)^2 \rho_s M_w} \right)^{\frac{1}{3}} \quad (4.3)$$

where  $M_s$  and  $M_w$  are the molecular weight of the solute and pure water, respectively;  $\nu$  is the number of ions the salt dissociates into (von't Hoff factor for solute in solution),  $\rho_s$  and  $\rho_w$  are the density of the aerosol material and water, respectively;  $A$  is the coefficient of the curvature effect given by,  $A = 2M_w \sigma_w / RT \rho_w$ , where  $R$  is the molar gas constant,  $T$  is the temperature, and  $\sigma_w$  is the surface tension of water. The chemical characteristics of the CCN affect  $a_{cut}$ .

#### 4.3.2.2 Multimode aerosols

One can extend the above single-mode aerosol activation to multiple externally mixed log-normal modes, each mode composed of a soluble material following the derivation of Abdul-Razzak and Ghan (2000). This multimode log-normal distribution is expressed as

$$f_i(a; a_{g,i}, \sigma_{g,i}) = \frac{1}{\sqrt{2\pi} a \ln \sigma_{g,i}} \exp \left( -\frac{\ln^2 \frac{a}{a_{g,i}}}{2 \ln^2 \sigma_{g,i}} \right) \quad (4.4)$$

where  $a_{g,i}$  is the geometric mean dry radius, and  $\sigma_{g,i}$  is the geometric standard deviation for each aerosol mode  $i$ ,  $i = 1, 2, \dots, I$ .

The smallest activation size for each mode  $i$  is,

$$a_{cut,i} = a_{g,i} \left( \frac{S_{m,i}}{S} \right) \quad (4.5)$$

where  $S_{m,i}$  is given by

$$S_{m,i} = \frac{2}{\sqrt{B_i}} \left( \frac{A}{3a_{g,i}} \right)^{\frac{3}{2}} \quad (4.6)$$

and the hygroscopicity parameter (solute effect)  $B$  of aerosol mode  $i$  can be expressed as (Pruppacher and Klett 1997),

$$B_i = \frac{M_w q_i \nu_i \phi_i \epsilon_i / M_{s,i}}{\rho_w q_i / \rho_{s,i}} \quad (4.7)$$

where  $q_i$  is the mass mixing ratio of mode  $i$ ,  $\phi_i$  is the osmotic coefficient, and  $\epsilon_i$  is the mass fraction of soluble material. Therefore, the number of particles activated at each time step for this multimode aerosol distribution is

$$\Delta N_c = \max \left[ 0, \sum_{i=1}^I N_{a,i} \int_{a_{cut,i}}^{\infty} f_i(a; a_{g,i}, \sigma_{g,i}) da - N_c \right] \quad (4.8)$$

## 4.4 LES simulation

### 4.4.1 Case description

We consider the intercomparison model study of a stratocumulus-topped planetary boundary layer of the GCSS (Global Energy and Water Cycle Experiment Cloud System Study) Boundary-Layer cloud Working Group 1 (Moeng et al. 1996). The sounding profile is loosely based on the FIRE [First ISCCP (International Satellite Cloud Climatology Project) Regional Experiment] of the 7 July 1987 horizontally homogeneous and nearly

solid cloud deck reported in Betts and Boers (1990). The simulation is an idealized nighttime stratocumulus-topped MBL case, and there is little wind shear and surface heating. The cloudy MBL is driven mainly by cloud-top IR cooling and modified by entrainment and condensation/evaporation processes. This sounding profile and configuration have been used in several previous studies, e.g., Feingold et al. (1994, 1996) and Stevens et al. (1996a).

The model was set up with sea surface temperature as 288 K. The large-scale subsidence is prescribed by  $w_{sub} = -Dz$ , where the large-scale divergence  $D = 5 \times 10^{-6} \text{ s}^{-1}$ . The subsidence velocity ( $w_{sub}$ ) is applied to the scalar tendency terms similar to Krueger (1988). The roughness length is 0.0002 m. The initial wind field was set to equal to the geostrophic wind, set to be  $2 \text{ m s}^{-1}$  in the  $x$ -direction and  $-4 \text{ m s}^{-1}$  in the  $y$ -direction. The initial sounding profile of potential temperature  $\theta$  and total liquid water mixing ratio ( $q_T$ ,  $q_T = q_v + q_l$ , where subscripts  $v$  and  $l$  represent vapor and liquid, respectively) are given in Fig. 4.1. Only long-wave radiation is considered for this nocturnal case. The radiative cooling rate is updated every 10 s in the simulation. The grid resolution is 55 m in  $x$  and  $y$  and 25 m in  $z$ . The numerical time step used is 2 s. White noise with amplitude of 0.1 K was applied on the temperature field at the lowest level. In order to accommodate the 98 3D simulations (Table 4.1), we reduced the computation domain down to  $1.1 \text{ km} \times 1.1 \text{ km}$  in the horizontal. We had chosen the BASE case (described subsequently) to validate the use of the smaller domain against the  $3.3 \text{ km} \times 3.3 \text{ km}$  domain (BASELG) used in Moeng et al. (1996). Figure 4.2 demonstrates that the trend of simulated domain averaged cloud optical depth (and also cloud albedo, not shown) versus aerosol number concentration is similar for both domain sizes, and the differences of actual values are small. The difference between the small domain results over the large domain results, averaged over the six CCNs, is 5.2%, slightly smaller than the averaged data standard deviation (i.e., the error bar in

the figure). Since our purpose is to investigate the relative change of the spatially and temporally averaged variables due to other external parameters, e.g., SST, Fig. 4.2 suggests that the use of the smaller domain is sufficient for our purpose. We return to Fig. 4.2 subsequently to discuss the effect of varying  $N_a$ . The vertical domain is 1.2 km, the same as that used in Moeng et al. (1996). Each simulation was run for six hours and requires about 2 hours to establish a well-mixed stratocumulus and resolved-scale boundary layer turbulence. Therefore, predictions for the final three hours are used in evaluating the FIRE simulations.

A constant background completely soluble ammonium sulfate aerosol with log-normal distribution mean radius  $r_g = 0.0695 \mu\text{m}$  and  $\sigma_g = 2.03$  (d’Almeida et al. 1991) is used. The aerosol density is  $1.77 \text{ g m}^{-3}$ , the aerosol molecular weight is  $132.14 \text{ g mol}^{-1}$  (Abdul-Razzak et al. 1998), and we assume complete dissociation  $\nu = 3$ . The aerosol number concentration,  $N_a$ , is set at six different levels, 50, 100, 500, 1000, 1500, and  $2000 \text{ cm}^{-3}$ , to represent increasing anthropogenic pollution loadings. The above configurations are considered to be the base run (referred to as “BASE”, hereafter). Aerosol number concentrations of  $N_a = 50$  and  $100 \text{ cm}^{-3}$  are referred to as “clean” cases and those with  $N_a \geq 500 \text{ cm}^{-3}$  are referred to as “polluted” cases. We do not, in this study, consider aerosol “chemical effects” on cloud droplet activation. Such effects have been addressed in the context of adiabatic parcel models (Nenes et al. 2002).

#### 4.4.2 Meteorological conditions

Stratocumulus clouds generally lie to the east of the subtropical high pressure and their cloud depths, cloudiness, and marine boundary layer circulations are closely related to the meteorological conditions (e.g., Schubert et al. 1979a,b; Wakefield and Schubert 1981;

Krueger et al. 1995; Wyant et al. 1997). The numerical study of a cloud-topped mixed-layer model by Schubert et al. (1979b) showed that the adjustment time under the downstream varying meteorological conditions for steady-state solution of cloud top is long (several days, especially for adjustment to large-scale divergence). The computation utilizing LES for Lagrangian numerical simulations of the subtropical marine boundary layer over the possible range of values of SST and large-scale divergence is inevitably too extensive. Therefore, we perform several sensitivity experiments by slightly varying the cloud LWP through initially changing the SST and large-scale divergence.

We consider two cases — SST2 (2K warmer than the base run) and SST4 (302 K) in addition to the base run (288 K), to study the effect of warmer SST. The initial boundary layer  $\theta$  is adjusted in each case to be the constant value of the warmer SST, while the free tropospheric temperature remains the same as in BASE (Fig. 4.1). Meanwhile, the initial profile of  $q_T$  should also be adjusted to the corresponding increase of SST. The climatological RH of the atmospheric boundary layer over tropical (trade-wind or ITCZ) oceans has been observed to remain in a narrow range around 80% (Fitzjarrald and Garstang 1981). The vertical profile of  $q_T$  is adjusted to be the same RH value as that in the BASE run, and the  $q_T$  profile in the free troposphere is the same as in the BASE run.

The large scale divergence rate is not readily obtainable through regular observation; one tends to rely on values derived from numerical weather prediction models like NCEP and ECMWF. A large scale divergence rate of  $4.0 \times 10^{-6} \text{ s}^{-1}$  was measured in ASTEX (Atlantic Stratocumulus Transition Experiment) with 20% uncertainty (Ciesielski et al. 1999). The value of the rate used in stratocumulus simulations typically lies in the range of  $3 - 5 \times 10^{-6} \text{ s}^{-1}$  (Wakefield and Schubert 1981; Moeng et al. 1996; Wyant et al. 1997); however, a value exceeding  $10 \times 10^{-6} \text{ s}^{-1}$  was used for the European cloud model intercomparison

in order to obtain a realistic cloud top height evolution (Duynkerke et al. 1999 and Chlond and Wolkau 2000). The base value of divergence rate (Table 4.1) is chosen here as  $5 \times 10^{-6} \text{ s}^{-1}$ . Other values used are  $2 \times 10^{-6} \text{ s}^{-1}$  (DIV2),  $6 \times 10^{-6} \text{ s}^{-1}$  (DIV6), and  $10 \times 10^{-6} \text{ s}^{-1}$  (DIV10).

## 4.5 Results

### 4.5.1 Liquid water path (LWP)

Averaged cloud LWP as a function of aerosol number concentration for various values of divergence rate and SST is shown in Fig. 4.3. Simulation results presented in this figure are temporally averaged over the final three hours and spatially over the cloudy region within the domain. Cloud LWP is calculated by the integration of the liquid water content (LWC) over the depth of the cloud,

$$\text{LWP} = \int_{z_b}^{z_t} \text{LWC}(z) dz = \int_{z_b}^{z_t} \int_{r_l}^{r_u} \frac{4}{3} \pi \rho_w r^3 n(r) dr dz \quad (4.9)$$

where  $z_b$  is cloud base and  $z_t$  is cloud top;  $r_l$  and  $r_u$  are the lower and upper radius of the hydrometeor number distribution,  $n(r)$ , respectively.

Cloud LWP varies only slightly with aerosol concentration, particularly at high aerosol loadings. There is a slight decrease of LWP as  $N_a$  increases from  $50 \text{ cm}^{-3}$  to  $500 \text{ cm}^{-3}$  in each of the cases. The effect of high pollution loadings in suppressing drizzle formation (Albrecht 1989) is evidenced as precipitation disappears when  $N_a$  exceeds  $500 \text{ cm}^{-3}$  (Fig. 4.4c). Also, the cloud droplet effective radius (averaged over the upper one-third of the cloud depth, Fig. 4.4b),  $r_e = \int_{r_l}^{r_u} r^3 n(r) dr / \int_{r_l}^{r_u} r^2 n(r) dr$  (a measure of the droplet size that contributes most strongly to the radiance, Hansen and Travis 1974), for  $N_a = 50$  and

$100 \text{ cm}^{-3}$  is larger than the  $15 \text{ }\mu\text{m}$  mean cloud droplet diameter (equivalent to an effective radius of about  $8.5 \text{ }\mu\text{m}$ ) generally considered to be required for the onset of precipitation (Yum and Hudson 2002). However, the precipitation is weak for the FIRE case. Vertical profile of the sedimentation flux (Fig. 4.5) ( $F_{sed} = \rho_0 L \int_{r_l}^{r_u} v_t(r) q_l(r) dr$ , where  $v_t$  is the droplet terminal velocity,  $L = 2.5 \times 10^6 \text{ J kg}^{-1}$ , and  $\rho_0$  is the air density.) shows a similar trend with that of LWC — They both peak at the same height, and the sedimentation flux drops quickly close to zero below the cloud base. Therefore, sedimentation flux is not dominated by the drizzle drops and very little surface precipitation is produced (Fig. 4.4c). This trend of the higher LWP for smaller  $N_a$  could be due to the weak precipitation effect on the stratocumulus-topped MBL dynamics. The study of the detailed dynamical responses of strong precipitation for the stratocumulus by Stevens et al. (1998) concluded that the cloud top entrainment rate and the boundary layer turbulence are decreased due to precipitation and they further hypothesized that light drizzle might lessen the cloud top entrainment drying and result in a deeper boundary layer. Ground-based observations during the ASTEX (Feingold et al. 1999a) also showed that drizzling cases were characterized by the smaller in-cloud turbulence than the non-drizzling cases. Fig. 4.6a is the vertical profile of the resolved-scale  $\overline{w'w'}$  (Fig. 4.6a) for one case each of the clean drizzling clouds ( $N_a = 50 \text{ cm}^{-3}$ ) and non-drizzling clouds ( $N_a = 2000 \text{ cm}^{-3}$ ), respectively.  $\overline{w'w'}$  is the horizontally averaged vertical velocity variance, which is a measure of the turbulence activity. It shows that boundary turbulent motion is weaker for the drizzling cloud than the non-drizzling cloud, in agreement with previously mentioned studies. Therefore the result shows that drizzle formation in the cloud releases latent heat, which partially compensates for the cloud-top long-wave cooling, stabilizes the subcloud atmosphere by evaporation, lessens the boundary layer turbulence, and reduces the cloud-top entrainment drying. We

calculate the entrainment rate,  $E$ , based on the mixing layer model (Lilly 1968), such that  $E = \frac{dh}{dt} + Dh$ .  $h$  is the temperature inversion base, which can be approximated by the horizontal mean cloud top (Moeng et al. 1999). From the above equation,  $E = 0.64 \text{ cm s}^{-1}$  and  $0.66 \text{ cm s}^{-1}$  (averaged over the last five hours) for  $N_a = 50 \text{ cm}^{-3}$  and  $N_a = 2000 \text{ cm}^{-3}$ , respectively. Therefore, the simulation shows a small reduction of cloud-top entrainment drying effect for the clean clouds. Meanwhile, the evaporation of those drizzle fall below the cloud base can moisten and cool the subcloud layer as shown in Fig. 4.6b and Fig. 4.6c. It follows that the cloud lifting condensation level lowers. Considering these two dynamical responses, the result shows cloud LWP is slightly higher for the clean clouds (Fig. 4.6d), in contrast to the typical secondary aerosol effect (e.g., Albrecht (1989)). This decreasing LWP with increasing pollution level is not limited to our simulation.

Brenguier et al. (2003), through ACE-2 (North Atlantic Regional Aerosol Characterization Experiment) measurements over the Atlantic, found that polluted clouds tended to be thinner than clean clouds. Twohy et al. (2005) found a weak anti-correlation between cloud geometrical thickness/cloud LWP and particle concentration from three of the four cleanest cloud cases from DYCOMS-II (Dynamics and Chemistry of Marine Stratocumulus-II), an airborne measurement of stratocumulus clouds over the eastern Pacific Ocean off the coast of San Diego, California. These in-situ aircraft field measurements also support our simulation results of a weak decreasing LWP with increasing aerosol number.

As the large-scale divergence rate increases (DIV2, BASE, DIV6, and DIV10), the cloud top is slowly driven down, thinning the cloud depth, and therefore cloud LWP decreases (Fig. 4.3). Cloud LWP decreases with increasing SST. The fractional cloudiness, averaged over the final 3 h and over six  $N_a$  cases, for BASE and SST2 are both approximately 1, but it decreases to roughly 0.4 for SST4. This behavior is similar to the stratocumulus to

trade cumulus transition when air advects from the subtropical regime over warmer ocean (Albrecht et al. 1995 and Wyant et al. 1997). Conditions becomes less cloudy because of gradual dissipation of the overlying stratocumulus clouds. Results in Fig. 4.7 at simulation  $t = 6$  h show that cloud base (top) height increases from 507 m (812 m) for BASE to 641 m (836 m) for SST4. This behavior agrees with both observations and simulations (e.g., Schubert et al. 1979a; Krueger et al. 1995; Wyant et al. 1997) that the stratocumulus topped boundary layer deepens and cloud base rises with warmer SST. Long-wave cooling at the cloud top drives the turbulent mixing through the entire boundary layer and maintains the layer in a well-mixed state. In the SST4 simulation (Fig. 4.7c), the initially broken cloud progressively forms a homogeneous solid deck due to longwave radiative cooling of the cloud top, gradually producing a well-mixed boundary layer.

Because of the fracture cloud fields seen in the early hours of SST4, we also carry out the same simulation but in the larger  $3.3 \text{ km} \times 3.3 \text{ km}$  horizontal domain (SST4LG). Results show that cloudiness for clean clouds of SST4LG are about 0.4 smaller than 0.7 of SST4, but they are comparable for polluted clouds. The averaged LWP and cloud optical depth (see next paragraph) and their trends with  $N_a$  of SST4LG are roughly close to those of SST4 (Figs. 4.3 and 4.8) suggesting the use of LWP and cloud optical depth of SST4 for subsequent analysis is appropriate.

#### 4.5.2 Cloud optical depth

Cloud optical depth is determined by,

$$\tau = \int_{z_b}^{z_t} \int_{r_l}^{r_u} 2\pi r^2 n(r) dr dz \quad (4.10)$$

where the extinction efficiency becomes asymptotically approaching a value of 2 for cloud droplets at visible wavelength (Seinfeld and Pandis 1998). Figure 4.8 shows Cloud optical depth increases with increasing aerosol burden. The trend of cloud optical depth versus aerosol number concentration is very similar to that of  $\tau$  versus  $N_a$  (Fig. 4.4f), where the cloud albedo is calculated in each column by  $Albedo = (1 - g)\tau / (2 + (1 - g)\tau)$  (Bohren 1980), and  $g$  is the asymmetry factor ( $\approx 0.85$ ). Because the averaged cloud optical depth is more sensitive to the aerosol number concentration than is LWP (Fig. 4.3), change of cloud optical depth with  $N_a$ , the Twomey effect, is clearly evident for all simulations except for SST4, in which the LWP itself is small.

In order to examine the relationship between  $\tau$  and LWP, we re-plot each data point in Figs. 4.3 and 4.8 in  $\tau$ -LWP (Fig. 4.9). Low LWP, and hence thinner cloud, is on the left hand side of Fig. 4.9 corresponding to higher SST or stronger divergence, while high LWP and thicker cloud conditions are on the right hand side, corresponding to lower SST or weaker large-scale subsidence. Cloud optical depth is highly positively correlated with LWP. This is consistent with satellite measurements of strong dependence of cloud albedo on LWP (Schwartz et al. 2002). Cloud optical depth is dependent on both LWP (or  $H$ ) and  $N_a$  as corroborated observationally (Breguier et al. 2000). For the same cloud optical depth, a clean cloud has higher  $H$  than a polluted cloud, as also seen in aircraft in situ measurements of clouds (i.e., refer to Fig. 2 of Breguier et al. (2000) at constant  $\tau$  line). Figure 4.9 also illustrates that the Twomey effect as seen by comparing  $\tau$  for polluted and clean clouds at constant LWP. The change of cloud optical depth per increase of cloud droplet number concentration (i.e.,  $\frac{d\tau}{d \ln N_c}$  at constant LWP) is larger for thicker cloud; in the present simulations, they are a solid stratocumulus deck with lower SST or lower divergence.

We also overlay the figure with the constant- $r_e$  lines, derived from Stephens (1978) based on a spatially uniform cloud with monodisperse cloud droplets,

$$r_e = 1.5\text{LWP}/\tau \quad (4.11)$$

The simulated  $r_e$  is averaged over the upper one-third of the cloud because the cloud radiative properties are mainly determined from their values near the cloud top. The simulated  $r_e$  in general is close to the theoretical lines, but the large deviation appears for SST4 due to spatially inhomogeneous cloud morphology for this experiment. It can be identified clearly from the figure that the data points can be grouped into polluted and clean cases based on  $r_e$ . The slopes (i.e., 0.27 and 0.13) are inversely proportional to the  $r_e$ , which is also explained by Eq. (4.11)

A multiple regression of cloud optical depth as a function of  $N_a$  and LWP data points, horizontal averages sampled every 5 min during the final 3 hours for the six weakly drizzling nocturnal experiments (the first six experiments in Table 4.1, we will call them as LIGHTDALL hereafter), yields,

$$\ln \tau = 0.31 \ln N_a + 0.93 \ln \text{LWP} - 3.39 \quad (4.12)$$

$$R^2 = 1.0 \text{ (1208 data points)}$$

The partial correlation coefficients of  $\tau$  versus  $N_a$  and LWP are 0.58 and 0.75, respectively. The regression result suggests that  $\tau$  is more sensitive to LWP variation than to  $N_a$ . The relationship between cloud droplet number concentration  $N_c$  and  $N_a$  at constant LWP can

be expressed empirically as,

$$N_c = 1.09N_a^{0.91} \quad (1100 \text{ data points}) \quad (4.13)$$

The above equation is obtained by the averaged regression results of  $N_c - N_a$  at every binned LWP with LWP bin size of  $5 \text{ g m}^{-2}$  with a 5 min sampling frequency during the final 3 hours (for  $\text{LWP} \geq 25 \text{ g m}^{-2}$ , Fig. 4.10). This figure also shows that our simulations agree well with the nocturnal measurement results from DYCOMS-II (Twohy et al. 2005). Using the result of Eq. (4.13), Eq. (4.12) can be expressed as,

$$\tau \propto N_c^{0.34} \quad (4.14)$$

for constant LWP. Interestingly, the result is the same as that from a homogeneous cloud of a constant LWC. However, Eq. (4.14) is the statistical product comprising the interactions of diabatic effects of radiation, precipitation, and entrainment, as well as cloud inhomogeneity.

In summary, Eq. (4.12) shows that cloud optical depth  $\tau$  is more sensitive to the dynamical variable LWP than to the microphysical variable  $N_a$ . The LWP is greatly dependent on the dynamical parameters (i.e.,  $D$  and SST). This is in agreement with Schwartz et al. (2002), who found a strong dependence of  $\tau$  on LWP, so that the LWP variability obscured the Twomey effect from the satellite measurements

## 4.6 Effect of giant sea salt on stratocumulus dynamics

Sea salt aerosols exhibit a size distribution that is strongly related to the surface wind velocity (e.g., O'Dowd et al. 1997). Because of their size, super-micron sea salt aerosols are

more readily activated at low supersaturations than are typical pollution aerosols. It has been shown by adiabatic parcel model simulations (Ghan et al. 1998 and O'Dowd et al. 1999) that under high sulfate concentrations, in the competition for available water vapor, coarse mode sea salt particles inhibit the activation of sub-micrometer sulfate particles sufficiently to reduce the total number of activated particles. In addition, large sea salt particles lead to large cloud drops that facilitate subsequent collision and coalescence and the formation of rain drops. This feature has been applied to the studies of hygroscopic seeding of cumulus clouds (e.g., Johnson 1982; Cooper et al. 1997; Yin et al. 2000; Segal et al. 2004). These numerical seeding experiments revealed that introducing giant CCN ( $r > 1 \mu\text{m}$ ) resulted in a significant potential of rain enhancement for continental (polluted) clouds. However, they found insignificant impact of seeding the maritime (clean) clouds due to already efficient collision and coalescence process in these clouds. This dynamical effect of giant sea salt aerosols on precipitation has led to the discussion of their impacts on cloud optical properties. The stratocumulus modeling study by Feingold et al. (1999b) indicates that the presence of very few giant sea salt CCN enhances drizzle production and reduces the cloud LWP; therefore, it can modulate the influence of anthropogenic aerosol considerably. Based on both the TRMM (Tropical Rainfall Measuring Mission) satellite observation of South Asian polluted air transported to the ITCZ (Intertropical Convergence Zone) over the Indian Ocean and a one-dimensional parcel model, Rosenfeld et al. (2002) also proposed the similar argument that sea salt aerosols can mitigate the anthropogenic aerosol indirect effect because the aerosol-induced precipitation suppression for polluted clouds is lessened in the presence of large sea salt particles.

#### 4.6.1 Uniform weakly precipitating stratocumulus clouds

In order to investigate the effect of large sea salt particles on stratocumulus properties, we add giant and ultra-giant sea salt aerosols to the sulfate aerosols in the simulation (GSALT, Table 4.1). The giant and ultra-giant sea salt data were taken from measurements reported in O’Dowd et al. (1997). The jet (giant) drop mode,  $r_g = 1 \mu\text{m}$ ,  $\sigma_g = 2$ , and number concentration =  $0.80 \text{ cm}^{-3}$ , and the spume (ultra-giant) drop mode,  $r_g = 6 \mu\text{m}$ ,  $\sigma_g = 3$ , and number concentration =  $3.15 \times 10^{-6} \text{ cm}^{-3}$ . These number concentrations are calculated from O’Dowd et al. (1997) assuming a surface (10-m height) wind speed of  $4.47 \text{ m s}^{-1}$  derived from the sounding profile. Sea salt density and molar mass are taken to be  $2.22 \text{ g cm}^{-3}$  (d’Almeida et al. 1991) and  $58.44 \text{ g mol}^{-1}$ , respectively. The osmotic coefficient and the number of dissociated ions for two sea salt modes are assumed 1 and 2, respectively.

The condensational growth of a particle, in terms of its radius, is inversely proportional to the radius. Therefore, the time required for particles to grow to equilibrate with the ambient water vapor concentration rapidly increases with particle size. Small particles can achieve their equilibrium sizes within seconds calculated based on Köhler theory, while large particles such as super-micron sea salt, require much longer (Mordy 1959). To account for this, we follow the assumption of Feingold et al. (1999) that giant and ultra-giant sea salt aerosol particles, when activated, grow to their 97% RH equilibrium sizes,  $r_{97}$ .  $r_{97}$  in the model is calculated by the line fitting results of the dry sea salt radius with the corresponding wet radius (Fig. 4.11), solved iteratively through the Köhler equation at  $\text{RH} = 97\%$ , i.e.,  $\ln(0.97) = A/r_{97} - \nu a^3 \rho_s M_w / M_s \rho_w r_{97}^3$ , in a broad size range. The linear regression gives a simple equation,  $r_{97} = 3.61a$  ( $a$  is the aerosol dry radius and here it refers to the giant and ultra-giant sea salt aerosols). The number and mass of activated sea salt aerosols (where  $a \geq a_{cut,i}$ ) with the wet radius of  $r_{97}$  are mapped to the cloud droplet size bins (see Fig. 4.11

for an example showing the fraction of the number of activated giant and ultra-giant sea salt CCNs mapped to the cloud droplet size bins.) Therefore, large drops initially form from the large sea salt particles. Sulfate and sea salt aerosols are activated based on the previously described multimode activation scheme.

The introduction of large sea salt particles inhibits the activation of sulfate particles by reducing maximum cloud supersaturation as a result of the competition for available water vapor. Because the cloud droplets are relatively large and few in a clean cloud, the competition for available water vapor between relatively few sea salt particles and sulfate particles does not greatly reduce the number of cloud droplets formed, as expected for polluted clouds. The clean clouds also readily precipitate, so the addition of a small number of giant sea salt particles does not greatly enhance the precipitation process. Therefore, inclusion of a small amount of giant sea salt CCN has a negligible effect on cloud properties under clean conditions; however, more noticeable impacts are seen at progressively higher sulfate aerosol concentration. Cloud droplet number concentrations are lowered by the presence of a few giant sea salt particles in the polluted cases (Fig. 4.4a). The effect on  $r_e$  of larger droplets that result from sea salt can be seen at high  $N_a$  in Fig. 4.4b. Large sea salt particles also have the potential to initiate precipitation-sized drops through collision and coalescence, and in their presence, precipitation forms for non-drizzling clouds in the BASE simulation (Fig. 4.4c,  $N_a \geq 500 \text{ cm}^{-3}$ ). The cloud LWP, however, does not show identifiable changes from adding super-micron sea salt because the surface precipitation is too small. (Fig. 4.4d). (The fluctuations in LWP in the presence of sea salt in Fig. 4.4d are comparable to the standard deviation of the data points and should not be considered of significance.) Finally, there is little impact on  $\tau$  due to sea salt; in this particular scenario, thereby, giant sea salt particles do not lessen aerosol indirect forcing. The reason is that the

BASE simulated case is a weakly drizzling stratocumulus cloud with cloud top around 800 m. (Note that Rosenfeld et al. (2002) considered much stronger cumulus convection with cloud top exceeding 2 km.) For this reason, we now consider a more heavily precipitating case.

#### 4.6.2 Heavily precipitating stratocumulus clouds

The sounding profile in the BASE simulation does not have sufficiently high humidity to produce substantial precipitation, even in the presence of the giant sea salt particles or at the low CCN conditions. To fully explore the effect of sea salt, we perform a simulation of a strongly precipitating shallow stratocumulus cloud. The simulation is initialized by the sounding profile (Fig. 4.12) from Stevens et al. (1998), based on measurements taken from ASTEX. This sounding is more humid than that in Fig. 4.1. Similar to the case in section 3a, we compare the simulation results from the horizontal domain size of  $1.1 \text{ km} \times 1.1 \text{ km}$  and of  $3.3 \text{ km} \times 3.3 \text{ km}$  (Fig. 4.13). Again, the cloud optical depth of the large domain is greater than that of the small domain. The figure shows that the trends of  $\tau$  versus  $N_a$  are different in these two domain configurations with the slope for the polluted clouds slightly larger for the large domain. Therefore, the typical  $3.3 \text{ km} \times 3.3 \text{ km}$  domain is adopted for the following ASTEX simulations.

We consider three sets of simulations using this sounding profile (Table 4.1): the first is BASEH simulation, in which only sulfate aerosols are present, the second one is UGSALTH, where the two large sea salt modes are added to the sulfate particles, and the third one is GSALTH, where only the jet drop mode sea salt is added to the sulfate as a comparison to UGSALTH. The wind speed at 10 m calculated from this sounding is  $2.12 \text{ m s}^{-1}$ , giving the sea salt number concentrations of  $0.633 \text{ cm}^{-3}$  and  $2.17 \times 10^{-6} \text{ cm}^{-3}$  for giant and ultra-

giant modes, respectively. Before conducting GSALTH and UGSALTH, we have tested the simulation in the  $1.1 \text{ km} \times 1.1 \text{ km}$  domain. Results (not shown) show that when the drizzle process is already quite active under clean conditions, the effect of giant sea salt is negligible, and it only has noticeable impacts when  $N_a \geq 1000 \text{ cm}^{-3}$ . Therefore, we only consider sulfate aerosol number concentrations above  $1000 \text{ cm}^{-3}$ , and one extra concentration of  $2500 \text{ cm}^{-3}$  is added to exhibit the giant sea salt effect.

Temporal evolution of the simulated cloud droplet number concentration and surface precipitation rate for high pollution is given in Fig. 4.14. Significant responses on the cloud droplet activation are seen during the first three hours, that cloud droplets numbers are inhibited by the coexistence of the large sea salt aerosols. Early surface precipitation formation due to the addition of the large sea salt is shown. The larger difference of the peak surface precipitation rate (and also accumulated surface precipitation) between the BASEH and GSALTH (or UGSALTH) at the higher sulfate concentration indicates a larger impact of the large sea salt. The comparison of the GSALTH and UGSALTH on several simulated variables shown in Fig. 4.14 and Fig. 4.15 suggest that the large sea salt impact is dominated by the giant (jet,  $r_g = 1 \mu\text{m}$ ) sea salt mode rather by the ultra-giant (spume,  $r_g = 6 \mu\text{m}$ ) mode, possibly because of the very small concentration of ultra-giant mode. This result is in agreement with the conclusion from the 2000-bin spectral cloud parcel model of the hygroscopic seeding study (Segal et al. 2004), which found the optimum seeding particle is around  $1.5 - 2.0 \mu\text{m}$ . In Fig. 4.16, the horizontally averaged drop number concentration spectrum at  $t = 5 \text{ h}$  shows a significant reduction of cloud droplet number concentration especially near cloud base where activation is prominent. This figure also shows that activation of ultra-giant sea salt and drop collision and coalescence result in an enhanced drop number concentration in the drizzle size category. These results

exhibiting suppression of activation of sulfate cloud droplets in the presence of giant sea salt particles are in essential agreement with cloud parcel simulations by Ghan et al. (1998) and O’Dowd et al. (1999). The averaged cloud droplet effective radius shown in Figure 4.15b is increased at large  $N_a$  in the presence of the giant sea salt aerosols. This increased effective radius significantly enhances the drizzling process (Fig. 4.15c), and the effect increases with increasing sulfate concentration.

The cloud LWP of BASEH run increases with  $N_a$  (Fig. 4.15d) because of the suppression of precipitation for more polluted clouds with smaller cloud droplet sizes, the second indirect effect. Unlike the weakly precipitating stratocumulus in section 5a, the impact of giant sea salt on lowering the cloud LWP is significant for polluted cases. Fig. 4.15e demonstrates that cloud optical depth generally shows a trend similar to that of LWP, and the impact of the sea salt increases with higher sulfate concentrations. The percentage change in cloud properties resulting from inclusion of giant sea salt (UGSALTH) relative to the base simulation (BASEH) averaged over the final hour of the simulation for polluted cases is summarized in Table 4.2. It can be seen that the effect of giant sea salt on polluted clouds increases with particle loading for  $N_a \geq 1000 \text{ cm}^{-3}$ . Suppression of the cloud LWP and cloud optical depth due to sea salt increases from around 3% to 77%. In summary, the impact of giant sea salt aerosols on cloud optical depth for polluted cases is only evident for a humid and potentially convective atmospheric environment capable of triggering active precipitation.

Finally, in order to assess the effect of higher sea salt concentrations associated with higher wind speed, we increased the initial  $v$ -component wind speed to  $10 \text{ m s}^{-1}$  (UGSALTHV10, Table 4.1); the giant sea salt number concentrations calculated based on this wind speed are  $1.36 \text{ cm}^{-3}$  and  $7.6 \times 10^{-6} \text{ cm}^{-3}$  for giant and ultra-giant drop modes, respectively. Simula-

tion results for  $N_a = 1500$  and  $2000 \text{ cm}^{-3}$  are shown in Fig. 4.15 and Table 4.2, indicating stronger wind shear leads to a more turbulent boundary layer and produces more sea salt aerosol activated. Therefore, the greater sea salt impacts are seen under the stronger wind shear.

### 4.6.3 *Aerosol washout*

The heavily precipitating cloud described in the previous subsection could result in a noticeable removal of aerosol number concentration due to the wet scavenging of the aerosol particles with the rain drops. We apply the size dependent first-order number washout coefficients from Dana and Hales (1976) to the aerosol number concentration governing equation. The washout coefficients consider Brownian diffusion, interception, and inertial impaction, which are derived from their Table 3 for the sulfate aerosol lognormal distribution specified in section 3a. The washout coefficient is a function of the drizzle size. The aerosol number concentration is now treated as a prognostic scalar, affected by advection, turbulent eddy mixing, and washout. We only perform the simulations for clean clouds ( $N_a = 50$  and  $100 \text{ cm}^{-3}$ ), named as WASHOUTH (Table 4.1), owing to prominent drizzling and thereby larger drizzle washout efficiency relative to the polluted clouds. A test of aerosol washout using  $N_a = 2000 \text{ cm}^{-3}$  verified that explicit treatment of washout introduces negligible effects to the simulated polluted cloud properties (not shown). Simulation results (Fig. 4.17) display that because of the aerosol washout by drizzle drops, the subsequently activated cloud droplets numbers are reduced, resulting in larger cloud effective radius, enhancement of drizzling, and simultaneous reductions of cloud LWP and optical depth. However, the results also show that the slopes of the LWP- $N_a$  (Fig. 4.17d) and  $\tau$ - $N_a$  (Fig. 4.17e) relationships are close to those that do not include the aerosol washout mechanism, suggesting that

neglect of this mechanism does not significantly affect the LWP- $N_a$  and  $\tau$ - $N_a$  relationships with only sulfate aerosols present.

## 4.7 Daytime conditions

Although many studies of stratocumulus clouds focus on the nocturnal clouds, the aerosol indirect effect applies to daytime conditions. Therefore we have carried out simulations for the light precipitation case BASE and the heavily precipitating case BASEH with solar radiation, that is BASESW and BASEHSW, respectively (Table 4.1). The simulation time spans from local standard time 0900 to 1500. To conform with our previous analysis procedure, the last three hours and last one hour results for BASESW and BASEHSW are used and shown in Fig. 4.4 and Fig. 4.18, respectively. For both cases, the solar heating absorbed by the cloud offsets the cloud-top LW cooling, which is the driving force for the turbulent eddies in the MBL. Both the turbulent kinetic energy and  $\overline{w'w'}$  are decreased (not shown). The daytime clouds become thinner with fewer number of activated cloud droplets than the nocturnal clouds as result of weaker updraft. The daytime cloud LWP is decreased mostly due to the shallower cloud depth. Consequently, daytime cloud optical depth is smaller than that of the nighttime cloud in response of the smaller LWP. The surface precipitation (not shown) is also decreased during daytime due to weaker boundary turbulence. For BASESW, the LWP and cloud optical depth show similar trends but smaller magnitude as compared with the results from nocturnal BASE. For BASEHSW, besides the weaker turbulent motion, the stratocumulus is decoupled from the subcloud layer due to the solar heating within the cloud. The daytime decoupled MBL has been observed during the ASTEX field campaign (Ciesielski et al. 2001). The MBL structure shows a thin solid layer of stratocumulus at the top with underlying cumuli (not shown). The decoupled

MBL cuts off the moisture transport to the cloud layer and greatly reduces the cloud LWP. However, because of essentially no precipitation, the cloud LWP does not respond to CCN number variation, which is consistent with the simulation results in Ackerman et al. (2003) and the Monterey Area Ship Track (MAST) observations (Ferek et al. 2000).

To evaluate the effect of cloud dynamics through night on the daytime simulations, we carry out the simulations of the entire diurnal cycle for several selected aerosol number concentrations (BASEHDIU, see Table 4.1). The diurnal simulation starts from the local standard time 2300 to 1600. Results for early morning (08–10h), noon (11–13h), and afternoon (14–16h) are shown in Fig. 4.18. Temporal evolutions show the cloud droplet number concentration, LWP, cloud optical depth, and albedo reduced from nighttime to daytime. The results of afternoon BASEHDIU generally agree with BASEHSW; therefore, neglecting the nighttime cloud dynamics does not produce a significant effect on the daytime simulated variables shown in Fig. 4.18. Early morning BASEHDIU still exhibits nighttime characteristics such that the trends of the variables versus  $N_a$  shown in Fig. 4.18 are similar to those from BASEH.

## 4.8 Implications for the aerosol indirect effect

Cloud optical depth depends on both  $N_a$  and LWP. LWP is strongly dependent on external dynamical forcing parameters, e.g., SST and large-scale divergence rate. Through statistical analysis of the simulations shown in section 4, the cloud optical depth is found to be more sensitive to LWP than to  $N_a$ . It is of interest to evaluate the relative importance of the microphysical and dynamical effects contributing to aerosol indirect forcing. We can

write from Eq. (4.12),

$$\left. \frac{\partial \ln \tau}{\partial \ln N_a} \right|_{D, \text{SST}} = \alpha + \beta \left. \frac{\partial \ln \text{LWP}}{\partial \ln N_a} \right|_{D, \text{SST}} \quad (4.15)$$

For the six lightly precipitating experiments of Eq. (4.12) (i.e., LIGHTDALL), the constants  $\alpha = 0.31$  and  $\beta = 0.93$ . The term on the left hand side is the aerosol indirect effect. The first term on the right hand side ( $\alpha$ ) represents the Twomey effect. For a spatially uniform cloud with a monodisperse cloud droplet spectrum,  $\tau \approx \text{LWP}^{\frac{2}{3}} N_c^{\frac{1}{3}} H$  (Seinfeld and Pandis 1998). Using the empirical relationship of Eq. (4.13), this idealized cloud gives the same microphysical sensitivity of 0.3 as Eq. (4.15) for a constant LWP. The second term on the right hand side of Eq. (4.15) ( $\beta \left. \frac{\partial \ln \text{LWP}}{\partial \ln N_a} \right|_{D, \text{SST}}$ ), the second aerosol indirect effect, represents the change of LWP in response to the change in  $N_a$ , i.e., the cloud dynamical effect such as the change of cloud LWP (Albrecht, 1989) or change of cloud depth (Pincus and Baker 1994) due to aerosol suppression of drizzle. Pincus and Baker (1994) found that the albedo susceptibility is increased by 50 – 200% when the dependence of cloud depth on particle number is included.

Table 4.3 summarizes Eq. (4.15) for the different experiments of this study. The constants  $\alpha$  and  $\beta$  for all cases shown in the table are the multiple regression coefficients of cloud optical depth with aerosol number concentration and cloud LWP. The value of  $\left. \frac{\partial \ln \text{LWP}}{\partial \ln N_a} \right|_{D, \text{SST}}$  is from the slope of the linear regression of LWP with  $N_a$  in the natural log space. Results from Table 4.3 show that clean cases give larger absolute values of  $\left. \frac{\partial \ln \text{LWP}}{\partial \ln N_a} \right|_{D, \text{SST}}$  than polluted cases (except for UGSALTH), and hence the clean clouds exhibit a larger second indirect effect than polluted clouds. It is because for the same meteorological condition, clean clouds more readily produce surface precipitation or cloud drop

sedimentation flux than polluted clouds. Heavy surface precipitation can reduce the cloud LWP directly through the drops collision and coalescence process; the more pollution, the smaller droplets, and the less precipitation efficiency. Therefore, this aerosol suppression of drizzle will result in a positive  $\beta \left. \frac{\partial \ln \text{LWP}}{\partial \ln N_a} \right|_{D, \text{SST}}$ , i.e., a positive second indirect effect and amplifies the overall indirect effect, as suggested from the aerosol suppression of drizzle by Albrecht (1989) and Pincus and Baker (1994). In our simulations, clean clouds that produce high precipitation amounts (BASEH and BASEHDIU (08-10h)), can be explained by this effect. However, the small negative, or close to zero, aerosol second indirect effect is seen for the clouds that produce little precipitation (LIGHTDALL, BASESW, and BASEHSW). For these cases, drizzle production is inefficient in reducing the cloud LWP. The negative sign for  $\left. \frac{\partial \ln \text{LWP}}{\partial \ln N_a} \right|_{D, \text{SST}}$  is likely be due to the slight increase of entrainment drying associated with less efficient cloud droplet sedimentation at high aerosol concentrations. Similar discussions are also seen in the recent work by Ackerman et al. (2004). They further found the condition for the positive sign of  $\left. \frac{\partial \ln \text{LWP}}{\partial \ln N_a} \right|_{D, \text{SST}}$  is only when significant surface precipitation for the stratocumulus clouds is greater than  $0.1 \text{ mm day}^{-1}$ , which is also favored by humid free tropospheric air or very low aerosol concentration.

Daytime (results are averaged during the afternoon) simulations for both the lightly and heavily drizzling cases (BASESW and BASEHSW) show a reduction of the magnitude of the aerosol indirect effect resulting from cloud thinning due to cloud solar absorption. Precipitation is significantly reduced in the daytime simulations, and the aerosol indirect effect is dominated by the Twomey effect. Although the largest values of the aerosol effect occur at nighttime instead of daytime, we have found through the diurnal cycle simulations, the early morning clouds of BASEHDIU shows similar trends of cloud droplet number concentration, LWP, cloud optical depth, and cloud albedo versus aerosol number concentration, and re-

sults in comparable aerosol indirect effects with nighttime clouds (BASEH). Therefore, the nighttime results can be applied to early morning cloud (e.g., 6 – 10 AM) when solar heating is small. Results also suggest that to accurately evaluate the aerosol indirect forcing, the diurnal evolutions of the aerosol indirect effects should be considered. Lastly, the interesting feature of this table shows that the giant sea salt aerosol (UGSALTH) exhibits a negative  $\frac{\partial \ln \text{LWP}}{\partial \ln N_a} \Big|_{D, \text{SST}}$ , which leads to a negative second indirect effect large enough to alter the sign of the overall aerosol effect.

## 4.9 Acknowledgments

This work was supported by Office of Naval Research Grant N-00014-96-1-0119. The authors especially appreciate comments from Dr. Graham Feingold. We also acknowledge computational resources from Caltech Center for Advanced Computing Research.

Table 4.1: Conditions of simulations

Experiment	$N_a$ ( $\text{cm}^{-3}$ )	Domain# $D$ (km)	$D$ ( $\text{s}^{-1}$ )	SST (K)	Aerosol composition	Night- /Daytime cloud	Sounding
BASE	50,100,500,1000,1500,2000	1.1	$5 \times 10^{-6}$	288	sulfate	night	Fig. 4.1
DIV2	50,100,500,1000,1500,2000	1.1	$2 \times 10^{-6}$	288	sulfate	night	Fig. 4.1
DIV6	50,100,500,1000,1500,2000	1.1	$6 \times 10^{-6}$	288	sulfate	night	Fig. 4.1
DIV10	50,100,500,1000,1500,2000	1.1	$10 \times 10^{-6}$	288	sulfate	night	Fig. 4.1
SST2	50,100,500,1000,1500,2000	1.1	$5 \times 10^{-6}$	290	sulfate	night	Fig. 4.1
SST4	50,100,500,1000,1500,2000	1.1	$5 \times 10^{-6}$	292	sulfate	night	Fig. 4.1
UGSALT	50,100,500,1000,1500,2000	1.1	$5 \times 10^{-6}$	288	sulfate and giant and ultra-giant drop modes sea salt	night	Fig. 4.1
BASESW	50,100,500,1000,1500,2000	1.1	$5 \times 10^{-6}$	288	sulfate	day	Fig. 4.1
BASELG	50,100,500,1000,1500,2000	3.3	$5 \times 10^{-6}$	288	sulfate	night	Fig. 4.1
SST4LG	50,100,500,1000,1500,2000	3.3	$5 \times 10^{-6}$	292	sulfate	night	Fig. 4.1
BASEH	50,100,500,1000,1500,2000,2500	3.3	$5 \times 10^{-6}$	290.4	sulfate	night	Fig. 4.12
BASEHSM	50,100,500,1000,1500,2000,2500	1.1	$5 \times 10^{-6}$	290.4	sulfate	night	Fig. 4.12
UGSALTH	1000,1500,2000,2500	3.3	$5 \times 10^{-6}$	290.4	sulfate and giant and ultra-giant drop modes sea salt	night	Fig. 4.12
UGSALTHV10	1500,2000	3.3	$5 \times 10^{-6}$	290.4	sulfate and giant and ultra-giant drop modes sea salt*	night	Fig. 4.12
GSALTH	1500,2000,2500	3.3	$5 \times 10^{-6}$	290.4	sulfate and giant drop mode sea salt	night	Fig. 4.12
WASHOUTH	50,100,2000	3.3	$5 \times 10^{-6}$	290.4	sulfate with aerosol washout mechanism	night	Fig. 4.12
BASEHSW	50,100,500,1000,1500,2000,2500	3.3	$5 \times 10^{-6}$	290.4	sulfate	day	Fig. 4.12
BASEHDIU	50,100,500,1500,2500	3.3	$5 \times 10^{-6}$	290.4	sulfate	diurnal**	Fig. 4.12

# Domain size is the same in both  $x$  and  $y$  directions.

\* Sea salt number concentration is calculated at the sounding profile of  $v = 10 \text{ m s}^{-1}$ .

\*\* for local standard time from 2300 to 1600.

Table 4.2: Relative change in averaged cloud properties due to introduction of large sea salt aerosols into BASEH simulation<sup>a</sup>.

$N_a$ ( $\text{cm}^{-3}$ )	$N_c$ (%)			$r_e$ (%)			Accum sfc precip (%)		
	UGSALTH	GSALTH	UGSALTHV10	UGSALTH	GSALTH	UGSALTHV10	UGSALTH	GSALTH	UGSALTHV10
1000	-22.1			-4.7			11.5		
1500	-30.9	-33.6	-48.6	0.2	1.2	4.8	19.4	20.1	40.2
2000	-39.9	-37.3	-58.0	0.9	-0.1	11.2	37.5	36.8	47.2
2500	-58.0	-46.5		66.6	25.0		79.9	77.6	

<sup>a</sup>Results are averaged over the last 1 hour of the simulation.

Table 4.2: Continued

$N_a$ ( $\text{cm}^{-3}$ )	LWP (%)			$\tau$ (%)			Albedo (%)		
	UGSALTH	GSALTH	UGSALTHV10	UGSALTH	GSALTH	UGSALTHV10	UGSALTH	GSALTH	UGSALTHV10
1000	-4.8			-3.3			-0.5		
1500	-10.9	-11.7	-28.7	-14.4	-16.3	-36.7	-1.9	-2.2	-6.4
2000	-22.3	-21.6	-29.6	-27.4	-25.4	-41.1	-4.1	-3.7	-7.3
2500	-64.0	-53.8		-77.0	-64.3		-28.2	-17.7	

Table 4.3: Evaluation of aerosol indirect effect of Eq. (4.15) and the contribution from the first and second aerosol indirect effect

$$\left. \frac{\partial \ln \tau}{\partial \ln N_a} \right|_{D, \text{SST}} = \alpha + \beta \left. \frac{\partial \ln \text{LWP}}{\partial \ln N_a} \right|_{D, \text{SST}}$$

Experiment	$\left. \frac{\partial \ln \tau}{\partial \ln N_a} \right _{D, \text{SST}}$		$\alpha$	$\beta$	$\left. \frac{\partial \ln \text{LWP}}{\partial \ln N_a} \right _{D, \text{SST}}$	
	Clean	Polluted			Clean	Polluted
LIGHTDALL	0.22±0.07 (444)	0.28±0.05 (888)	0.31	0.93	-0.10±0.08	-0.03±0.05
BASESW	0.18 (74)	0.23 (148)	0.29	0.79	-0.14	-0.08
BASEH	0.87 (26)	0.46 (65)	0.22	1.10	0.59	0.22
BASEHDIU (08-10h)	0.67 (50)	0.48 (75)	0.29	0.96	0.40	0.20
BASEHSW	0.30 (26)	0.30 (65)	0.29	1.10	0.01	0.01
UGSALTH		-1.0 (52)	0.21	1.55		-0.78

The number in the parenthesis denotes the number of data points. Data points are obtained by a 5 min sampling frequency during the last three/one hours for FIRE/ASTEX drizzling case except for BASEHDIU.

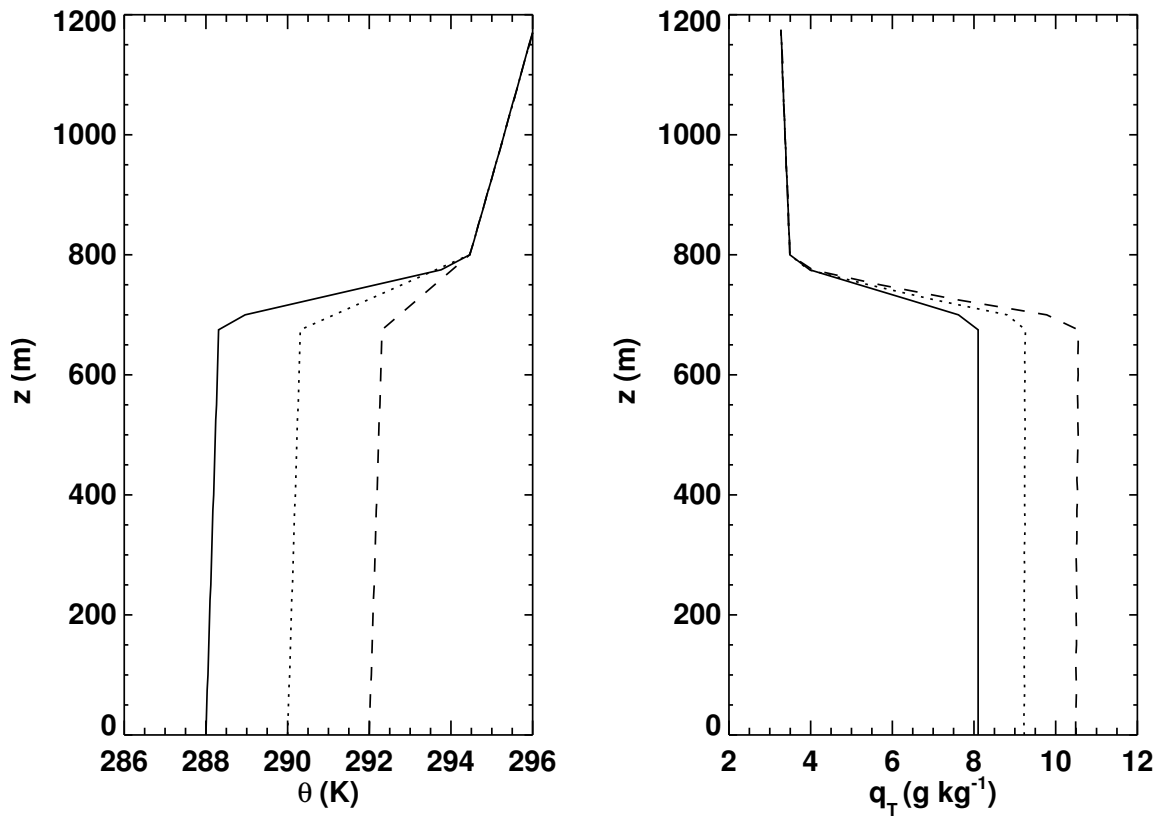


Figure 4.1: Initial sounding profile for a lightly drizzling stratocumulus cloud. Solid line is for BASE run (data from Moeng et al. 1996); dotted line is for SST2 run; dashed line is for SST4 run.

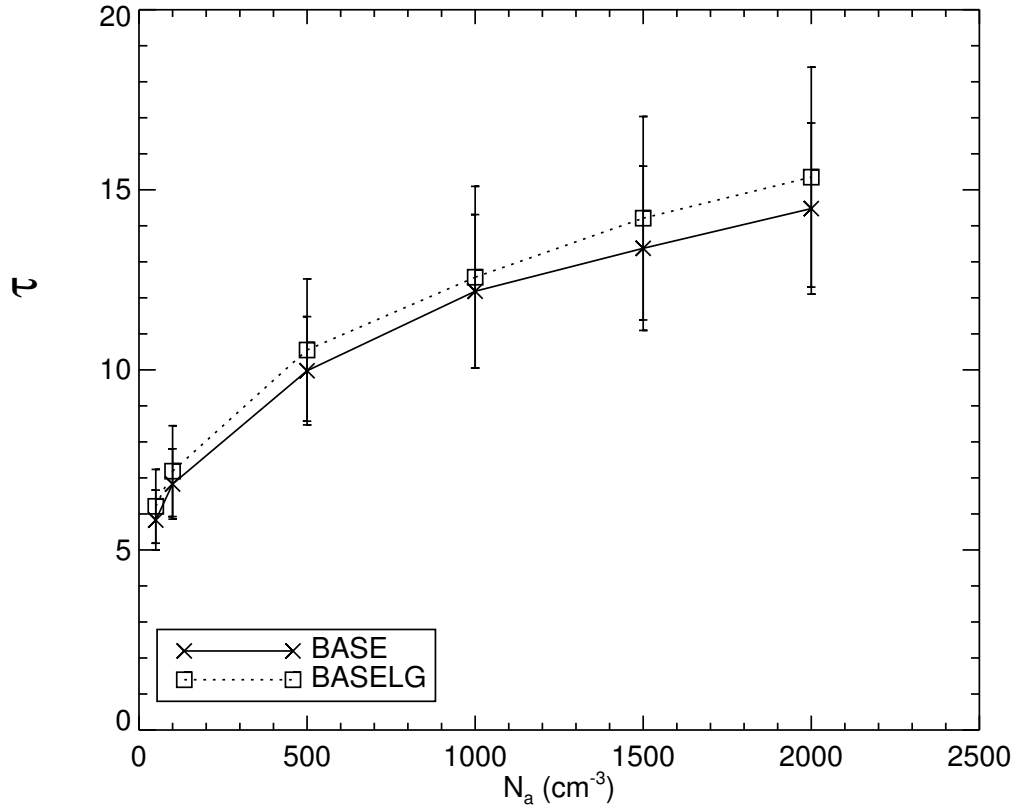


Figure 4.2: Effect of region size on averaged cloud optical depth as a function of aerosol number concentration. BASE run (solid line) performed over a horizontal region of  $1.1 \text{ km} \times 1.1 \text{ km}$ , while the same configuration but a domain of  $3.3 \text{ km} \times 3.3 \text{ km}$  (BASELG) is shown as the dotted line. The average is performed over the horizontal domain during the final 3 h of the simulation. Error bars represent the standard deviation of the domain-averaged values.

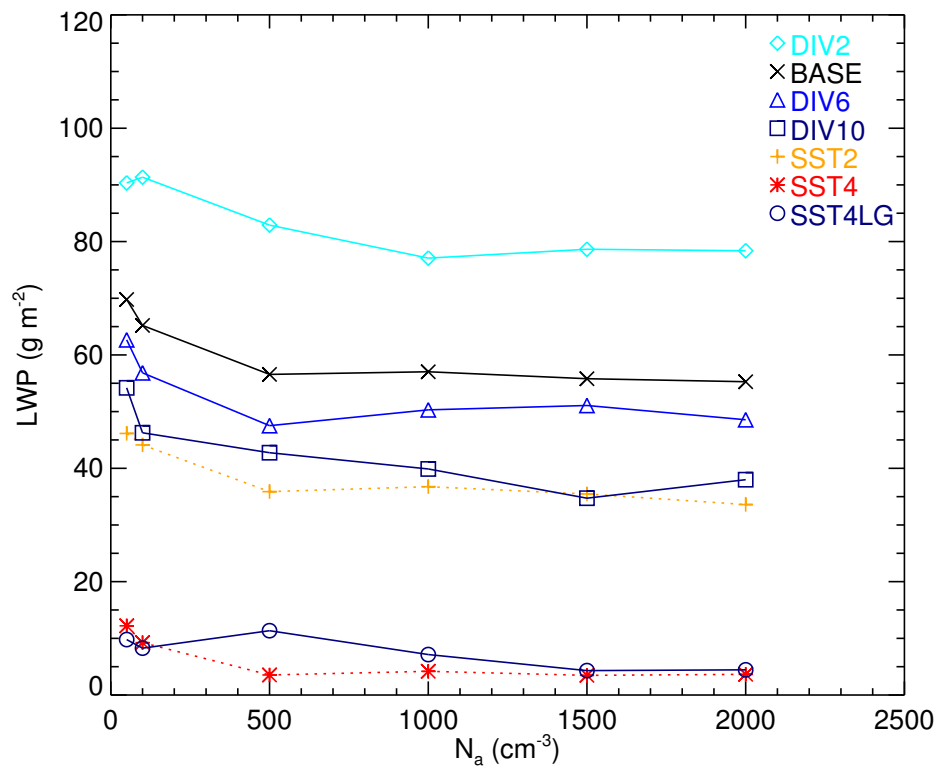


Figure 4.3: Cloud LWP for seven simulations defined in Table 4.1. Data points are averages over the horizontal domain during the final 3 h of the simulation.

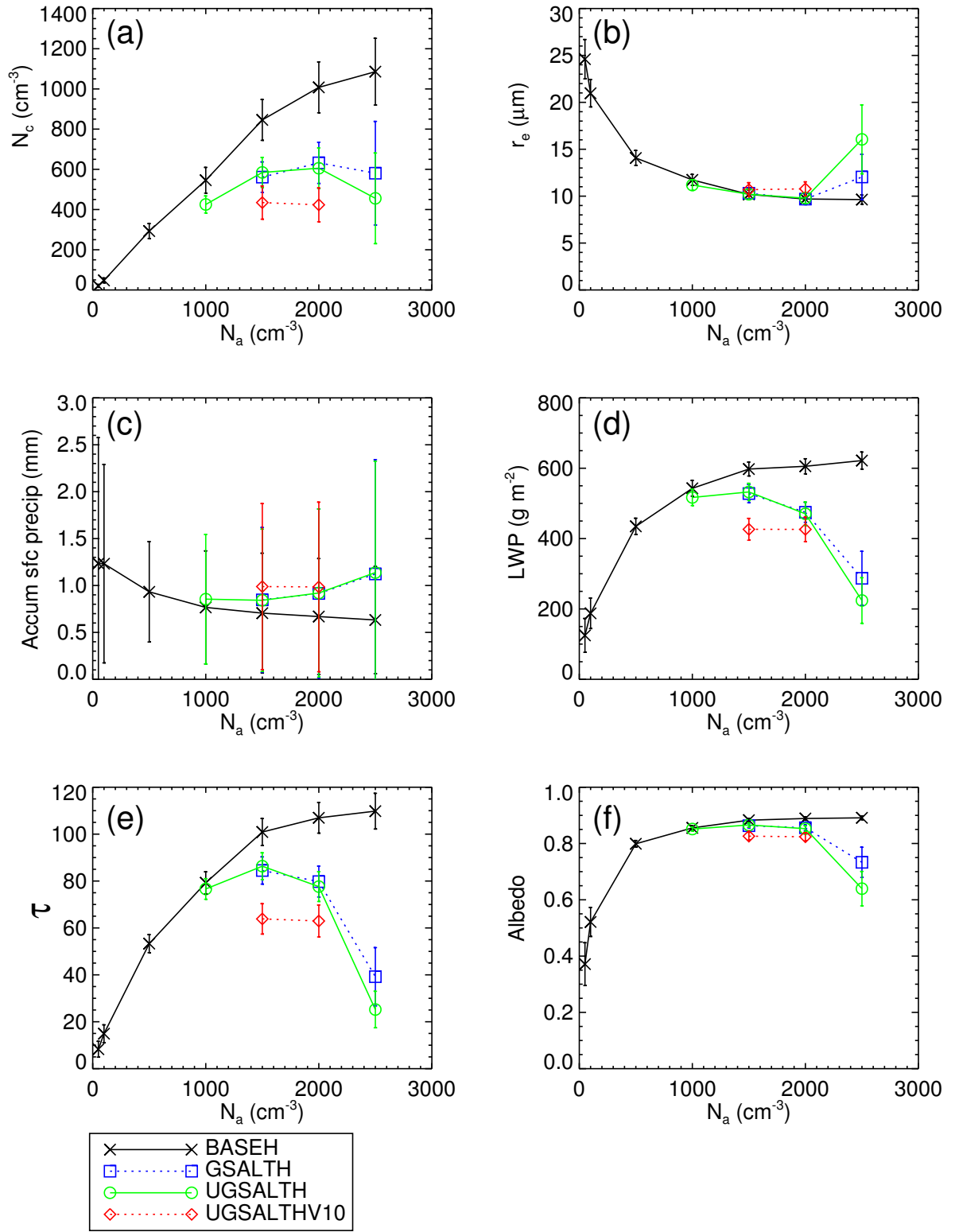


Figure 4.4: Super-micron sea salt effect (see section 5 for details) for weakly precipitating stratocumulus cloud (a)  $N_c$ , (b)  $r_e$ , (c) accumulated surface precipitation, (d) cloud LWP, (e)  $\tau$ , and (f) cloud albedo for BASE, UGSALT, and BASESW. The accumulated surface precipitation is summed over the six-hour simulations.

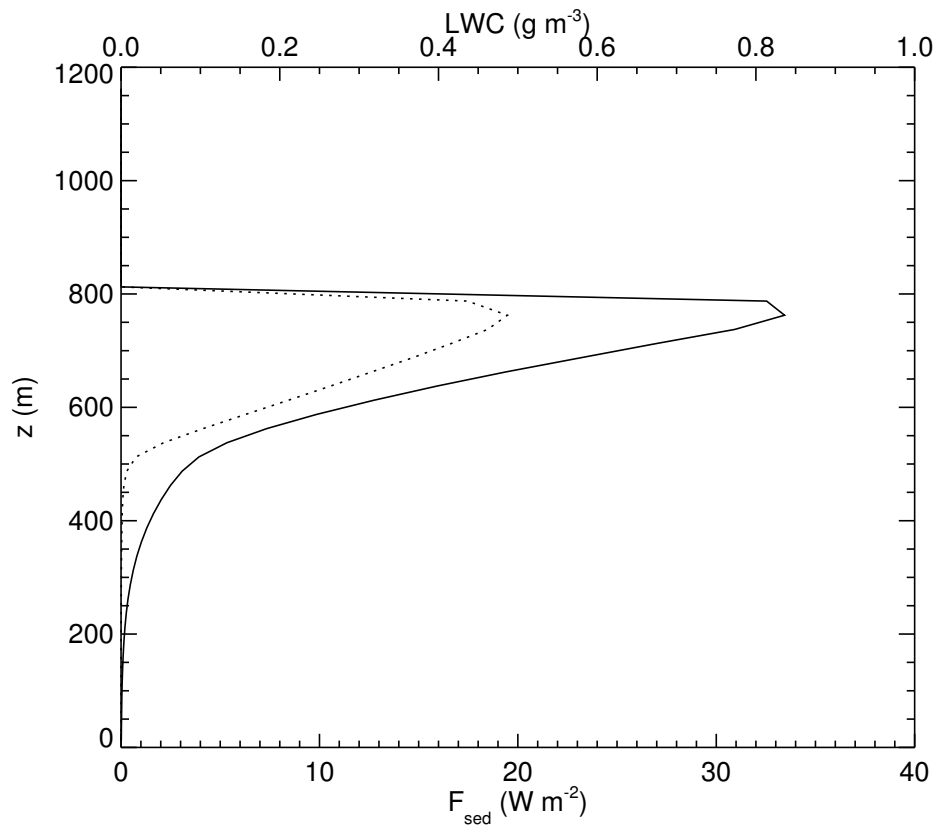


Figure 4.5: Vertical profiles of sedimentation flux (solid line, lower axis) and LWC (dotted line, upper axis) for BASE  $N_a=50 \text{ cm}^{-3}$ , horizontally averaged over the final 3 h of the simulation.

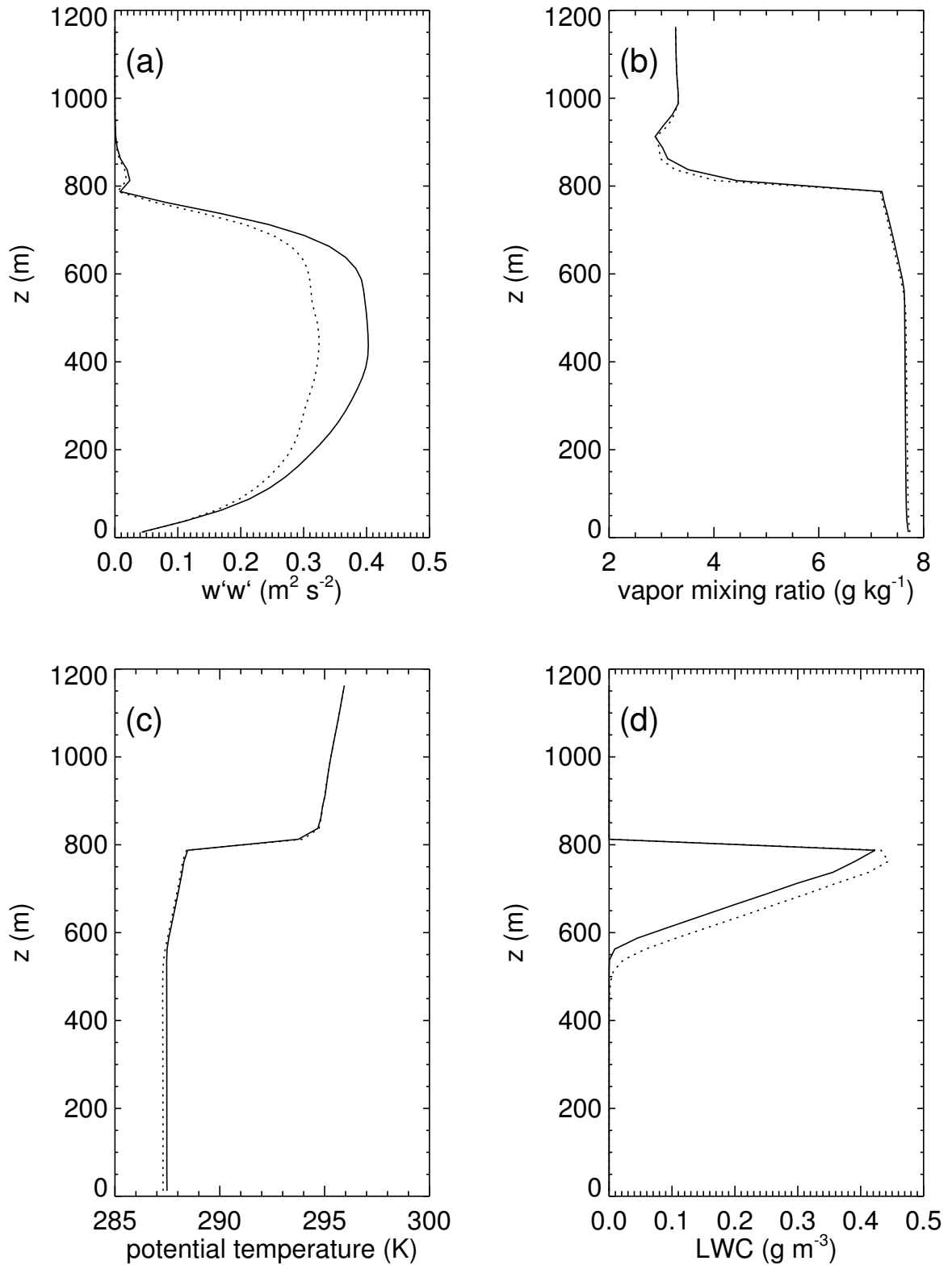
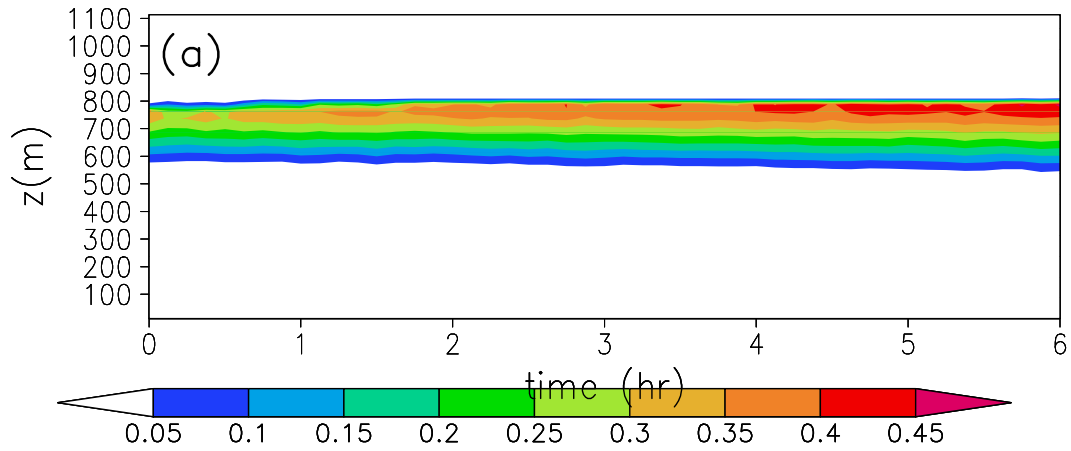
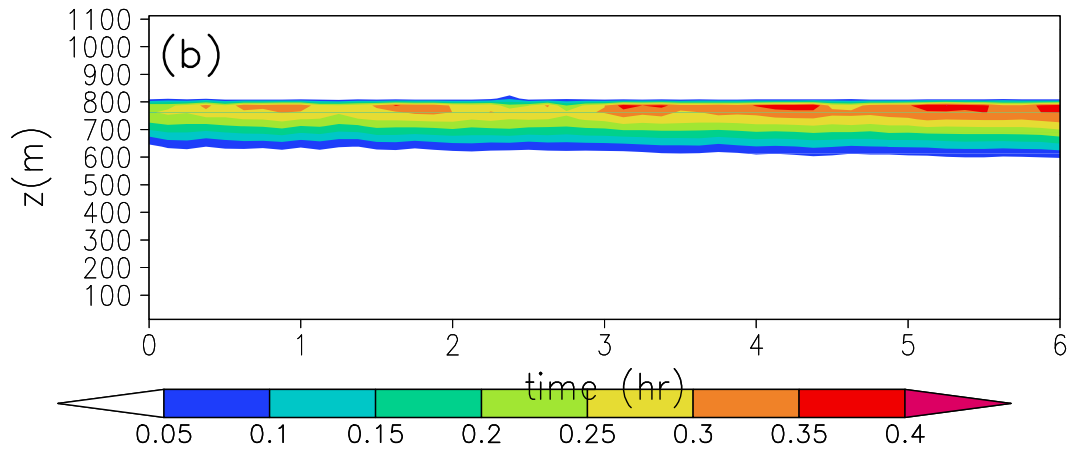


Figure 4.6: Vertical profiles of the temporally (last 3 hours) and horizontally averaged (a) vertical velocity variance, (b) water vapor mixing ratio, (c) potential temperature, and (d) cloud LWC. Solid line represents the non-drizzling cloud (BASE,  $N_a = 2000 \text{ cm}^{-3}$ ) and the dotted line represents the drizzling cloud (BASE,  $N_a = 50 \text{ cm}^{-3}$ ).

## BASE



## SST2



## SST4

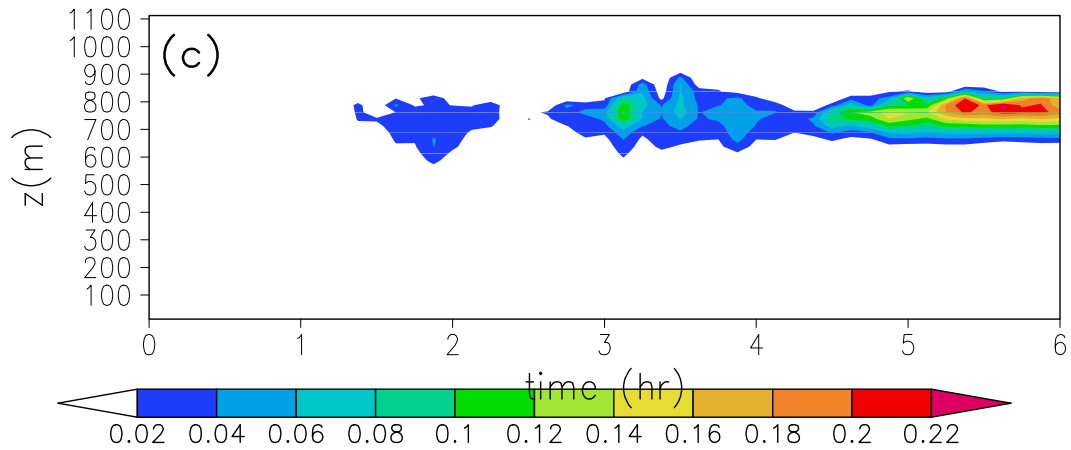


Figure 4.7: Temporal evolution of horizontally averaged cloud mixing ratio ( $\text{g kg}^{-1}$ ) for (a) BASE, (b) SST2, and (c) SST4. Aerosol number concentration is  $50 \text{ cm}^{-3}$ . Cloud optical depth versus cloud LWP for clean and polluted cases for eight simulations. Data points are averaged over the horizontal domain.

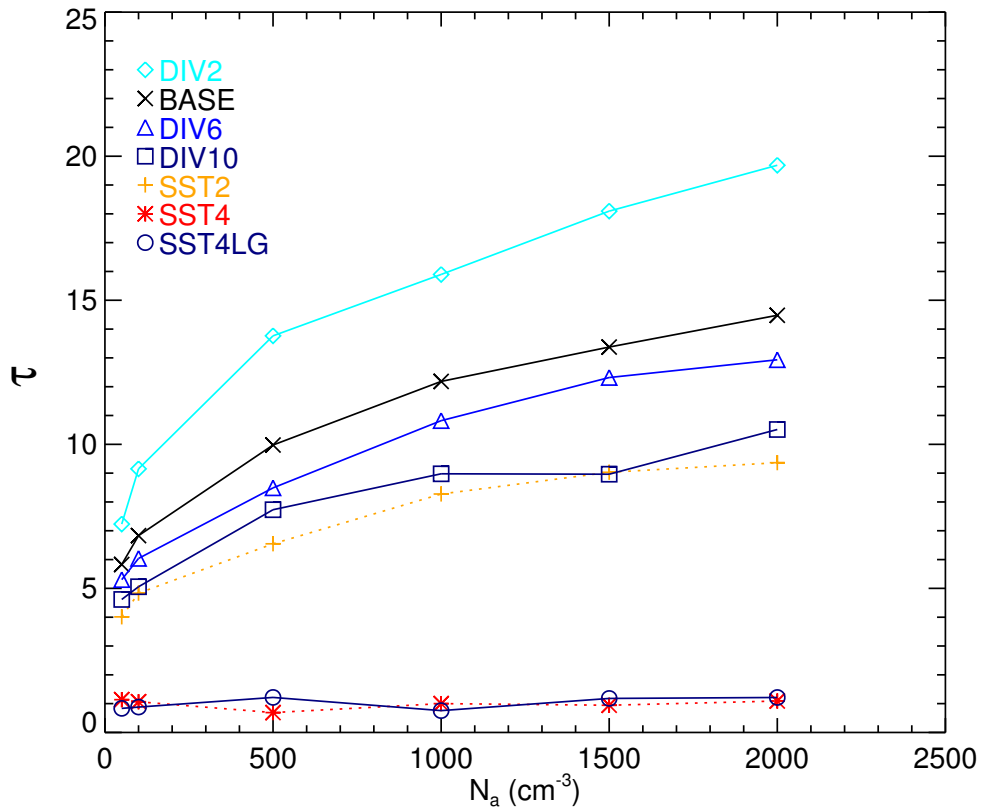


Figure 4.8: Cloud optical depth for seven simulations defined in Table 4.1. Data points are averages over the horizontal domain during the final 3 h of the simulation.

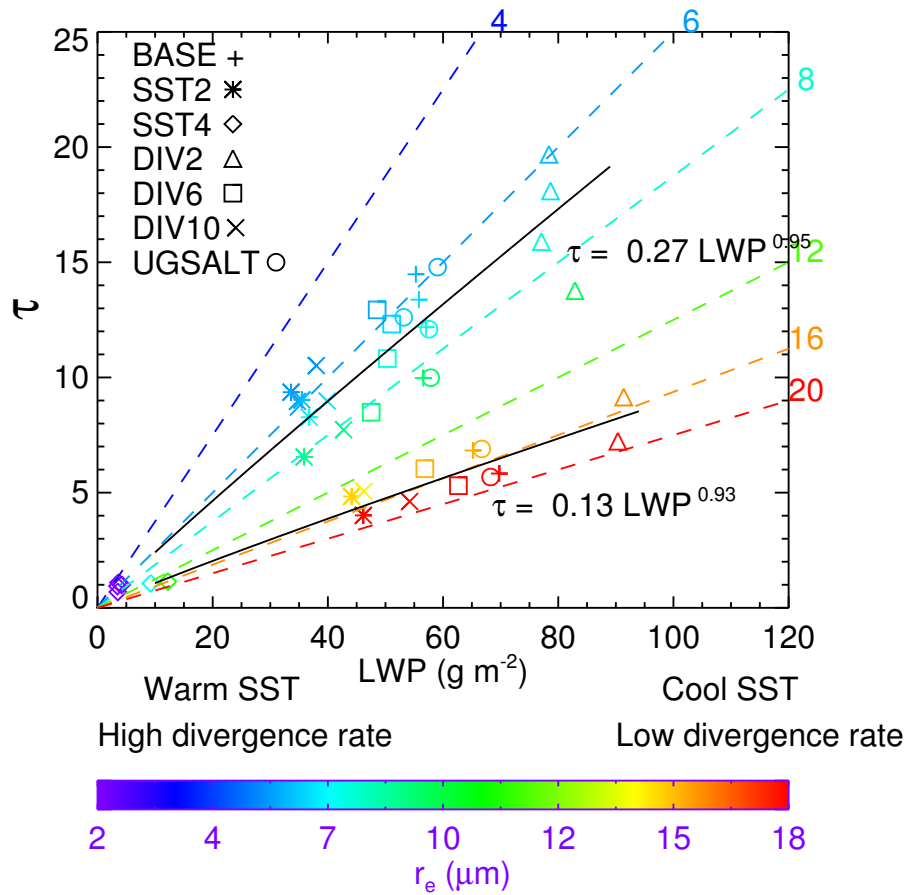


Figure 4.9: Cloud optical depth versus cloud LWP for clean and polluted (data points below the constant line of  $r_e = 12 \mu\text{m}$ ) cases for eight simulations. Data points are averaged over the horizontal domain; except that  $r_e$  is averaged over the upper one-third of the cloud layer.  $r_e$  is colored by its value given in the colorbar. Overlain dashed lines are the theoretical  $r_e$  defined in Stephens (1978).

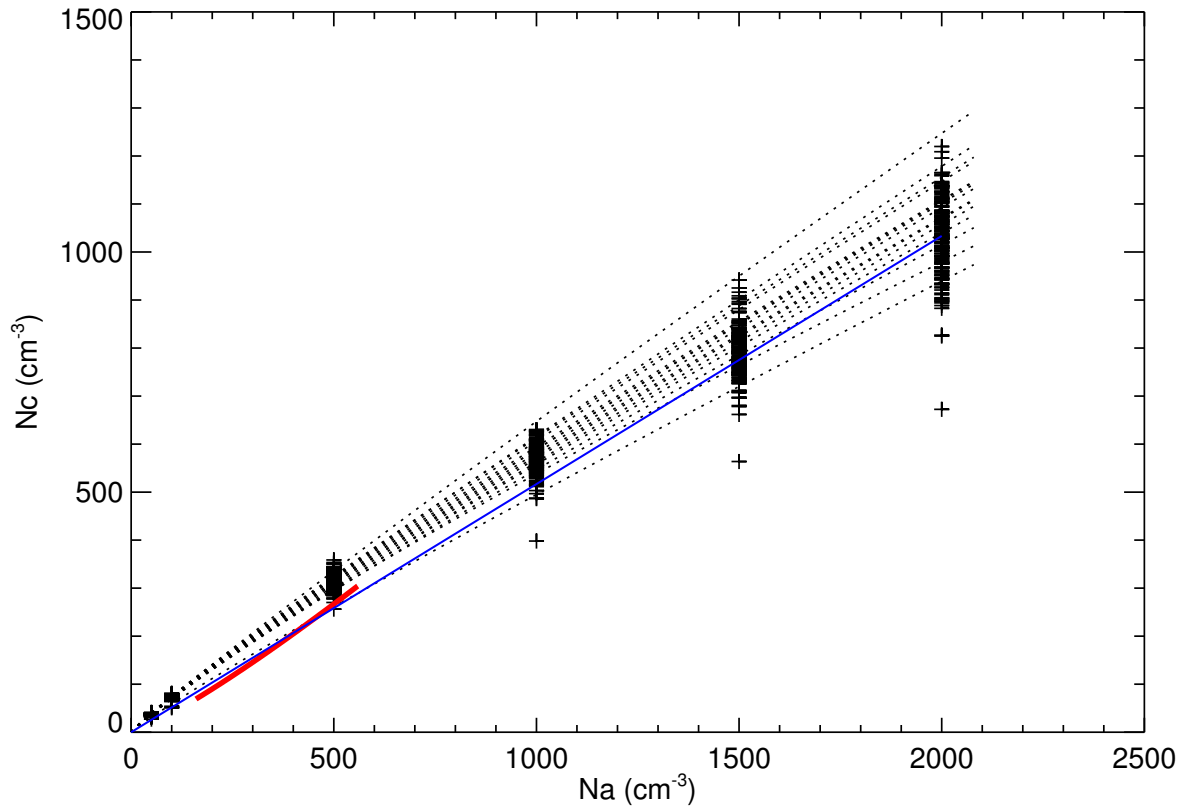


Figure 4.10: Regression of  $N_c$  versus  $N_a$  at every binned LWP with bin size of  $5 \text{ g m}^{-2}$  with 5 min sampling frequency (for  $\text{LWP} \geq 25 \text{ g m}^{-2}$ , data points are represented by plus) during the final 3 h (dotted lines). The line solid line is the averaged results of the dotted lines. The short thick line is from DYCOMS-II measurements (Fig. 1 of Twohy et al. 2005).

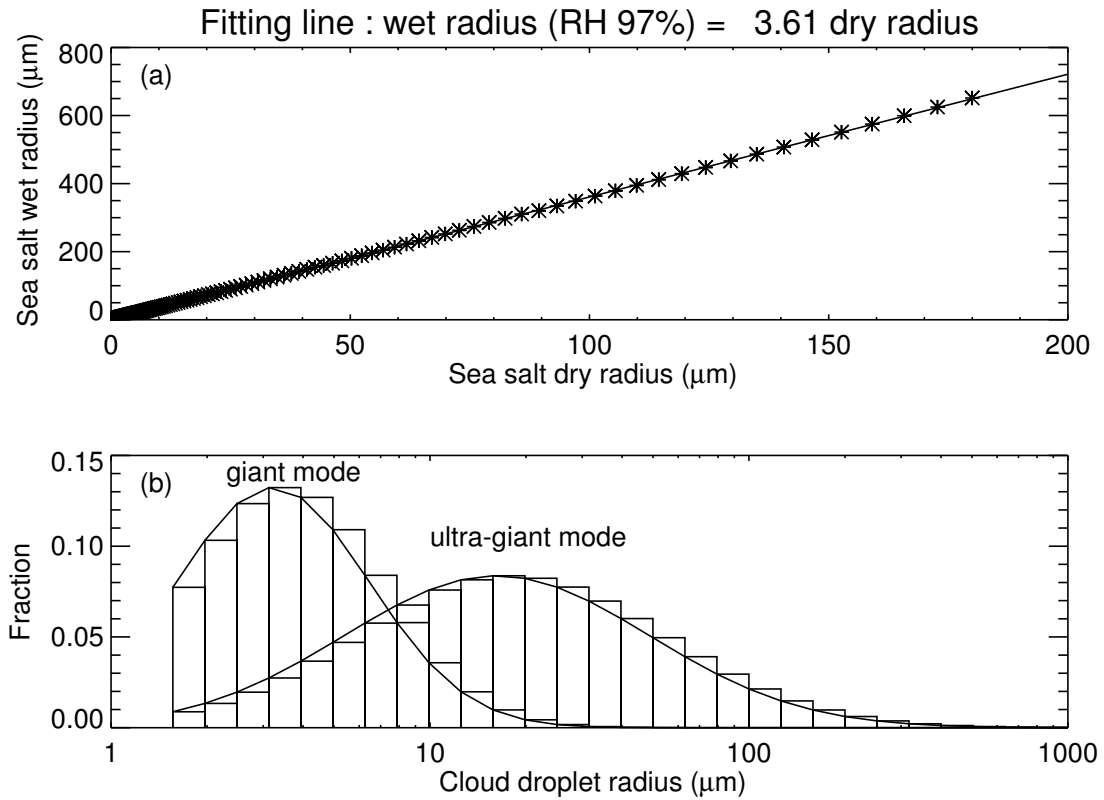


Figure 4.11: (a) Linear regression results of the dry sea salt aerosol radius with the corresponding wet radius at  $\text{RH} = 97\%$ ,  $r_{97}$ , at 285K for 200 size bins in the dry size range of  $r_g(\text{giant})/10 \sigma_g(\text{giant}) = 0.05 \mu\text{m} - 10 r_g(\text{ultra-giant})/\sigma_g(\text{ultra-giant}) = 180 \mu\text{m}$ ; (b) Spectrum of fractions of the number of activated giant- and ultra-giant- sea salt aerosols mapped to the 36 cloud droplet size bins in the model.

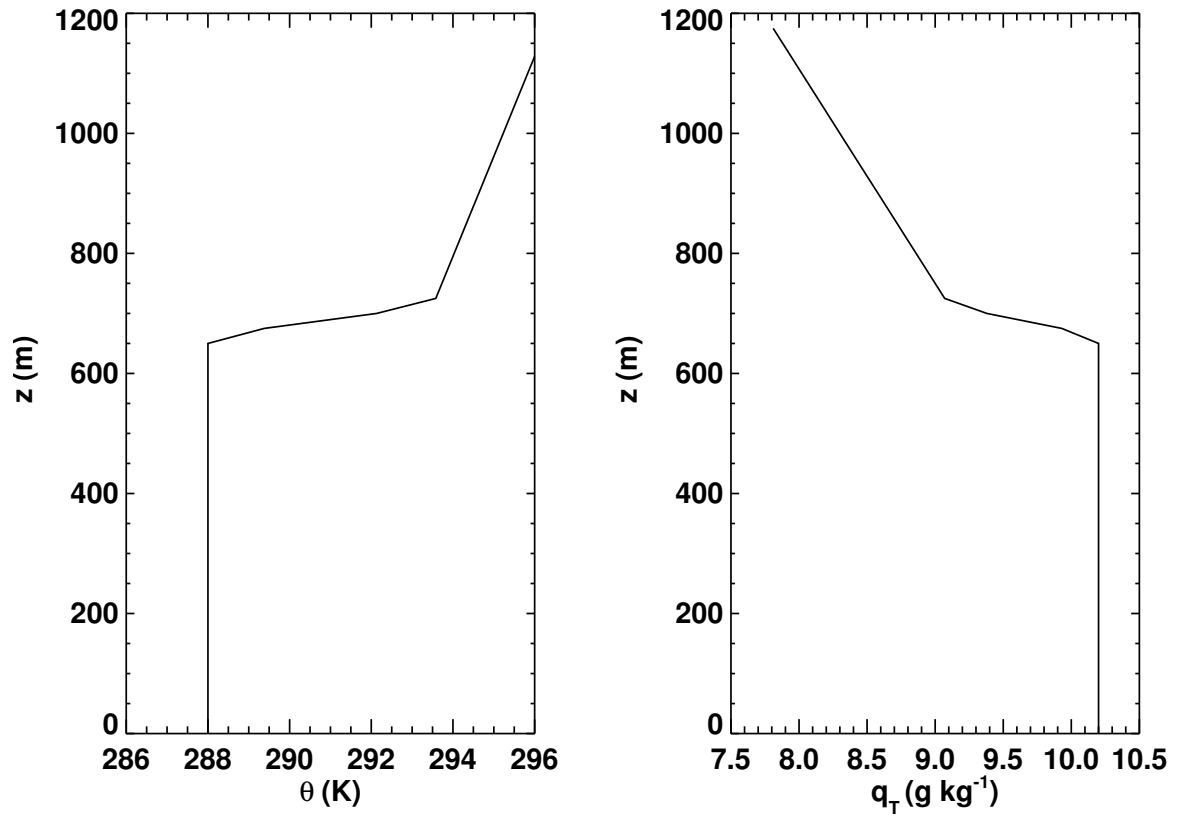


Figure 4.12: Initial sounding profile for a heavily precipitating stratocumulus cloud (data from Stevens et al. 1998).

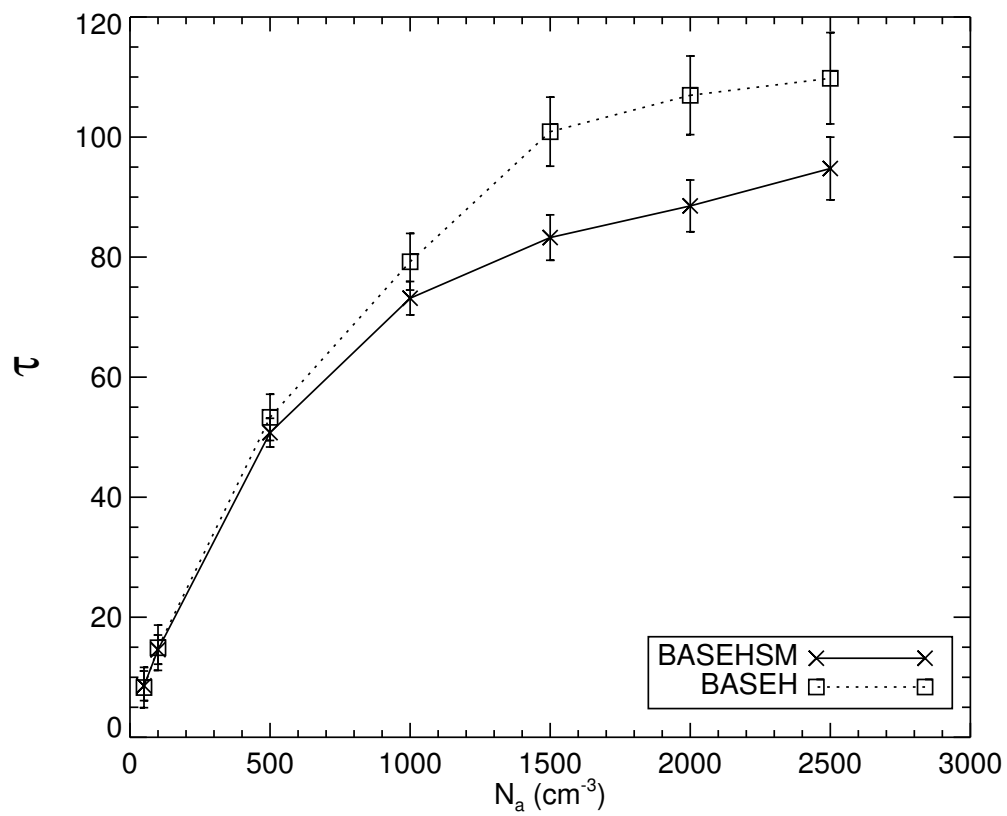


Figure 4.13: Same as Fig. 4.2 but for the BASEH run.

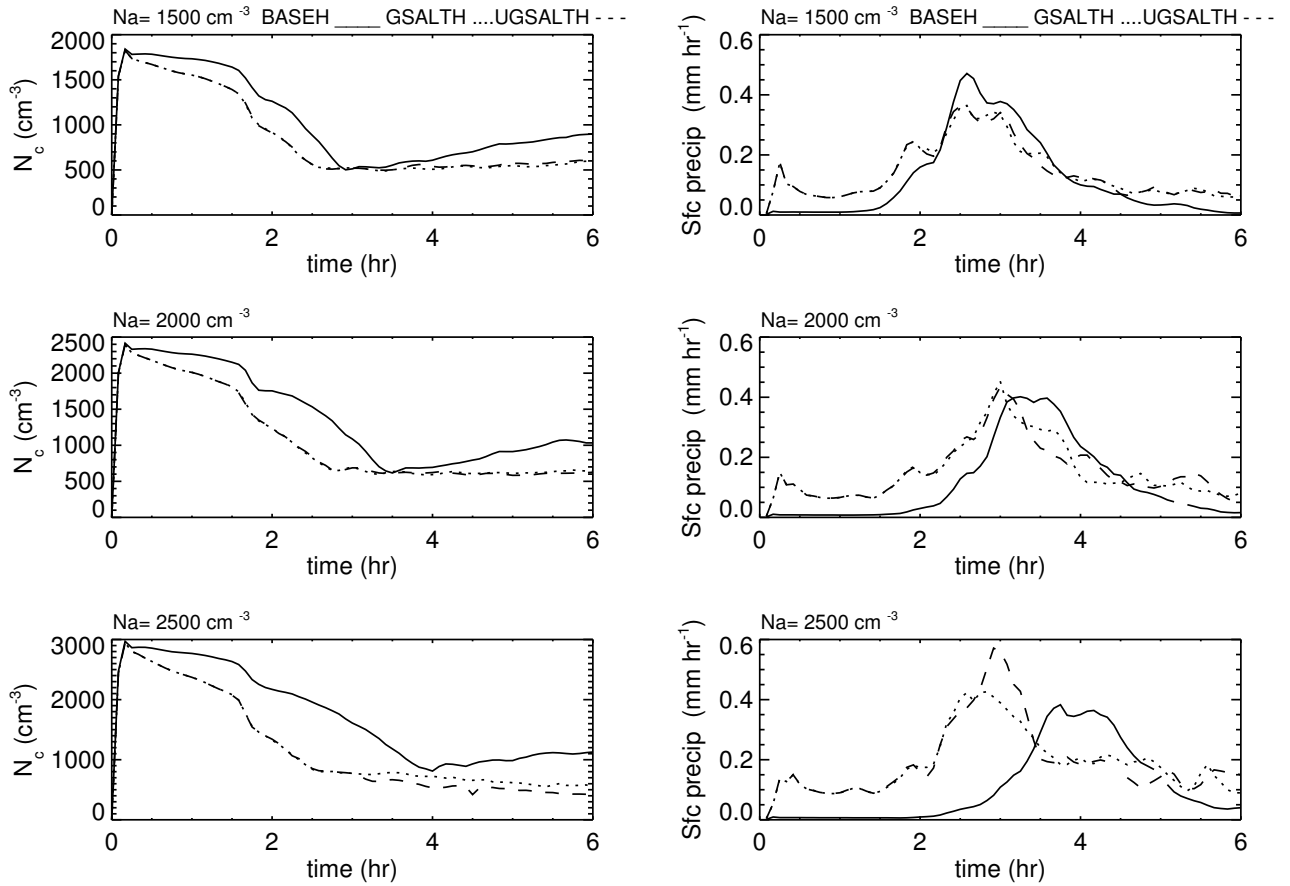


Figure 4.14: Temporal evolution of domain averaged cloud droplet number concentration (left) and surface precipitation rate (right) at high aerosol loadings ( $N_a = 1500, 2000, 2500 \text{ cm}^{-3}$ ) for BASEH, GSALTH, and UGSALTH.

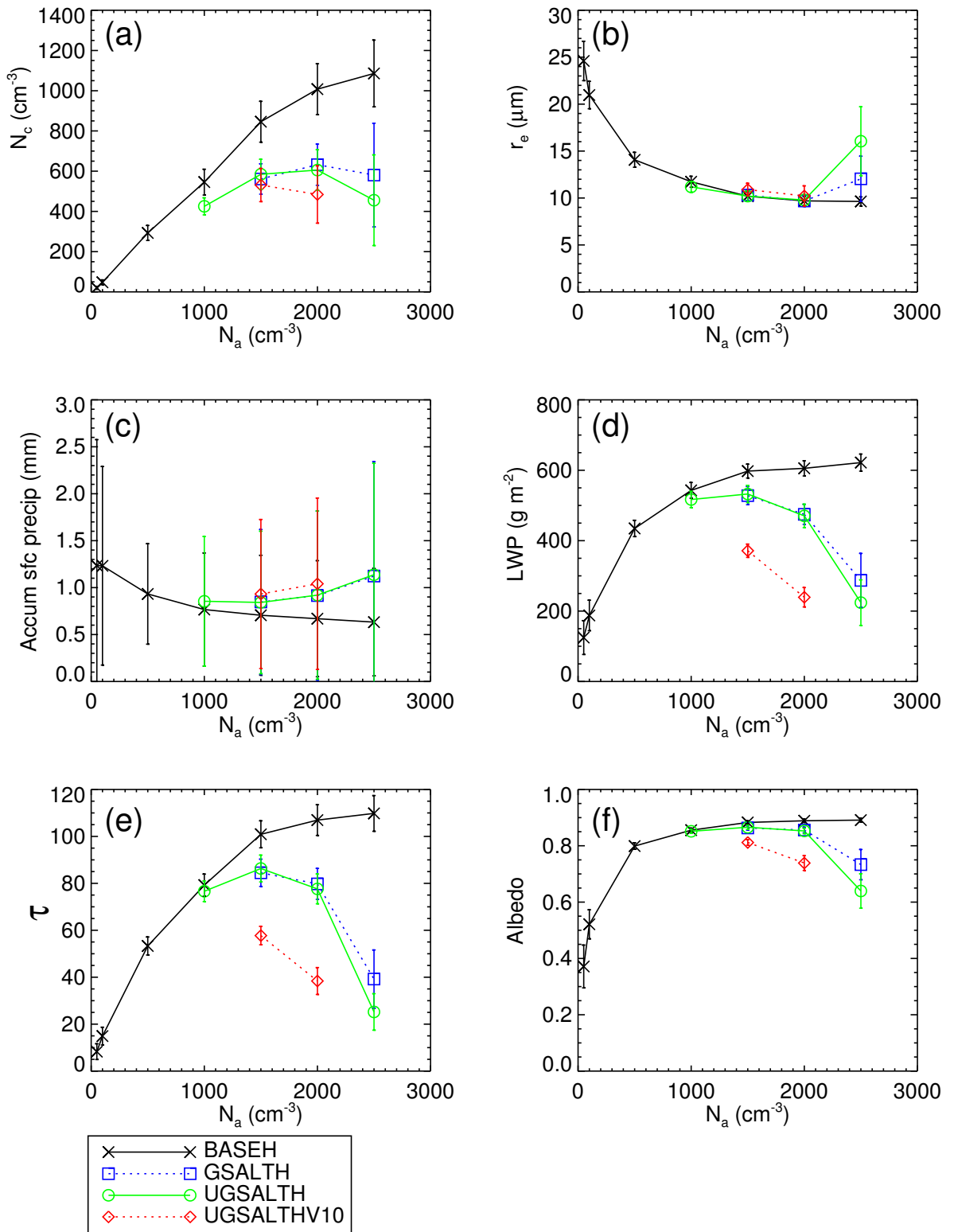


Figure 4.15: Simulation results of the ASTEX sounding (Fig. 4.12) on different sulfate aerosol concentrations as seen on (a)  $N_c$ , (b)  $r_e$ , (c) accumulated surface precipitation, (d) cloud LWP, (e)  $\tau$ , and (f) cloud albedo. Data are domain-averaged during the final 1 hour of the simulation. The accumulated surface precipitation is summed over the 6 h simulations.

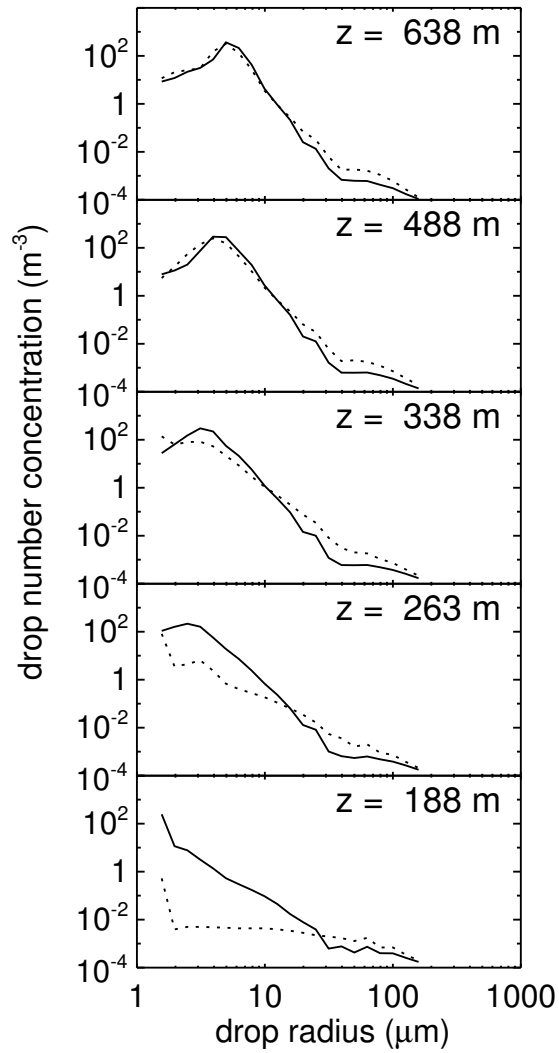


Figure 4.16: Layer-averaged drop spectra for  $N_a = 2000 \text{ cm}^{-3}$  at selected heights at  $t = 5 \text{ h}$ . Solid line is BASEH run and dotted line is UGSALTH.

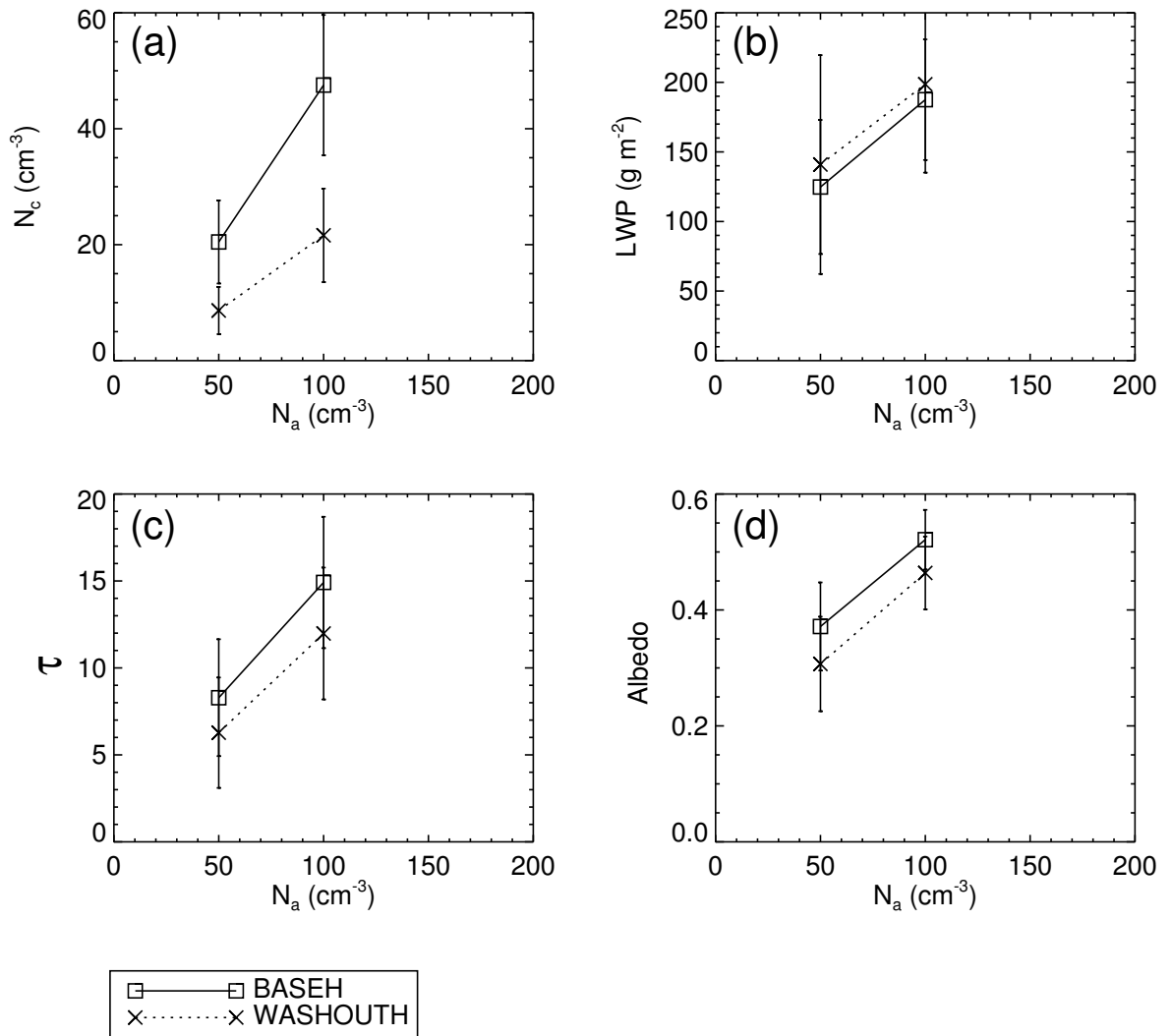


Figure 4.17: Similar to Fig. 4.15 except for the inclusion of aerosol washout by drizzle drops (WASHOUTH).

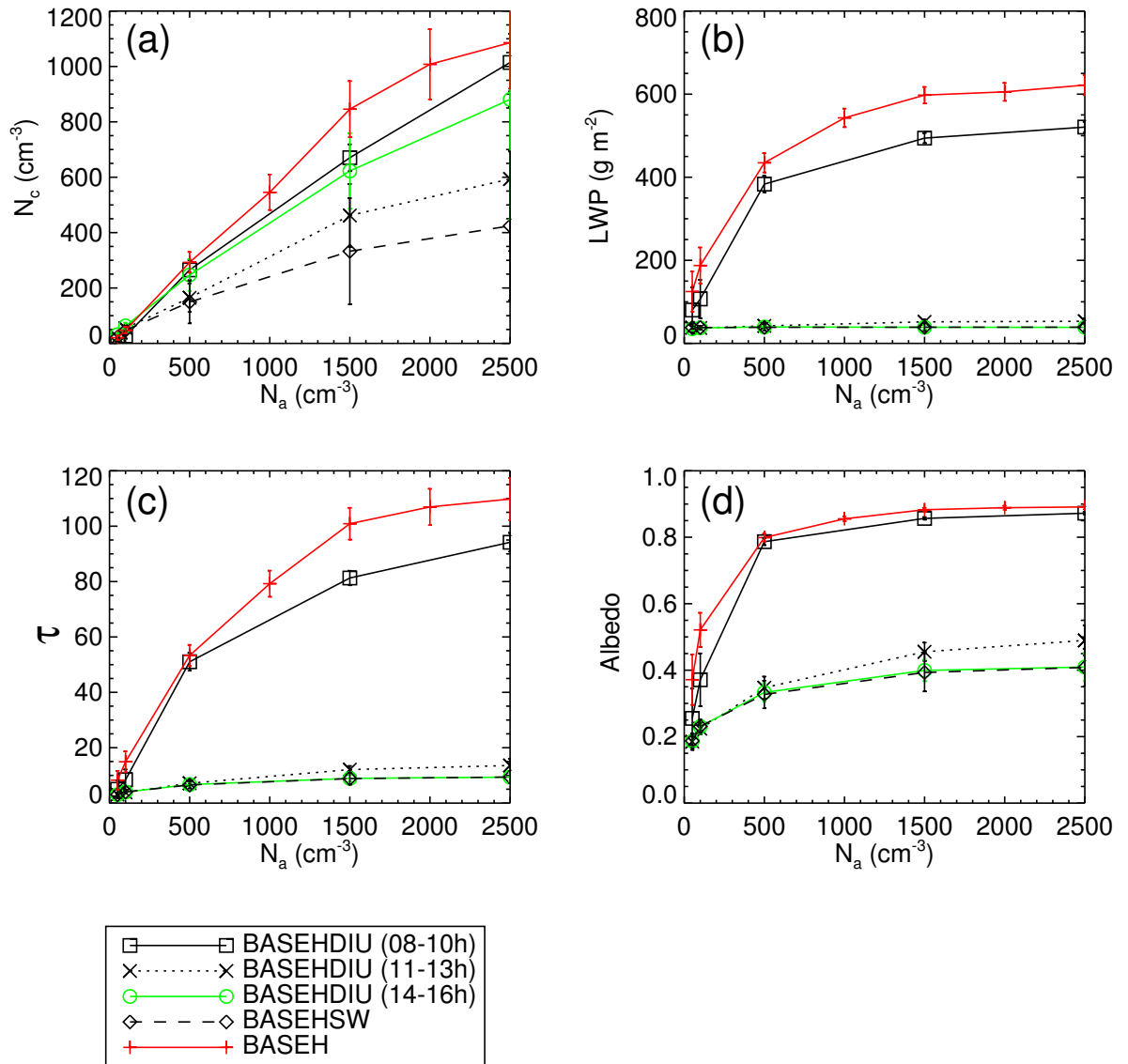


Figure 4.18: Simulation results of the ASTEX sounding (Fig. 4.12) on different sulfate aerosol concentrations as seen on (a)  $N_c$ , (b) LWP, (c)  $\tau$ , and (d) cloud albedo for the BASEHDIU early morning (local standard time 08-10h), noon (11-13h), and afternoon (14-16h).

## Chapter 5

# Future studies

The goal of this thesis is to understand the underlying interplay of the interactions between aerosol-cloud-radiation and leading ultimately to improve the confidence of the aerosol indirect forcing evaluation. Following this spirit, therefore, several further studies with the frame of the cloud model utilized in this thesis are proposed:

### 1) LES scale modeling

#### *Semi-indirect effect*

Chapter 4 presents the studies the aerosol indirect effect of non-scattering sulfate aerosols of the LES stratocumulus with the Khler theory-based aerosol activation scheme. The similar methodology can be extended to the study of the aerosol semi-indirect effect, in which that the absorbing aerosols such as black carbon can result in surface warming via cloud evaporation due to solar heating, and further a reduction of cloud cover (Hansen et al. 1997, 2000; Ackerman et al. 2000; Koren et al. 2004). The goal can be achieved by imposing the increased atmospheric SW heating due to absorbing aerosols into the cloud.

#### *Land cloud*

This thesis focuses on the aerosol indirect effect of the marine stratocumulus clouds.

The other aspect to improve the understanding of the aerosol indirect effect is to conduct the simulations of the continental clouds over the anthropogenic aerosol sources, such as South East Asia, Africa, and South America.

## 2) Lagrangian CRM/meso-scale modeling

### *Vast region from solid stratocumulus to trade wind cumuli*

The second indirect effect is found to have a different effect on the overall aerosol indirect effect with different precipitation intensity or sounding profiles used in the model. Therefore, the study of Chapter 4 suggests that the sign of the second indirect effect depends on the meteorological conditions. The current study of the aerosol indirect effect is a LES domain with the fixed meteorological condition. A further study from this is to simulate the larger domain comprising the vast region of both the solid and broken stratocumulus and the trade wind cumuli, with a realistically varying background sounding conditions. Due to the significant computer time for simulating LES clouds with explicit bin microphysics, the practical way is to run the model with the coarser grid spacing than LES, say the CRM (cloud resolving model) or a 2D eddy resolving model similar to the methods in Krueger et al. (1995) and Wyant et al. (1997). Therefore we can use a Lagrangian way of varying the meteorological conditions representative of climatological conditions (e.g., increase the SST by 1.5 K per day) in the subtropical northeastern Pacific, representing a gradual change from solid stratocumulus deck to trade wind cumuli. In this way the myriad interactions between aerosol-cloud-radiation in different boundary cloud regimes and the diurnal variation can be explored with the timescale of several days instead of a fixed background condition and a few hours in this study.

### 3) CRM-GCM scale modeling

#### *Embedding cloud resolving model in GCM*

The global instantaneous aerosol indirect radiative forcing and the long-term climatic response of this aerosol indirect perturbation can not be resolved without the use of the GCM. The typical GCM grid size (200–500 km) is much larger than the cloud scale (typically in the range of several hundred meters to several tenth kilometers), thereby, the cloud is usually coarsely parameterized in the GCM. However, it is found by numerous studies and this study that the aerosol indirect effect is sensitive to the meteorological conditions and the cloud scale process, such as precipitation intensity, cloudiness, and cloud LWP variability. Therefore, one cannot isolate the interactions between aerosol and cloud dynamics, for example, changing the aerosol number concentration can alter the precipitation process and also cloud depth and LWP. In this regard, simply adding the aerosol activation parameterization scheme into the GCM is not enough. A cloud model comprising the subgrid cloud variability and the aerosol-cloud interaction is also needed to confidently assess the aerosol indirect forcing and the climatic effect. The strategy is therefore adopting the approach by Grabowski (2001) of coupling the 2D cloud resolving model (CRM) in each column of a 3D large-scale model. Also, the multi-composition aerosol activation parameterization of Abdul-Razzak and Ghan (2000) or Nenes and Seinfeld (2003) is used in the CRM. The method proposed by Grabowski uses the concept of the classical moist convection parameterization, in which the cloud model and the GCM communicate with each other through the large-scale dynamics (or forcing terms). This approach was applied to the NCAR Community Climate System Model shown in Khairoutdinov and Randall (2001) and Randall et al. (2003). However, due to the overwhelming computing time expected, for example, Khairoutdinov and Randall (2001) showed that their GCM was slowed down by the CRM

by a factor of 180. The practical first step should start with embedding the CRM into the single-column model (the column-physics component of the GCM).

---

# Bibliography

Abdul-Razzak, H., S. Ghan, and C. Rivera-Carpio, 1998: A parameterization of aerosol activation. 1. single aerosol type. *J. Geophys. Res.*, **103**, 6123–6131.

Abdul-Razzak, H. and S. J. Ghan, 2000: A parameterization of aerosol activation. 2. multiple aerosol types. *J. Geophys. Res.*, **105**, 6837–6844.

Ackerman, A. S., M. P. Kirkpatrick, D. E. Stevens, and O. B. Toon, 2004: The impact of humidity above stratiform clouds on indirect aerosol climate forcing. *Nature*, **432**, 1014–1017.

Ackerman, A. S., O. B. Toon, D. E. Stevens, and J. A. Coakley, 2003: Enhancement of cloud cover and suppression of nocturnal drizzle in stratocumulus polluted by haze. *Geophys. Res. Lett.*, **30**, 1381, doi:10.1029/2002GL016634.

Ackerman, A. S., O. B. Toon, D. E. Stevens, A. J. Heymsfield, V. Ramanathan, and E. J. Welton, 2000: Reduction of tropical cloudiness by soot. *Science*, **288**, 1042–1047.

Ackerman, B., 1958: Turbulence around tropical cumuli. *J. Meteor.*, **15**, 69–74.

Albrecht, B. A., 1989: Aerosols, cloud microphysics, and fractional cloudiness. *Science*, **245**, 1227–1230.

Albrecht, B. A., C. S. Bretherton, D. Johnson, W. H. Scubert, and A. S. Frisch, 1995: The

- atlantic stratocumulus transition experiment - ASTEX. *Bull. Amer. Meteor. Soc.*, **76**, 889–904.
- Andreae, M., D. Rosenfeld, P. Artaxo, A. Costa, G. Frank, K. Longo, and M. Silva-Dias, 2004: Smoking rain clouds over the Amazon. *Science*, **303**, 1337–1342.
- Arking, A., 1996: Absorption of solar energy in the atmosphere: Discrepancy between model and observations. *Science*, **273**, 779–782.
- , 1999: The influence of clouds and water vapor on atmospheric absorption. *Geophys. Res. Lett.*, **26**, 2729–2732.
- Austin, G. R., R. M. Rauber, H. T. Ochs III, and L. J. Miller, 1996: Trade-wind clouds and Hawaiian rainbands. *Mon. Wea. Rev.*, **124**, 2126–2151.
- Betts, A. and R. Boers, 1990: A cloudiness transition in a marine boundary-layer. *J. Atmos. Sci.*, **47**, 1480–1497.
- Bohren, C. F., 1980: Multiple scattering of light and some of its observable consequences. *Amer. J. Phys.*, **55**, 524–533.
- Brenguier, J.-L., H. Pawlowska, and L. Schüller, 2003: Cloud microphysical and radiative properties for parameterization and satellite monitoring of the indirect effect of aerosols on climate. *J. Geophys. Res.*, **108**, 8632, doi:10.1029/2002JD002682.
- Brenguier, J.-L., H. Pawlowska, L. Schüller, R. Preusker, and J. Fischer, 2000: Radiative properties of boundary layer clouds: Droplet effective radius versus number concentration. *J. Atmos. Sci.*, **57**, 807–821.
- Bréon, F.-M., D. Tanré, and S. Generoso, 2002: Aerosol effect on cloud droplet size monitored from satellite. *Science*, **295**.

- Bretherton, C. S. and P. K. Smolarkiewicz, 1989: Gravity waves, compensating subsidence and detrainment around cumulus clouds. *J. Atmos. Sci.*, **46**, 740–759.
- Chen, C. and W. R. Cotton, 1983: A one-dimensional simulation of the stratocumulus-capped mixed layer. *Bound.-Layer Meteor.*, **25**, 289–321.
- Chen, Y.-L. and A. J. Nash, 1994: Diurnal variation of surface airflow and rainfall frequencies on the island of Hawaii. *Mon. Wea. Rev.*, **122**, 34–56.
- Chlond, A. and A. Wolkau, 2000: Large-eddy simulation of a nocturnal stratocumulus-topped marine atmospheric boundary layer: An uncertainty analysis. *Bound.-Layer Meteor.*, **95**, 31–55.
- Chylek, P. and V. Ramaswamy, 1982: Simple approximation for infrared emissivity of water clouds. *J. Atmos. Sci.*, **39**, 171–177.
- Ciesielski, P. E., W. H. Schubert, and R. H. Johnson, 1999: Large-scale heat and moisture budgets over the ASTEX region. *J. Atmos. Sci.*, **56**, 3241–3261.
- , 2001: Diurnal variability of the marine boundary layer during astex. *J. Atmos. Sci.*, **58**, 2355–2376.
- Clarke, A. D. and V. N. Kapustin, 2002: A Pacific aerosol survey. Part I: A decade of data on particle production, transport, evolution, and mixing in the troposphere. *J. Atmos. Sci.*, **59**, 363–382.
- Coakley, J. A., J. R. Bernstein, and P. A. Durkee, 1987: Effect of ship track effluents on cloud reflectivity. *Science*, **237**, 1020–1021.
- Collins, D. R., R. C. Flagan, and J. H. Seinfeld, 2002: Improved inversion of scanning DMA data. *Aerosol. Sci. Technol.*, **36**, 1–9.

- Conant, W. C., A. M. Vogelmann, and V. Ramanathan, 1998: The unexplained solar absorption and atmospheric H<sub>2</sub>O: a direct test using clear-sky data. *Tellus*, **50**, 525–533.
- Cooper, W. A., R. T. Bruintjes, and G. K. Mather, 1997: Calculations pertaining to hygroscopic seeding with flares. *J. Appl. Meteor.*, **36**, 1449–1469.
- Crisp, D., 1997: Absorption of sunlight by water vapor in cloudy conditions: A partial explanation for the cloud absorption anomaly. *Geophys. Res. Lett.*, **24**, 571–574.
- d’Almeida, G. A., P. Koepke, and E. P. Shettle, 1991: Atmospheric aerosols—global climatology and radiative characteristics. A. Deepak Publishing, Hampton, Virginia.
- Dana, M. T. and J. M. Hales, 1976: Statistical aspects of the washout of polydisperse aerosols. *Atmos. Env.*, **10**, 45–50.
- Davidson, B., 1968: The Barbados oceanographic and meteorological experiment. *Bull. Amer. Meteor. Soc.*, **49**, 928–934.
- Davies, R., W. L. Ridgway, and K.-E. Kim, 1984: Spectral absorption of solar radiation in cloudy atmosphere: A 20 cm<sup>-1</sup> model. *J. Atmos. Sci.*, **41**, 2126–2137.
- Deardorff, J. W., 1970: A numerical study of three-dimensional turbulent channel flow at large Reynolds number. *J. Fluid Mech.*, **41**, 453–480.
- Duynkerke, P. G., P. J. Jonker, A. Chlond, M. C. Van Zanten, J. Cuxart, P. Clark, E. Sanchez, G. Martin, G. Lenderink, and J. Teixeira, 1999: Intercomparison of three- and one-dimensional model simulations and aircraft observations of stratocumulus. *Bound.-Layer Meteor.*, **92**, 453–487.
- Evans, K. F., 1993: Two-dimensional radiative transfer in cloudy atmospheres: The spherical harmonic spatial grid method. *J. Atmos. Sci.*, **50**, 3111–3124.

- , 1998: The spherical harmonic discrete ordinate method for three-dimensional atmospheric radiative transfer. *J. Atmos. Sci.*, **55**, 429–446.
- Feingold, G., B. S. A. S. Frisch, and W. R. Cotton, 1999a: On the relationship among cloud turbulence, droplet formation and drizzle as viewed by doppler radar, microwave radiometer and lidar. *J. Geophys. Res.*, **104**, 22195–22203.
- Feingold, G., R. Boers, B. Stevens, and W. Cotton, 1997: A modeling study of the effect of drizzle on cloud optical depth and susceptibility. *J. Geophys. Res.*, **102**, 13527–13534.
- Feingold, G., W. R. Cotton, S. M. Kreidenweis, and J. T. Davis, 1999b: The impact of giant cloud condensation nuclei on drizzle formation in stratocumulus: Implications for cloud radiative properties. *J. Atmos. Sci.*, **56**, 4100–4117.
- Feingold, G., W. L. Eberhard, D. E. Veron, and M. Previdi, 2003: First measurements of the twomey indirect effect using ground-based remote sensors. *Geophys. Res. Lett.*, **30**.
- Feingold, G. and S. Kreidenweis, 2002: Cloud processing of aerosol as modeled by a large eddy simulation with coupled microphysics and aqueous chemistry. *J. Geophys. Res.*, **107**, 4687, doi:10.1029/2002JD002054.
- Feingold, G., S. Kreidenweis, B. Stevens, and W. Cotton, 1996: Numerical simulations of stratocumulus processing of cloud condensation nuclei through collision-coalescence. *J. Geophys. Res.*, **101**, 21391–21402.
- Feingold, G., B. Stevens, W. Cotton, and R. Walko, 1994: An explicit cloud microphysics/LES model designed to simulate the Twomey effect. *Atmos. Res.*, **33**, 207–233.
- Ferek, R. J., T. Garrett, P. V. Hobbs, S. Strader, D. Johnson, J. P. Taylor, K. Nielsen, A. S.

- Ackerman, Y. Kogan, Q. F. Liu, B. A. Albrecht, and D. Babb, 2000: Drizzle suppression in ship tracks. *J. Atmos. Sci.*, **57**, 2707–2728.
- Fitzjarrald, D. and M. Garstang, 1981: Vertical structure of the tropical boundary-layer. *Mon. Wea. Rev.*, **109**, 1512–1526.
- Fu, Q. and K. N. Liou, 1992: On the correlated  $k$ -distribution method for radiative transfer in nonhomogeneous atmospheres. *J. Atmos. Sci.*, **49**, 2139–2156.
- GEWEX, 2000: GEWEX Global cloud system study (GCSS). Second science and implementation Plan. IPGO publication series. **34**, 52pp.
- Ghan, S. J., G. Guzman, and H. Abdul-Razzak, 1998: Competition between sea salt and sulfate particles as cloud condensation nuclei. *J. Atmos. Sci.*, **55**, 3340–3347.
- Ghan, S. J., L. R. Leung, R. C. Easter, and H. Abdul-Razzak, 1997: Prediction of cloud droplet number in a general circulation model. *J. Geophys. Res.*, **102**, 21777–21794.
- Grabowski, W. W., 2001: Coupling cloud processes with the large-scale dynamics using the cloud-resolving convection parameterization (CRCP). *J. Atmos. Sci.*, **58**, 978–997.
- Han, Q., W. B. Rossow, J. Chou, and R. M. Welch, 1998: Global variation of column droplet concentration in low-level clouds. *Geophys. Res. Lett.*, **25**, 1419–1422.
- Hansen, J., M. Sato, and R. Ruedy, 1997: Radiative forcing and climate response. *J. Geophys. Res.*, **102**, 6831–6864.
- Hansen, J., M. Sato, R. Ruedy, A. Lacis, and V. Oinas, 2000: Global warming in the twenty-first century: An alternative scenario. *Proc. Natl. Acad. Sci. USA*, **97**, 9875–9880.

- Hansen, J. E. and L. D. Travis, 1974: Light scattering in planetary atmospheres. *Space Sci. Rev.*, **16**, 527–610.
- Harrington, J. Y., 1997: The effects of radiative and microphysical processes on simulated warm and transition season arctic stratus. *CSU Dept. of Atmospheric Science paper*, **637**.
- Heymsfield, A. and G. McFarquhar, 2001: Microphysics of INDOEX clean and polluted trade cumulus clouds. *J. Geophys. Res.*, **106**, 28,653–28,673.
- Hobbs, P. V. and L. F. Radke, 1992: Reply. *J. Atmos. Sci.*, **49**, 1516–1517.
- Hoppel, W. A., G. M. Frick, and J. W. Fitzgerald, 1996: Deducing droplet concentration and supersaturation in marine boundary layer clouds from surface aerosol measurements. *J. Geophys. Res.*, **101**, 26,553–26,565.
- Houghton, J. T., T. Ding, D. J. Griggs, M. Noguer, P. J. van der Linden, X. Dai, K. Maskell, and C. A. Johnson, 2001: Climate change 2001: The scientific basis. Contribution of working group 1 to the third assessment report of the intergovernmental panel on climate change. Cambridge University Press, Cambridge, United Kingdom.
- Jenkins, F. and H. White, 1957: *Fundamentals of Optics*. McGraw Hill, New York.
- Jiang, H. and W. R. Cotton, 2000: Large eddy simulation of shallow cumulus convection during BOMEX: Sensitivity to microphysics and radiation. *J. Atmos. Sci.*, **57**, 582–594.
- Jiang, H., G. Feingold, and W. Cotton, 2002: Simulations of aerosol-cloud-dynamical feedbacks resulting from entrainment of aerosol into the marine boundary layer during the Atlantic Stratocumulus Transition Experiment. *J. Geophys. Res.*, **107**, 4813, doi:10.1029/2001JD001502.

- Jiang, H., G. Feingold, W. Cotton, and P. Duynkerke, 2001: Large-eddy simulations of entrainment of cloud condensation nuclei into the Arctic boundary layer: May 18, 1998, FIRE/SHEBA case study. *J. Geophys. Res.*, **106**, 15113–15122.
- Johnson, D. B., 1982: The role of giant and ultragiant aerosol particles in warm rain initiation. *J. Atmos. Sci.*, **39**, 448–460.
- Kaufman, V. and B. Edlen, 1974: Reference wavelengths from atomic spectra in the range 15 Å to 25000 Å. *J. Phys. Chem. Ref. Data*, **3**, 825–896.
- Kebabian, P. L., 1998: Optical Monitor for Water Vapor Concentration. U.S. Patent #5760,895. New York.
- Kebabian, P. L., T. Berkoff, and A. Freedman, 1998: Water vapour sensing using polarization selection of a Zeeman-split argon discharge lamp emission line. *Meas. Sci. Technol.*, **9**, 1793–1796.
- Kebabian, P. L., C. E. Kolb, and A. Freedman, 2002: Spectroscopic water vapor sensor for rapid response measurements of humidity in the troposphere. *J. Geophys. Res.*
- Kerminen, V.-M. and A. S. Wexler, 1994: Particle formation due to SO<sub>2</sub> oxidation and high relative humidity in the remote marine boundary layer. *J. Geophys. Res.*, **99**, 25,607–25,614.
- Khairoutdinov, M. F. and D. A. Randall, 2001: A cloud resolving model as a cloud parameterization in the near community climate system model: Preliminary results. *Geophys. Res. Lett.*, **28**, 3617–3620.
- Kim, B., S. Schwartz, M. Miller, and Q. Min, 2003: Effective radius of cloud droplets

- by ground-based remote sensing: Relationship to aerosol. *J. Geophys. Res.*, **108**, 4740, doi:10.1029/2003JD003721.
- Kogan, Y. L., 1991: The simulation of a convective cloud in a 3-D model with explicit microphysics. Part I: Model description and sensitivity experiments. *J. Atmos. Sci.*, **48**, 1160–1189.
- Kollias, P., B. A. Albrecht, R. Lhermitte, and A. Savtchenko, 2001: Radar observations of updrafts, downdrafts, and turbulence in fair-weather cumuli. *J. Atmos. Sci.*, **58**, 1750–1766.
- Koren, I., Y. Kaufman, L. Remer, and J. Martins, 2004: Measurement of the effect of amazon smoke on inhibition of cloud formation. *Science*, **303**, 1342–1345.
- Krueger, S., 1988: Numerical simulation of tropical cumulus clouds and their interaction with the subcloud layer. *J. Atmos. Sci.*, **45**, 2221–2250.
- Krueger, S., G. Mclean, and Q. Fu, 1995: Numerical-simulation of the stratus-to-cumulus transition in the subtropical marine boundary-layer. 1. boundary-layer structure. *J. Atmos. Sci.*, **52**, 2839–2850.
- Lawson, R. P. and W. A. Cooper, 1990: Performance of some airborne thermometers in clouds. *J. Atmos. Ocea. Tech.*, **7**, 480–494.
- Li, J. and Y.-L. Chen, 1999: A case study of nocturnal rain showers over the windward coastal region of the island of Hawaii. *Mon. Wea. Rev.*, **127**, 2674–269.
- Li, Z. and A. P. Trishchenko, 2001: Quantifying uncertainties in determining SW cloud radiative forcing and cloud absorption due to variability in atmospheric conditions. *J. Atmos. Sci.*, **58**, 376–389.

- Liu, Y. G. and P. H. Daum, 2000: The effect of refractive index on size distributions and light scattering coefficients derived from optical particle counters. *J. Aerosol Sci.*, **31**, 945–957.
- Lu, M.-L., R. A. McClatchey, and J. H. Seinfeld, 2002: Cloud halos: numerical simulation of dynamical structure and radiative impact. *J. Appl. Meteor.*, **41**, 832–848.
- Malkus, J. S., 1949: Effects of wind shear on some aspects of convection. *Trans. Amer. Geophys. Union*, **30**, 19–25.
- , 1954: Some results of a trade-cumulus investigation. *J. Meteor.*, **11**, 220–237.
- Marshak, A., A. Davis, W. Wiscombe, W. Ridgway, and R. Cahalan, 1998: Biases in shortwave column absorption in the presence of fractal clouds. *J. Climate*, **11**, 431–446.
- McClatchey, R. A., R. W. Fenn, J. E. A. Selby, P. E. Volz, and J. S. Garing, 1972: Optical properties of the atmosphere (3rd edition). AFCRL-72-0497, Air Force Cambridge University Press, Defense Technical Information Center, AD 753-075.
- McManus, J. B., P. L. Keabian, and M. Zahniser, 1995: Astigmatic mirror multipass absorption cell for long path length spectroscopy. *Appl. Opt.*, **34**, 3336–3338.
- McNider, R. T. and F. J. Kopp, 1990: Specification of the scale and magnitude of thermals used to initiate convection in cloud models. *J. Appl. Meteor.*, **29**, 99–104.
- Menon, S., J. Brenguier, O. Boucher, P. Davison, A. Del Genio, J. Feichter, S. Ghan, S. Guibert, X. Liu, U. Lohmann, H. Pawlowska, J. Penner, J. Quaas, D. Roberts, L. Schuller, and J. Snider, 2003: Evaluating aerosol/cloud/radiation process parameterizations with single-column models and Second Aerosol Characterization

- Experiment (ACE-2) cloudy column observations. *J. Geophys. Res.*, **108**, 4762, doi:10.1029/2003JD003902.
- Moeng, C., P. P. Sullivan, and B. Stevens, 1999: Including radiative effects in an entrainment rate formula for buoyancy-driven PBLs. *J. Atmos. Sci.*, **56**, 1031–1049.
- Moeng, C.-H., W. R. Cotton, C. Bretherton, A. Chiond, M. Khairoutdinov, S. Krueger, W. S. Lwellen, M. K. Macvean, J. R. M. Pasquier, H. A. Rand, A. P. Siebesma, B. Stevens, and R. I. Sykes, 1996: Simulation of a stratocumulus-topped planetary boundary layer: Intercomparison among different numerical codes. *Bull. Amer. Meteor. Soc.*, **77**, 261–278.
- Moore, C., 1971: Atomic Energy Levels. NBS Circular 467. U.S. Government Printing Office, Washington, D.C.
- Mordy, W., 1959: Computations of the growth by condensation of a population of cloud droplets. *Tellus*, **11**, 16–44.
- Murray, F. W., 1971: Humidity augmentation as the initial pulse in a numerical cloud model. *Mon. Wea. Rev.*, **99**, 37–48.
- Nakajima, T. and M. Tanaka, 1988: Algorithms for radiative intensity calculations in moderately thick atmospheres using a truncation approximation. *J. Quant. Spectrosc. Radiat. Transfer*, **40**, 51–69.
- Nenes, A., R. Charlson, M. Facchini, M. Kulmala, A. Laaksonen, and J. Seinfeld, 2002: Can chemical effects on cloud droplet number rival the first indirect effect? *Geophys. Res. Lett.*, **29**, 1848, doi:10.1029/2002GL015295.
- Nenes, A. and J. Seinfeld, 2003: Parameterization of cloud droplet formation in global climate models. *J. Geophys. Res.*, **108**, 4415, doi:10.1029/2002JD002911.

- O'Dowd, C. D., J. A. Lowe, M. H. Smith, and A. D. Kaye, 1999: The relative importance of non-sea-salt sulphate and sea-salt aerosol to the marine cloud condensation nuclei population: An improved multi-component aerosol-cloud droplet parameterization. *Quart. J. Roy. Meteor. Soc.*, **125**, 1295–1313.
- O'Dowd, C. D., M. H. Smith, I. E. Consterdine, and J. A. Lowe, 1997: Marine aerosol, sea-salt, and the marine sulphur cycle: A short review. *Atmos. Env.*, **31**, 73–80.
- O'Hirok, W. and C. Gautier, 1998: A three-dimensional radiative transfer model to investigate the solar radiation within a cloudy atmosphere. Part I: spatial effects. *J. Atmos. Sci.*, **55**, 2162–2179.
- Penner, J., X. Dong, and Y. Chen, 2004: Observational evidence of a change in radiative forcing due to the indirect aerosol effect. *Nature*, **427**, 231–234.
- Perry, K. D. and P. V. Hobbs, 1994: Further evidence for particle nucleation in clear air adjacent to marine cumulus clouds. *J. Geophys. Res.*, **99**, 22,803–22,818.
- , 1996: Influences of isolated cumulus clouds on the humidity of their surroundings. *J. Atmos. Sci.*, **53**, 159–174.
- Pielke, R. A., W. R. Cotton, R. L. Walko, C. J. Tremback, W. A. Lyons, L. D. Grasso, M. E. Nicholls, M. D. Moran, D. A. Wesley, T. J. Lee, and J. H. Copeland, 1992: A comprehensive meteorological modeling system – RAMS. *Meteor. Atmos. Phys.*, **49**, 69–91.
- Pincus, R. and M. B. Baker, 1994: Effect of precipitation on the albedo susceptibility of marine boundary layer clouds. *Nature*, **372**, 250–252.

- Platt, C. M. R. and D. J. Gambling, 1971: Laser radar reflections and downward infrared flux enhancement near small cumulus. *Nature*, **232**, 182–185.
- Podgorny, I. A., A. M. Vogelmann, and V. Ramanathan, 1998: Effects of cloud shape and water vapor distribution on solar absorption in the near infrared. *Geophys. Res. Lett.*, **25**, 1899–1902.
- Pruppacher, H. R. and J. D. Klett, 1997: Microphysics of clouds and precipitation, 954 pp. ,Kluwer Acad., Norwell, Mass.
- Radke, L. F. and P. V. Hobbs, 1991: Humidity and particle fields around some small cumulus clouds. *J. Atmos. Sci.*, **48**, 1190–1193.
- Raes, F., R. Van Dingenen, E. Vignati, J. Wilson, J. P. Putaud, J. H. Seinfeld, and P. Adams, 2000: Formation and cycling of aerosols in the global troposphere. *Atmos. Environ.*, **34**, 4215–4240.
- Raga, G. B., J. B. Jensen, and M. B. Baker, 1990: Characteristics of cumulus band clouds off the coast of Hawaii. *J. Atmos. Sci.*, **47**, 338–355.
- Randall, D. A., J. A. Coakley Jr., C. W. Fairall, R. A. Kropfli, and D. H. Lenschow, 1984: Outlook for research on subtropical marine stratiform clouds. *Bull. Amer. Meteor. Soc.*, **65**, 1290–1301.
- Randall, D. A., M. Khairoutdinov, A. Arakawa, and W. Grabowski, 2003: Breaking the cloud parameterization deadlock. *Bull. Amer. Meteor. Soc.*, **84**, 1547–1564.
- Raymond, D. J. and A. M. Blyth, 1986: A stochastic mixing model for nonprecipitating cumulus clouds. *J. Atmos. Sci.*, **43**, 2708–2718.

- Raymond, D. J., R. Solomon, and A. M. Blyth, 1991: Mass fluxes in New-Mexico mountain thunderstorm from radar and aircraft measurements. *Quart. J. Roy. Meteor. Soc.*, **117**, 587–621.
- Rosenfeld, D., 1999: TRMM observed first direct evidence of smoke from forest fires inhibiting rainfall. *Geophys. Res. Lett.*, **26**, 3105–3108.
- , 2000: Suppression of rain and snow by urban and industrial air pollution. *Science*, **287**, 1793–1796.
- Rosenfeld, D., R. Lahav, A. Khain, and M. Pinsky, 2002: The role of sea spray in cleansing air pollution over ocean via cloud processes. *Science*, **297**, 1667–1670.
- Rosenfeld, D., Y. Rudich, and R. Lahav, 2001: Desert dust suppressing precipitation: A possible desertification feedback loop. *Proc. Natl. Acad. Sci. USA*, **98**, 5975–5980.
- Rothman, L. S., C. P. Rinsland, A. Goldman, S. T. Massie, D. P. Edwards, J. M. Flaud, A. Perrin, C. Camy-Peyret, V. Dana, J. Y. Mandin, J. Schroeder, A. McCann, R. R. Gamache, R. B. Wattson, K. Yoshino, K. V. Chance, K. W. Jucks, L. R. Brown, V. Nemtchinov, and P. Varanasi, 1998: The HITRAN molecular spectroscopic database and HAWKS (HITRAN atmospheric workstation): 1996 edition. *J. Quant. Spectrosc. Rad. Transfer*, **60**, 665–710.
- Schubert, W. H., J. S. Wakefield, E. J. Steiner, and S. K. Cox, 1979a: Marine stratocumulus convection. Part I: Governing equations and horizontally homogeneous solutions. *J. Atmos. Sci.*, **36**, 1286–1307.
- , 1979b: Marine stratocumulus convection. Part II: Horizontally inhomogeneous solutions. *J. Atmos. Sci.*, **36**, 1308–1324.

- Schwartz, S. E., Harshvardhan, and C. M. Benkovitz, 2002: Influence of anthropogenic aerosol on cloud optical depth and albedo shown by satellite measurements and chemical transport modeling. *Proc. Natl. Acad. Sci. USA*, **99**, 1784–1789.
- Segal, Y., A. Khain, M. Pinsky, and D. Rosenfeld, 2004: Effects of hygroscopic seeding on raindrop formation as seen from simulations using a 2000-bin spectral cloud parcel model. *Atm. Res.*, **71**, 3–34.
- Seinfeld, J. H. and S. N. Pandis, 1998: Atmospheric chemistry and physics: From air pollution to climate change. John Wiley & Sons, Inc., New York.
- Steiner, J. T., 1973: A three-dimensional model of cumulus cloud development. *J. Atmos. Sci.*, **30**, 414–435.
- Stephens, G. L., 1978: Radiation profiles in extended water clouds. Part II: Parameterization schemes. *J. Atmos. Sci.*, **35**, 2123–2132.
- Stevens, B., A. S. Ackerman, B. A. Albrecht, A. R. Brown, A. Chlond, J. Cuxart, P. G. Duynkerke, D. C. Lewellen, M. K. Macvean, R. A. J. Neggers, E. Sánchez, A. P. Siebesma, and D. E. Stevens, 2001: Simulations of trade wind cumuli under a strong inversion. *J. Atmos. Sci.*, **58**, 1870–1891.
- Stevens, B., W. R. Cotton, G. Feingold, and C.-H. Moeng, 1998: Large-eddy simulations of strongly precipitating, shallow, stratocumulus-topped boundary layer. *J. Atmos. Sci.*, **55**, 3616–3638.
- Stevens, B., G. Feingold, W. Cotton, and R. Walko, 1996a: Elements of the microphysical structure of numerically simulated nonprecipitating stratocumulus. *J. Atmos. Sci.*, **53**, 980–1006.

- Stevens, B., R. L. Walko, and W. R. Cotton, 1996b: The spurious production of cloud-edge supersaturations by Eulerian models. *Mon. Wea. Rev.*, **124**, 1034–1041.
- Takahashi, T., 1977: A study of Hawaiian warm rain showers based on aircraft observation. *J. Atmos. Sci.*, **34**, 1733–1790.
- Taylor, G. R. and M. B. Baker, 1991: Entrainment and detrainment in cumulus clouds. *J. Atmos. Sci.*, **48**, 112–121.
- Telford, J. W. and P. B. Wagner, 1980: The dynamical and liquid water structure of the small cumulus as determined from its environment. *Pure Appl. Geophys.*, **118**, 935–952.
- Trautmann, T., I. Podgorny, J. Landgraf, and P. J. Crutzen, 1999: Actinic fluxes and photodissociation coefficients in cloud fields embedded in realistic atmospheres. *J. Geophys. Res.*, **104**, 30173–30192.
- Tripoli, G. J. and W. R. Cotton, 1981: The use of ice-liquid water potential temperature as a thermodynamic variable in deep atmospheric models. *Mon. Wea. Rev.*, **109**, 1094–1102.
- Twohy, C. H., M. D. Petters, J. R. Snider, B. Stevens, W. Tahnk, M. Wetzal, L. Russell, and F. Burnet, 2005: Evaluation of the aerosol indirect effect in marine stratocumulus clouds: droplet number, size, liquid water path and radiative impact. *J. Geophys. Res.*, , doi:10.1029/2004JD005116.
- Twomey, S., 1977: The influence of pollution on the shortwave albedo of clouds. *J. Atmos. Sci.*, **34**, 1149–1152.
- Tzivion, S., G. Feingold, and Z. Levin, 1987: An efficient numerical solution to the stochastic collection equation. *J. Atmos. Sci.*, **44**, 3139–3149.

- , 1989: The evolution of raindrop spectra. 2. Collisional collection breakup and evaporation in a rainshaft. *J. Atmos. Sci.*, **46**, 3312–3327.
- Vaillancourt, P. A., M. K. Yau, and W. W. Grabowski, 1997: Upshear and downshear evolution of cloud structure and spectral properties. *J. Atmos. Sci.*, **54**, 1203–1217.
- Vogelmann, A. M., V. Ramanathan, W. C. Conant, and W. E. Hunter, 1998: Observational constraints on non-Lorentzian continuum effects in the near-infrared solar spectrum using ARM ARESE data. *J. Quant. Spectrosc. Radiat. Transfer*, **60**, 231–246.
- Von der Emde, K. and U. Wacker, 1993: Comments on the relationship between aerosol spectra, equilibrium drop size spectra, and CCN spectra. *Beitr. Phys. Atmos.*, **66**, 157–162.
- Wakefield, J. S. and W. H. Schubert, 1981: Mixed-layer mode simulation of eastern north Pacific stratocumulus. *Mon. Wea. Rev.*, **109**, 1952–1968.
- Walko, R. L., W. R. Cotton, M. P. Meyers, and J. Y. Harrington, 1995: New RAMS cloud microphysics parameterization. Part I: The single-moment scheme. *Atmos. Res.*, **38**, 29–62.
- Wang, J.-J. and Y.-L. Chen, 1998: A case study of trade-wind rainbands and their interaction with the island-induced airflow. *Mon. Wea. Rev.*, **126**, 409–423.
- Wang, S. and R. C. Flagan, 1990: Scanning electrical mobility spectrometer. *Aerosol. Sci. Technol.*, **13**, 230–240.
- Warner, J., 1955: The water content of cumuliform cloud. *Tellus*, **7**, 449–457.
- , 1977: Time variation of updraft and water content in small cumulus clouds. *J. Atmos. Sci.*, **34**, 1306–1312.

- Warren, S. G., C. J. Hahn, J. London, R. M. Chervine, and R. L. Jenne, 1986: Global distribution of total cloud cover and cloud type amounts over ocean. NCAR/TN-317+STR, NCAR Tech. Note., New York.
- Weber, R. J., G. Chen, D. D. Davis, R. L. Mauldin III, D. J. Tanner, F. L. Eisele, A. D. Clarke, D. C. Thornton, and A. R. Bandy, 2001: Measurements of enhanced H<sub>2</sub>SO<sub>4</sub> and 2-4 nm particles near a frontal cloud during the First Aerosol Characterization Experiment (ACE1). *J. Geophys. Res.*, **106**, 24,107–24,117.
- Wendisch, M. and A. Keil, 1999: Discrepancies between measured and modeled solar and UV radiation within polluted boundary layer clouds. *J. Geophys. Res.*, **104**, 27373–27385.
- Wyant, M. C., C. S. Bretherton, H. A. Rand, and D. E. Stevens, 1997: Numerical simulations and a conceptual model of the stratocumulus to trade cumulus transition. *J. Atmos. Sci.*, **54**, 168–192.
- Yin, Y., Z. Levin, T. G. Reisin, and S. Tzivion, 2000: The effects of giant cloud condensation nuclei on the development of precipitation in convective clouds — A numerical study. *Atm. Res.*, **53**, 91–116.
- Yum, S. S. and J. G. Hudson, 2002: Maritime/continental microphysical contrasts in stratus. *Tellus*, **54B**, 61–73.
-